The Scale Invariant Generator Technique and Scaling Anisotropy in Geophysics

BY

GREGORY LEWIS

A THESIS SUBMITTED TO THE FACULTY OF
GRADUATE STUDIES AND RESEARCH IN PARTIAL
FULFILLMENT OF THE REQUIREMENT FOR THE
DEGREE OF MASTER OF SCIENCE

DEPARTMENT OF PHYSICS
McGILL UNIVERSITY
MONTREAL, QUEBEC
CANADA

AUGUST 1993

Name Gregory Lewis

Dissertation Abstracts International is arranged by broad, general subject categories. Please select the one subject which most nearly describes the content of your dissertation. Enter the corresponding four-digit code in the spaces provided.

SUBJECT TERM

SUBJECT CODE 0373

U·M·I

Subject Categories

THE HUMANITIES AND SOCIAL SCIENCES

COMMUNICATIONS AND THE ARTS

Architecture	0729
Art History	0377
Cinema	0900
Dance	0378
Fine Arts	0357
Information Science	0723
Journalism	0391
Library Science	0399
Mass Communications	0708
Music	0413
Speech Communication	0459
Theater	0465

EDUCATION

General	0515
Administration	0514
Adult and Continuing	0516
Agricultural	0517
Art	0273
Bilingual and Multicultural	0282
Business	0688
Community College	0275
Curriculum and Instruction	0727
Early Childhood	0518
Elementary	0524
Finance	0277
Guidance and Counseling	0519
Health	0680
Higher	0745
History of	0520
Home Economics	0278
Industrial	0521
Language and Literature	0279
Mathematics	0280
Music	0522
Philosophy of	0998
Physical	0523
Psychology	0525
Reading	0535
Religious	0527
Sciences	0714
Secondary	0533
Social Sciences	0534
Sociology of	0340
Special	0529
Teacher Training	0530
Technology	0710
Tests and Measurements	0288
Vocational	0747

LANGUAGE, LITERATURE AND LINGUISTICS

Language	
General	0679
Ancient	0289
Linguistics	0290
Modern	0291
Literature	
General	0401
Classical	0294
Comparative	0295
Medieval	0297
Modern	0298
African	0316
American	0591
Asian	0305
Canadian (English)	0352
Canadian (French)	0355
English	0593
Germanic	0311
Latin American	0312
Middle Eastern	0315
Romance	0313
Slavic and East European	0314

PHILOSOPHY, RELIGION AND THEOLOGY

Philosophy	0422
Religion	
General	0318
Biblical Studies	0321
Clergy	0319
History of	0320
Philosophy of	0322
Theology	0469

SOCIAL SCIENCES

American Studies	0323
Anthropology	
Archaeology	0324
Cultural	0326
Physical	0327
Business Administration	
General	0310
Accounting	0272
Banking	0770
Management	0454
Marketing	0338
Canadian Studies	0385
Economics	
General	0501
Agricultural	0503
Commerce Business	0505
Finance	0508
History	0509
Labor	0510
Theory	0511
Folklore	0358
Geography	0366
Gerontology	0351
History	
General	0578
Ancient	0579
Medieval	0581
Modern	0582
Black	0328
African	0331
Asia, Australia and Oceania	0332
Canadian	0334
European	0335
Latin American	0336
Middle Eastern	0333
United States	0337
History of Science	0585
Law	0398
Political Science	
General	0615
International Law and Relations	0616
Public Administration	0617
Recreation	0814
Social Work	0452
Sociology	
General	0626
Criminology and Penology	0627
Demography	0938
Ethnic and Racial Studies	0631
Individual and Family Studies	0628
Industrial and Labor Relations	0629
Public and Social Welfare	0630
Social Structure and Development	0700
Theory and Methods	0344
Transportation	0709
Urban and Regional Planning	0999
Women's Studies	0453

THE SCIENCES AND ENGINEERING

BIOLOGICAL SCIENCES

Agriculture	
General	0473
Agronomy	0285
Animal Culture and Nutrition	0475
Animal Pathology	0476
Food Science and Technology	0359
Forestry and Wildlife	0478
Plant Culture	0479
Plant Pathology	0480
Plant Physiology	0817
Range Management	0777
Wood Technology	0746
Biology	
General	0306
Anatomy	0287
Biostatistics	0308
Botany	0309
Cell	0379
Ecology	0329
Entomology	0353
Genetics	0369
Limnology	0793
Microbiology	0410
Molecular	0307
Neuroscience	0317
Oceanography	0416
Physiology	0433
Radiation	0821
Veterinary Science	0778
Zoology	0472
Biophysics	
General	0786
Medical	0760

EARTH SCIENCES

Biogeochemistry	0425
Geochemistry	0996
Geodesy	0370
Geology	0372
Geophysics	0373
Hydrology	0388
Mineralogy	0411
Paleobotany	0345
Paleoecology	0426
Paleontology	0418
Paleozoology	0985
Palynology	0427
Physical Geography	0368
Physical Oceanography	0415

HEALTH AND ENVIRONMENTAL SCIENCES

Environmental Sciences	0768
Health Sciences	
General	0566
Audiology	0300
Chemotherapy	0992
Dentistry	0567
Education	0350
Hospital Management	0769
Human Development	0758
Immunology	0982
Medicine and Surgery	0564
Mental Health	0347
Nursing	0569
Nutrition	0570
Obstetrics and Gynecology	0380
Occupational Health and Therapy	0354
Ophthalmology	0381
Pathology	0571
Pharmacology	0419
Pharmacy	0572
Physical Therapy	0382
Public Health	0573
Radiology	0574
Recreation	0575
Speech Pathology	0460
Toxicology	0383
Home Economics	0386

PHYSICAL SCIENCES

Pure Sciences

Chemistry	
General	0485
Agricultural	0749
Analytical	0486
Biochemistry	0487
Inorganic	0488
Nuclear	0738
Organic	0490
Pharmaceutical	0491
Physical	0494
Polymer	0495
Radiation	0754
Mathematics	0405
Physics	
General	0605
Acoustics	0986
Astronomy and Astrophysics	0606
Atmospheric Science	0608
Atomic	0748
Electronics and Electricity	0607
Elementary Particles and High Energy	0798
Fluid and Plasma	0759
Molecular	0609
Nuclear	0610
Optics	0752
Radiation	0756
Solid State	0611
Statistics	0463

Applied Sciences

Applied Mechanics	0346
Computer Science	0984
Engineering	
General	0537
Aerospace	0538
Agricultural	0539
Automotive	0540
Biomedical	0541
Chemical	0542
Civil	0543
Electronics and Electrical	0544
Heat and Thermodynamics	0348
Hydraulic	0545
Industrial	0546
Marine	0547
Materials Science	0794
Mechanical	0548
Metallurgy	0743
Mining	0551
Nuclear	0552
Packaging	0549
Petroleum	0765
Sanitary and Municipal	0554
System Science	0790
Geotechnology	0428
Operations Research	0796
Plastics Technology	0795
Textile Technology	0994

PSYCHOLOGY

General	0621
Behavioral	0384
Clinical	0622
Developmental	0620
Experimental	0623
Industrial	0624
Personality	0625
Physiological	0989
Psychobiology	0349
Psychometrics	0632
Social	0451

The Scale Invariant Generator Technique and Scaling Anisotropy

BY

GREGORY LEWIS

A THESIS SUBMITTED TO THE FACULTY OF
GRADUATE STUDIES AND RESEARCH IN PARTIAL
FULFILLMENT OF THE REQUIREMENT FOR THE
DEGREE OF MASTER OF SCIENCE

DEPARTMENT OF PHYSICS
McGILL UNIVERSITY
MONTREAL, QUEBEC
CANADA

AUGUST 1993

Abstract

Recently there has been a dramatic increase in the use of scale invariance in the study of geophysical fields. However, very little attention has been paid to the anisotropy that is invariably present in these fields, in the form of stratification, differential rotation, texture and morphology. In order to account for scaling anisotropy, the formalism of Generalized Scale Invariance (GSI) was developed. Until now, only a single analysis technique has been developed which incorporates this formalism and which can be used to study the anisotropic scaling of fields.

Using a tensorial representation of the linear approximation to GSI, a new, greatly improved technique for quantifying anisotropic scale invariance in geophysical fields is developed: the Scale Invariant Generator technique (SIG).

The ability of the technique to yield valid estimates is tested by performing the analysis on multifractal (scale invariant) simulations. It was found that SIG yields reasonable estimates for fields with a diversity of anisotropic and statistical characteristics. The analysis is also performed on three satellite cloud radiances and three sea ice SAR reflectivities to test the applicability of the technique. SIG also produced reasonable estimates in these cases.

Résumé

Récemment, la fréquence d'utilisation de l'invariance d'échelle, dans l'étude des champs géophysiques, a crû dramatiquement. Cependant, l'anisotropie, qui est toujours présente dans ces champs sous forme de stratification, rotation différentielle, texture et morphologie, a reçu très peu d'attention. Pour pouvoir tenir compte de l'anisotropie de l'invariance d'échelle, le formalisme de l'invariance d'échelle généralisée (GSI) a été développé. A présent, il n'y a qu'une seule technique d'analyse développée qui incorpore ce formalisme.

En utilisant une représentation à deux dimensions de l'approximation linéaire du GSI, une nouvelle technique, très améliorée, est développée: la technique du générateur à échelle invariante (SIG). Cette technique sert à quantifier l'invariance d'échelle anisotropique des champs géophysiques.

L'habilité, avec laquelle cette technique permet d'obtenir des estimations valides des paramètres du GSI, est évaluée en analysant des simulations multifractales (d'échelle invariante). Des estimations raisonnables, pour plusieurs champs de caractéristiques anisotropiques et statistiques différentes, ont été trouvées en utilisant SIG. Le rayonnement (capté par satellite) de trois nuages et trois réflectivités SAR, de la glace de la mer, sont également analysés afin d'évaluer l'applicabilité de cette technique. Dans ces cas aussi, SIG a produit des estimations raisonnables.

Acknowledgments

I would like to thank my supervisor, Shaun Lovejoy, for his scientific advice and assistance and also for his patience.

I would also like to thank J.F. Malouin and Charles Hooge for their help with the Silicon Graphics and Macintosh computers and for occasional programming advice. The program which generated the multifractal simulations is due mostly to Sean Pecknold. I would also like to thank the other members of GANG for many conversations (sometimes even scientific). In particular, Tony Falco and Fred Francis helped a great deal with the photocopying, etc. in the final minutes.

The time Professor J. E. Lewis Jr. and Sofia Chavez spent reading drafts of this thesis is greatly appreciated. I thank them for their helpful suggestions. I also thank Sofia Chavez for translating the abstract into French. I have her to thank for her help with this thesis and for much more.

I thank my parents for their help and encouragement throughout this degree and my whole education. Without them, this would not have been possible.

Statement of Originality

The Scale Invariant Generator technique is a new Generalized Scale Invariance (GSI) analysis technique that was developed for this thesis. This is the first time a GSI analysis technique has been tested using multifractal simulations. The method of enhancing the spectral energy density (section 3.3.3) and the equations that state the conditions under which a linear GSI system (using a second order and fourth order bivariate polynomial to model the GSI balls) is valid (section 2.4) are published here for the first time.

Table of Contents

List of Figures

Chapter 1

INTRODUCTION

1.1 Scale Invariance as a Symmetry Principle

When the exact solutions of the dynamical equations of a system are not known (as is typically the case when the equations are nonlinear), or even when the equations themselves are not known, much can be learned of the dynamics by studying the symmetries of the system. Important types of symmetries have long included translational and rotational symmetries, but increasingly, the importance of scale invariance is being recognized. Scale invariance is found when a system is invariant under a scale transformation that is only a function of the ratio between the initial and final scales. This implies that the system has no characteristic scale (size).

It is becoming more standard to use scale invariance in the study of geophysics (even if only implicitly in the form of fractal geometry), although unfortunately, the full scope of the notion is usually underestimated since only the very special self-similar or self-affine scale transformations are employed. A system is self-similar if it is invariant under an (isotropic) magnification (or reduction) and self-affine when it is invariant under magnification followed by differential 'squashing' in a fixed direction. It has been argued elsewhere (e.g. Schertzer and Lovejoy, 1985a,b; 1987b) that the ubiquity of scale invariance can be explained since it is a fundamental property of the dynamics, and associated nonlinear partial differential equations, that describe many geophysical systems. Take, for example, the basic equations of fluid dynamics, the Navier-Stokes equations:

$$\frac{\partial \mathbf{v}}{\partial t} + (\mathbf{v}\cdot\nabla)\mathbf{v} = \frac{\nabla p}{\rho} + \upsilon\nabla^2\mathbf{v} + \mathbf{f}$$
$$\nabla\cdot\mathbf{v} = 0 \qquad (1.1.1)$$

where $\mathbf{v} \equiv$ velocity, $p \equiv$ pressure, $\rho \equiv$ density, $\upsilon \equiv$ viscosity, $\mathbf{f} \equiv$ body force.

Consider the scale transformation: $\mathbf{x} \Rightarrow \lambda^{-1}\mathbf{x}$. If this transformation is made, the equations will describe the same dynamics when the velocity is scaled as $\mathbf{v} \Rightarrow \lambda^{-H}\mathbf{v}$ (where $H \equiv$ an arbitrary scaling exponent) and the other quantities of the equation are also rescaled according to dimensional considerations. From the above it can be seen that the dynamics do not depend on the absolute size of the system; it is scale invariant. In real systems such as the atmosphere, neither the forcing (e.g. planetary scale solar heating) nor the viscosity is rescaled, hence the system will only be scaling within a finite (but possibly very large) range of scales.

Like other symmetries, scale invariance can a priori be assumed to hold unless a specific symmetry breaking mechanism exists (e.g., a force that acts at only one scale). Many geophysical fields exhibit no such mechanism over a wide range of scales. For example, in many atmospheric motions, the scaling symmetry apparently remains unbroken from large scales of 10 000 km down to the viscous dissipation scale (~1 mm)[1] and from geological scales down to milliseconds. The boundary conditions (topography, Lavallée, 1991) will not break the scaling, since they have also been shown to be scaling (i.e. they have scale invariant symmetry).

No geophysical field is exactly isotropic. For example, in atmospheric fields, there will be differential stratification due to gravity and differential rotation due to coriolis forces. Many other geophysical fields also exhibit highly anisotropic phenomena, such as ridges in sea ice, faultplanes in earthquakes and mountain ranges and rifts in topography. It is often taken for granted that the anisotropic phenomena break the scaling when, in fact, it is quite possible that they break only the self-similarity, since their effects (or they themselves) are seen over a wide range of scales. For example, evidence of scaling in the presence of gravity has been shown; the horizontal fluctuations of the wind velocity in the atmosphere show evidence of scaling in the vertical, and from dimensional analysis the (scale invariant) spectral exponent, β (see section 1.2), will be approximately $1\frac{1}{3}$ (Endlich et al., 1969; Adelfang, 1971; Schertzer and Lovejoy, 1985a) whereas in the horizontal, it is closer to the Kolmogorov $\beta = \frac{5}{3}$. Also, using a data analysis technique called 'elliptical dimension sampling', three dimensional radar rain reflectivities were shown to scale anisotropically (Lovejoy et al., 1987). Fox and Hayes

---

[1] Here the symmetry will be broken at the inner scale of turbulence, ℓ_0. However, the invariance will hold for $\ell >> \ell_0$.

(1985) and VanZandt et al. (1990) also observed that the bathymetry of the ocean and wind fluctuations, respectively, were anisotropic and studied the directional dependence of the spectral slope.

An anisotropic satellite cloud radiance (AVHRR channel 1) is shown in figure 1.1 (top). While large scale bands are oriented mostly bottom left to top right, the small scale structures are more left to right i.e. there is a clear change in orientation (and perhaps degree of stratification) from large to small scales. The anisotropy can be seen more clearly in the squared modulus of the Fourier transform of the field, the spectral energy density (bottom of figure 1.1). When the contours of the spectral energy density are vertically elongated, the field (in real space) is horizontally stratified. The contours closer to the center correspond to the large scale structure of the field while the outer contours correspond to the small scales. Note the change in the orientation of the contours as expected from the inspection of the real space image.

Considering that there is rarely strong empirical evidence of scale breaking mechanisms, and few convincing theoretical reasons to invoke them, scale invariance, in the absence of other information, must be assumed. However, there is usually no reason to assume that a specific type of scale invariance will hold e.g. self-affinity. Therefore, only the most general scale invariance should be considered, with no a priori restrictions. This requires a generalization of the definition of scale and scale transformations. In several papers, Schertzer and Lovejoy (1983, 1984, 1985b, 1987a, 1991a) present a formalism called Generalized Scale Invariance (GSI). GSI answers the question of what is the most general conditions under which two scales can be related by a scale changing operator that is only a function of the ratio of scales. Thus, GSI uses a scale transformation defined as $T_\lambda = \lambda^{-G}$, where λ is the ratio between the scales and G (called the generator) is some function which is not dependent on scale. The 'balls', which define the scale, can be of diverse shape as long as a few conditions (necessary to ensure uniqueness) are met. (All this will be discussed further in the following chapters).

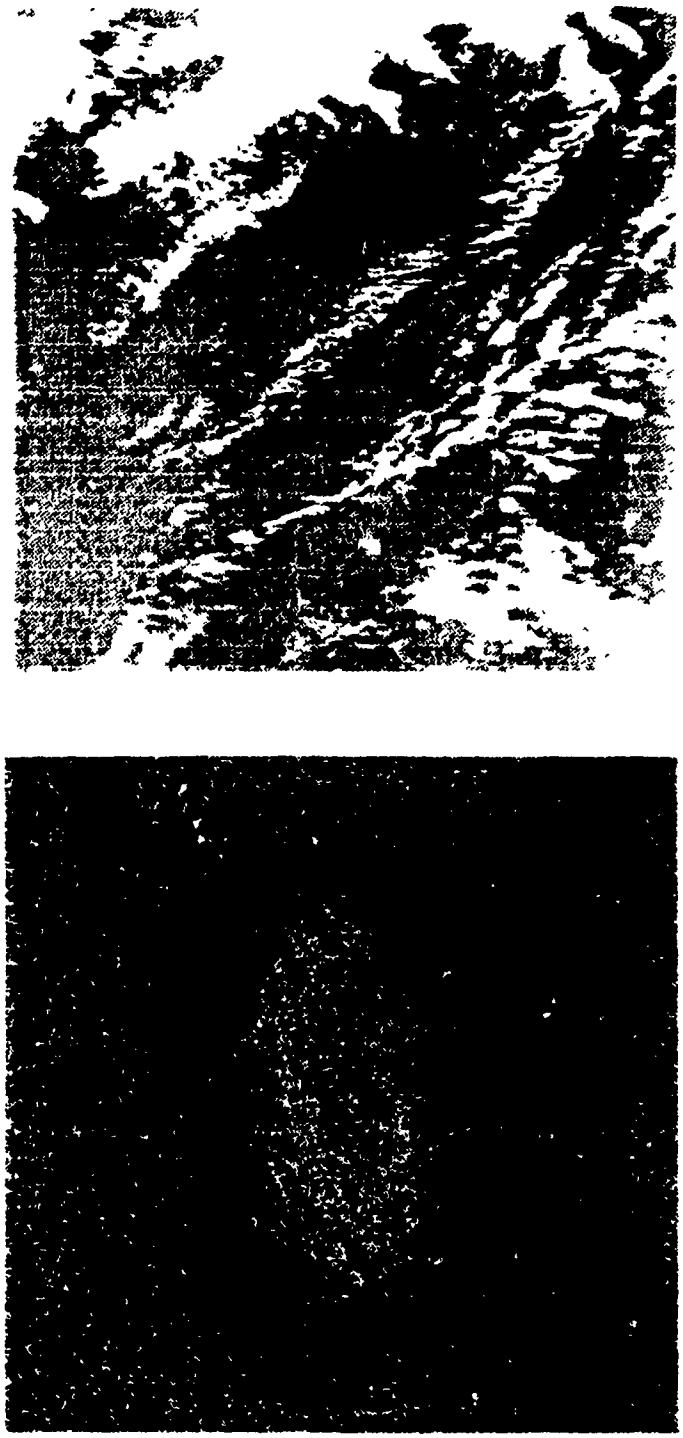

Figure 1.1 : Anisotropic satellite cloud radiance, AVHRR from NOAA-9 (top) and its spectral energy density, the modulus squared in Fourier space (bottom). The anisotropic nature of the cloud can be seen in the spectral energy density.

1.2 Scale Invariance in Geophysics

The types of scale invariance of concern in many geophysical applications relate the statistical properties of the system as it is transformed under generalized scale changes. That is, the statistical moments, that describe the probability distribution of a process, are scaling functions (i.e. they have scale invariant symmetry). In this thesis, a geophysical field whose moments are scaling will be called a scaling field. Thus, we consider scaling fields whose structure function, $S(\Delta \mathbf{x})$, (a second order statistical moment), satisfies a power-law relation with changes in scale:

$$S(T_\lambda \Delta \mathbf{x}) = \lambda^{-\xi} S(\Delta \mathbf{x}) \qquad (1.2.1)$$

where $\Delta \mathbf{x} = \mathbf{x}' - \mathbf{x}$, $\mathbf{x}'$ and $\mathbf{x}$ are any two vectors in the vector space over which the field is defined, and ξ is an arbitrary scale invariant exponent (see section 2.2). The structure function of equation (1.2.1) will be valid for statistically translationally invariant fields that are scaling under a variety of different types of scale invariance ranging from some fractal sets (e.g. with the use of indicator functions), to monofractal functions, to multifractal measures. (It may also be valid without the condition of statistical translational invariance, but only over a small range in space, over which the translational variation is negligible, see below). The statistical translational invariance makes it convenient to study the field in Fourier space, where the modulus squared of the Fourier transform of the field, the spectral energy density $P(\mathbf{k})$ (where $\mathbf{k}$ is the wave number), will be the relevant scaling quantity (see section 2.2) and will also satisfy a power-law relation.

A method that is often used to study (isotropic) scale invariance involves the isotropic energy spectrum, $E(k)$, which is found by integrating $P(\mathbf{k})$ over annuli of constant $k = |\mathbf{k}|$. If the field is isotropic and scaling, then $E(k) \sim k^{-\beta}$, where β is the (scale invariant) spectral exponent. If the anisotropy of a scaling field is not extreme, it may be 'washed-out' by the smoothing effect of the integration and thus, the scaling of the isotropic spectrum may seem to hold. The same may be said of one-dimensional energy spectra (where the data is only known in one dimension), if many realizations are averaged. Thus, a power-law isotropic energy spectrum can indicate scaling without implying isotropy. It is stressed that this (and other) isotropic methods give no

information of the anisotropy, which must be considered if the anisotropic phenomena, discussed in section 1.1 (e.g. differential stratification and rotation), are to be modeled. Anisotropy is also important since, for example, it has been argued that it explains the texture and morphology of fields (Lovejoy and Schertzer, 1985; Pflug et al., 1993). It is important to note that a break in the isotropic scaling does not necessarily indicate the field is not scaling in the general sense.

The existence of scaling has been seen in many geophysical fields using the isotropic energy spectrum and other types of isotropic scale invariance. Below, a few examples of different areas where different types of scale invariance have been studied, are included. This is only a small incomplete sample of the examples available. See Korvin (1993) for review and the books 'Non-Linear Variability in Geophysics' (Schertzer and Lovejoy, 1991) and 'Fractals in Geophysics' (Scholz and Mandelbrot, 1989) containing papers using scale invariance with geophysical applications.

Various empirical studies of the horizontal fluctuations in wind velocity in the atmosphere have shown evidence of a $\beta \approx 5/3$ scaling region in $E(k)$ (over various ranges in scale). Lilly and Petersen (1983) summarized much of the data available at the time in a graph (figure 1.2). Included in the graph of figure 1.2 are data from Nastrom and Gage (1983), Lilly and Petersen (1983), Vinnichenko (1970), Balsley and Carter (1982) and Chen and Wiin-Nielsen (1978). The scaling seems to approximately hold from less than 1 km to 10 000 km. Fritts et al. (1990) further supports the notion that the velocity fluctuations are power-law. This example is of interest since it shows no evidence of a 'meso-scale gap'. This gap would be seen as a dip in $E(k)$ in the meso-scale region. The absence of the gap contradicts the standard model of atmospheric dynamics (a three-dimensional isotropic scaling regime at small scales and a two-dimensional isotropic scaling regime at large scales with a dimensional transition in the meso-scale region). However, it is consistent with the unified scaling model of atmospheric dynamics (Schertzer and Lovejoy, 1983, 1985a,b; Lovejoy et al, 1993a) which uses GSI to postulate a single anisotropic scaling regime from large to small scales. Lovejoy et al. (1993a) further supports the unified scaling model with a systematic study of the energy spectra of satellite cloud radiances. The radiances of five wavelength channels of fifteen consecutive scenes were shown to be scaling from 160 m to 4000 km.

The spectral slope has also been used to characterize surfaces in many areas of geophysics. For instance, it has been used to study topography (Brown and Scholz, 1985;

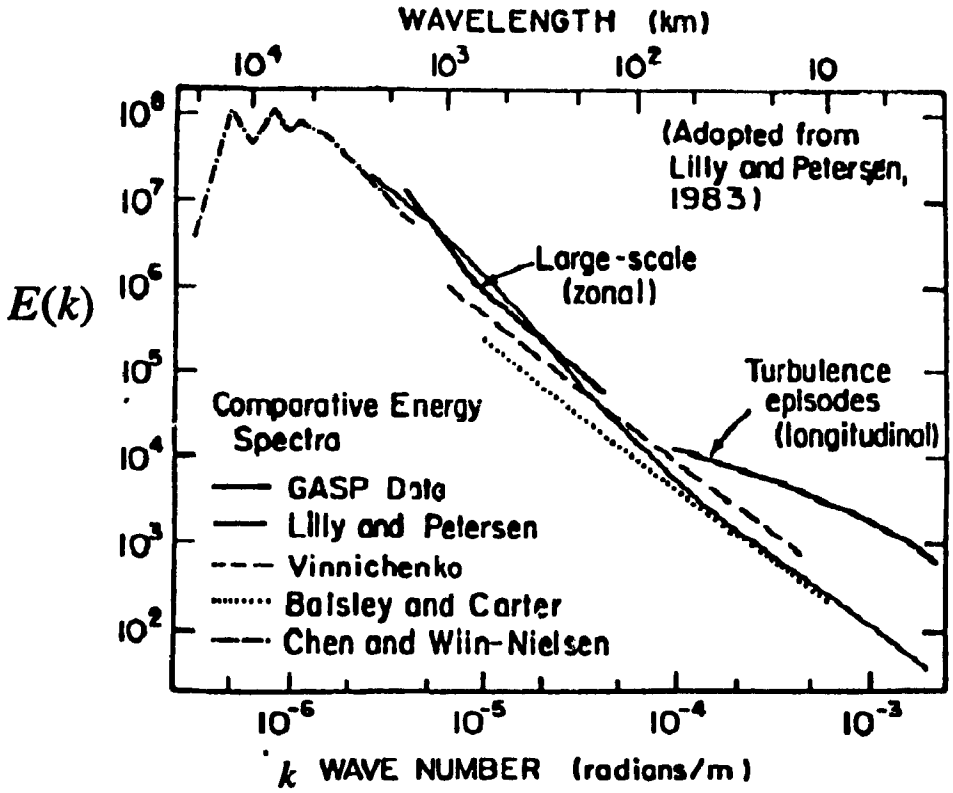

Figure 1.2 : A compilation of energy spectra of the fluctuations of the horizontal wind in the horizontal, obtained from various sources, including commerical aircraft (from Lilly and Petersen, 1983).

Sayles and Hayes, 1978), the bathymetry of the ocean (Fox and Hayes, 1985) and the profiles of the underside of sea ice (Rothrock and Thorndike, 1980).

Above, the scaling of the structure function (a second order statistical moment) was discussed. However, in order to obtain a more complete description of the statistical properties of the process (field), the scaling of all the moments is needed. Because of the initial success of fractal geometry at characterizing scaling by unique fractal dimensions (as above), it was often thought that a single parameter was sufficient to characterize all the moments. That is, the scale invariant exponents of the different moments can be written as a linear function of the moment and thus all the information of the statistical properties can be found from β. The first example of non-linear multiple scaling was given by Kolmogorov (1962) and Oboukhov (1962) who suggested that the moments of the energy dissipation, ε_λ, in fully developed turbulence depends on resolution, λ, in the following manner:

$$\langle \varepsilon_\lambda^q \rangle = \lambda^{K(q)} \qquad (1.2.2)$$

where $K(q)$ is the scale invariant exponent that is a function of the moments, q. In general, each moment, q, will have a different scale invariant exponent. Multi-scaling fields are of particular interest, since the analysis technique developed in this thesis will be tested on multifractal simulations. A further discussion (although brief) is therefore merited.

An equivalent description of multi-scaling fields (to that given directly above) states that the probability that ε_λ, at resolution λ, will exceed λ^γ is:

$$\Pr(\varepsilon_\lambda \geq \lambda^\gamma) \approx \lambda^{-c(\gamma)} \qquad (1.2.3)$$

where c is the co-dimension which is some function of $\gamma \equiv$ the order of singularity (Schertzer and Lovejoy, 1987b). Therefore, in general, there will be a unique value of c for each γ and thus an infinite hierarchy of fractal dimensions corresponding to $\gamma = [-\infty, \infty]$ where $\gamma \in \Re$. Scaling fields with this property are multifractals and they are characterized by their extreme variability (Schertzer and Lovejoy, 1987b).

In general, $c(\gamma)$ is of an undetermined form and therefore requires an infinite number of parameters for its determination. However, if a multifractal process exhibits a sufficient number of non-linear interactions over a range of scales, much of the detail of the process may be 'washed out' with the consequence that the statistics of its multifractal generator will be described by (special) Lévy distributions (Schertzer and Lovejoy, 1987b, 1989b, 1991a; Schertzer et al., 1991b; Brax and Peshanski, 1991). These multifractals are 'universal'. Only three parameters are necessary for a full characterization of the probability distribution of a universal multifractal: α, C_1, and H. α ($0 \leq \alpha \leq 2$) is a measure of the degree of multifractality ($\alpha = 0$: monofractal, $\alpha = 2$: log normal multifractal), C_1 is a measure of the sparseness of the mean of the field and H is a measure of the degree of non-conservation of the field (see Schertzer and Lovejoy, 1991a). Many geophysical (and other) fields have recently been shown to be well represented by universal multifractals. Included is a table (Table 1.1) of some of these results.

Field		α	C1	H	Range of scales	References
Cloud radiances	visible	1.35	0.15	0.3	160m→ 4000km	Tessier et al. (1993a)
	infrared	1.35	0.15	0.4	160m→ 4000km	Tessier et al. (1993a)
	microwave	1.60	0.10	0.35	160m→ 4000km	Lavallée et al. (1993)
Rain	radar	1.35	0.30	0.0	30m→ 64km	Tessier et al. (1993a)
	gages	1.35	0.20	0.0	50km→ 4000km	Tessier et al. (1993a)
Sea Ice (radar)		1.7	0.05	0.0	50m→25km	Francis et al. (1993)
Ocean surface (0.95μm)		1.1	0.25	0.35	1m→50m	Tessier et al. (1993b)
Topography		1.8	0.05	0.5	50m→1000km	Lavallée (1991)
Seismicity		1.35	1.9	0.0	1km→500km	Hooge (1993)
DioxinPollution (Seveso)		1.2	0.8	-0.2	30m→5km	Salvadori et al. (1993)
Wind	windtunnel	1.30	0.25	1/3	1ms→ 1s	Schmitt et al. (1992)
	atmosphere	1.45	0.23	1/3	1ms→ 1s	Schmitt et al. (1993)
Temperature		1.20	0.35	0.30	0.1s→ 1000s	Schmitt et al. (1992)
Earth's magnetic field		1.9	0.15	0.75	1600m→200km	Lovejoy et al. (1993b)

Table 1.1 : Multifractal parameters determined for a variety of fields with the corresponding ranges of scale. The accuracy of most parameters is ~ ±0.1 (adapted from Pecknold et al., 1993).

1.3 Generalized Scale Invariant Analysis Techniques

All the above evidence supports the use of scale invariance in the analysis of geophysical fields and the necessity of introducing more general notions of scale and scale transformations. Generalized Scale Invariance (GSI) encompasses these general notions. However, in order for GSI to be useful, it requires the knowledge of its basic elements: the scale changing operator and the scale defining balls. In the isotropic case, these are known(the generator, G, is the identity and the balls are concentric spheres), but for GSI, special analysis techniques must be developed. However, the generality of GSI causes problems in analysis. If GSI in its most general form were assumed, the generator, G, would be described by an infinite number of parameters (i.e. G would be a stochastic, nonlinear function, Schertzer and Lovejoy, 1991a). Since the usefulness of GSI lies in the ability to estimate the generator, it is necessary to work with an approximation. In this thesis, linear GSI will be studied.

Linear GSI approximates T_λ as a linear transformation. In this case, G is a matrix (thus is described by D^2 parameters where D is the dimension of space) and a functional form of T_λ can be found. Linear GSI is still general enough to model a diversity of situations (see figures of Chapter 2 and 4). Self-similarity is the special case when G is the identity matrix and self-affinity is when G is diagonal with unequal elements. Even though in linear GSI, G is independent of position, it will still be a valid approximation to any scaling field if only a small enough range is considered. Pflug et al. (1993) showed that linear GSI holds approximately in clouds by studying the spectral energy density of satellite cloud radiances and showed the potential of using the values of the GSI generator for structural and textural analysis. In general, it will be necessary to study non-linear GSI and/or to analyze the field in real space (as opposed to the spectral energy density). Nevertheless, in principle, information about the full non-linear GSI can still be determined by considering a series of linear approximations.

There are a number of possible ways to estimate G. The goal is to find a method that is accurate while being computationally tenable. In Pflug et al. 1991a,b and 1993 (see also Lovejoy et al., 1992), a cumbersome, but workable, technique called the Monte Carlo Differential Rotation (MCDR) method was developed and used to estimate the linear GSI parameters of satellite cloud radiances. The MCDR involves, at least, an eight-dimensional parameter space that is reduced to practical proportions by estimating

(with unknown accuracy) many of the parameters before the obligatory search of the parameter space. In this thesis, the emphasis is on the development of an alternative technique, which separates the estimation of the generator parameters and the estimation of the parameters of the scale defining balls needed in the scale invariant system. Thus, the technique is called the 'Scale Invariant Generator' technique (SIG) because it can quantify the scale invariant generator, G, by searching a three-dimensional parameter space, without any knowledge of the ball parameters.

The technique is tested on multifractal (scale invariant) simulations (see Wilson et al., 1991 and Pecknold et al., 1993) that are constructed with known scale invariant generators. Multifractal fields were chosen as the test fields because we feel that they are the most relevant in geophysics and also, due to the extreme variability of multifractals, they will be more difficult to analyze than other scale invariant fields (e.g. monofractals, such as 'fractional Brownian motion'). The Scale Invariant Generator technique is not restricted to multifractals and can be used, without modification, to analyze the spectral energy density of any (scaling) field (or, using indicator functions, anisotropic fractal sets), regardless of the type of scaling expected.

The technique also includes a method of anisotropically 'enhancing' the image in Fourier space while maintaining the scaling properties of the field. This method may have applications in image processing and data compression.

1.4 The Purpose and Structure of Thesis

The purpose of this thesis is to develop the Scale Invariant Generator technique (SIG), an analysis technique that finds the linear Generalized Scale Invariance parameters that best describe a scaling field. The emphasis is on testing the accuracy of the technique by applying the analysis to a variety of simulated fields with fully known properties. Details of the technique are investigated so that the technique can be made numerically efficient. The purpose, however, is not to theoretically prove the optimum efficiency, but to simply obtain a reasonably efficient technique that produces valid estimates mainly in parameter ranges relevant to common geophysical fields such as clouds, topography, sea ice, etc. Six actual geophysical fields (satellite radiances of clouds and sea ice) are analyzed for the purpose of testing the applicability of the

technique. Many more images must be analyzed if conclusions are to be made concerning the full extent of the hypothesis of linear GSI in geophysics.

The thesis is structured as follows. Chapter 2 contains a discussion of Generalized Scale Invariance in a general sense and also in application to geophysics via the structure function . Also, in section 2.4, there is a discussion of the restrictions on a scale invariant system. In Chapter 3, analysis techniques for Generalized Scale Invariance are discussed. The (previously published) Monte Carlo Differential Rotation method is briefly presented, while the (new) Scale Invariant Generator technique is discussed in great detail. Chapter 4 contains results of SIG on a variety of multifractal simulations and Chapter 5 contains results of the analysis on actual geophysical fields. The conclusions are stated in Chapter 6.

Chapter 2

GENERALIZED SCALE INVARIANCE

2.1 The Elements of a Generalized Scale Invariant System

Generalized Scale Invariance (GSI) is a formalism which states the most general conditions under which large and small scales can be related without introducing a characteristic size. That is, the different scales are related by a scale changing operator that is only a function of the ratio of scales. This generalization is measure based. The notion of scale of a vector may be defined without introducing a metric; only a notion of integration over sets is necessary.

A scale invariant system requires the definitions of the following three elements: (1) a scale changing operator, T_λ, (2) a family of balls, B_λ, and (3) a measure of scale, φ, (Schertzer and Lovejoy, 1985b, 1988). In order to see the nature of a generalized scale invariant system, it is instructive to investigate these elements in more detail.

The scale changing operator, T_λ, is the reduction operator. It is the rule which relates vectors of different scales by only their ratio of scales, λ, therefore, it does not impose any characteristic size to the system. This implies that T_λ must satisfy the properties:

$$T_{\lambda_3} = T_{\lambda_1} T_{\lambda_2} = T_{\lambda_2} T_{\lambda_1} \tag{2.1.1}$$

if and only if: $\lambda_3 = \lambda_1 \lambda_2$, for any λ_1, λ_2 and λ_3, (see figure 2.1) and

$$\left(T_{\lambda_1} T_{\lambda_2}\right) T_{\lambda_3} = T_{\lambda_1} \left(T_{\lambda_2} T_{\lambda_3}\right) \tag{2.1.2}$$

where T_{λ_i} are the scale transformations corresponding to a scale change of $\lambda_i = [1,\infty]$. The identity is the operator for which $\lambda = 1$.

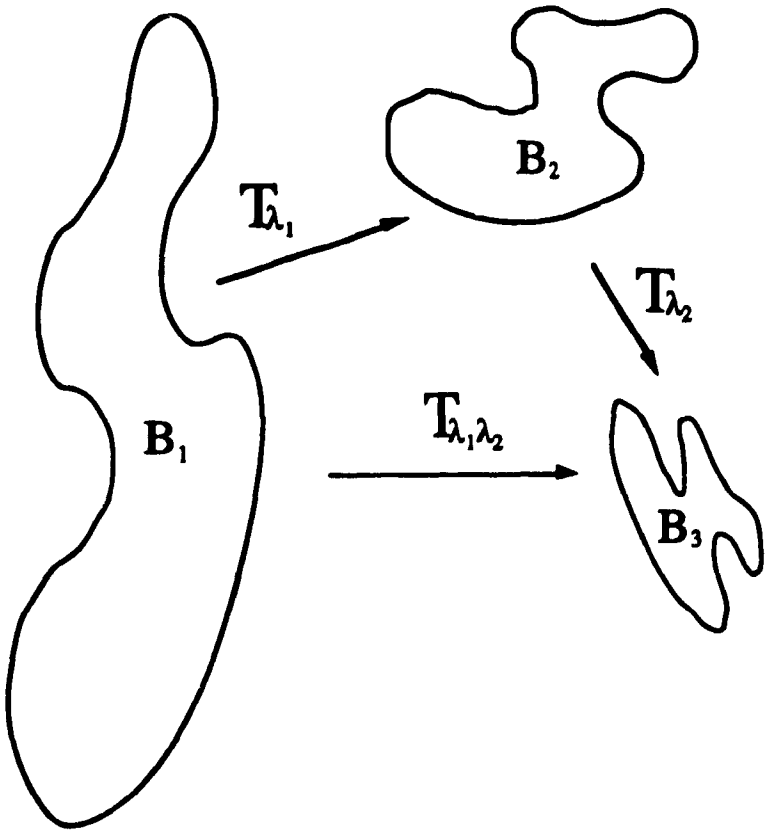

Figure 2.1 : Group properties of the scale changing operator. *B* are balls of the scale invariant system.

These properties imply that the set of scale changing operators forms an infinite one parameter Abelian multiplicative semi-group. Therefore, T_λ can be written as:

$$T_\lambda = \lambda^{-G} \tag{2.1.3}$$

where G is the generator of the group and λ is the scale ratio between any two scales (Schertzer and Lovejoy, 1985b). The only restriction on G, (besides minor ones to ensure a valid GSI system, see section 2.4), is that it not be a function of scale. G could possibly be a stochastic non-linear function of time and space (Schertzer and Lovejoy, 1989a, 1991a). Note that a priori it need not be required that an inverse, $(T_\lambda)^{-1}$, exists (i.e. T_λ form a *semi*-group). For example, the scale invariant cascades, that produce multifractal

fields, typically go from large to small scales (i.e. an inverse need not be defined). However, in many cases (such as in linear GSI, see section 2.3), an inverse will exist and $(T_\lambda)^{-1} = T_{\lambda^{-1}}$. These are the transformations corresponding to the scale changes $\lambda =]0,1]$.

A ball, B_λ, of a GSI system is the set of all vectors of a given scale (labeled by λ). Alternatively, it can be said that all the position vectors associated with a ball are of the same scale. A family of balls (Schertzer and Lovejoy, 1985b) is a set of ordered balls (one for every scale) which covers the relevant vector space by uniquely assigning all the vectors to a scale. All pairs of balls, B_{λ_2} and B_{λ_1} (that are members of a family of balls), must satisfy the property $B_{\lambda_2} = T_\lambda B_{\lambda_1}$, where $\lambda = \lambda_2/\lambda_1$ i.e. operating T_λ on all the vectors associated with B_{λ_1} must form another ball, B_{λ_2}. It can be said that the balls order the vectors by increasing λ. However, the balls, and thus the corresponding vectors, are only related by their scale ratio, which, as yet, cannot be interpreted as a relative *size*. It should be noted that the necessity of assocciating a notion of size with the balls (and thus the vectors) implies that the balls must be measurable i.e. when a weight is assigned to them (most easily using a normal Lebesque measure), they will become measures.

It is possible to generate the whole family of balls from any one member by operating T_λ on that ball for all possible values of the scale ratio. One ball will be generated for every value of the scale ratio. Therefore, once one ball is known, all others can be found if T_λ is known. It is convenient to choose one ball to which all the other balls will be compared. This ball will be called the unit ball, B_1 (Schertzer and Lovejoy, 1985b, 1988). The family of balls will then be $B_\lambda = T_\lambda B_1$. It should be stressed that the unit ball has no unique characteristics and that any B_λ may be chosen as the unit ball. For example, if $B_1' \in B_\lambda$ such that $B_1' = T_{\lambda_1} B_1$, where λ_1 is the scale ratio between B_1' and B_1, then B_1' can also be defined as the unit ball since $B_{\lambda'} = T_{\lambda'} B_1'$ also defines the family of balls, where $\lambda' = \lambda/\lambda_1$, i.e.

$$B_{\lambda'} = T_{\lambda'} B_1' = T_{\lambda'} T_{\lambda_1} B_1 = T_\lambda B_1 = B_\lambda$$

where $T_{\lambda'} T_{\lambda_1} = T_\lambda$ since $\lambda' \lambda_1 = \lambda$ as required by (2.1.1).

To complete the scale invariant system, we must define how to associate a size with λ. The definition of scale, φ, must be such that it can assign a unique positive real number, that monotonically increases from low to high scales, to every ball, B. Any consistent definition is equally valid; the exact definition used is a matter of convenience or convention. The definition need not be restricted to being metric based, but may require only that an integral be defined over the balls i.e. measure based definitions will be allowed.

Thus we may use the volume bounded by a ball raised to some power to define our measure of scale, φ. It is worthwhile to note that any positive power of the volume would be a consistent definition. The exact power that will be used is discussed below.

The volume of a ball, B, in D dimensions[1], $\Phi^D(B)$, scales as $\lambda^{-D_{el}}$, where $D_{el} = Trace(G)$ is the elliptical dimension (Schertzer and Lovejoy, 1984). That is,

$$\Phi^D(T_\lambda B_1) = \lambda^{-D_{el}} \Phi^D(B_1) \tag{2.1.4}$$

and φ_{el} is defined such that:

$$\varphi_{el}{}^{D_{el}}(B) \equiv \Phi^D(B) \tag{2.1.5}$$

Therefore, if $B_\lambda = T_\lambda B_1$,

$$\varphi_{el}{}^{D_{el}}(B_\lambda) = \Phi^D(B_\lambda) = \lambda^{-D_{el}} \Phi^D(B_1)$$
$$\varphi_{el}(B_\lambda) = \Phi^{1/D_{el}}(B_\lambda) = \lambda^{-1} \Phi^{1/D_{el}}(B_1)$$

$$\varphi_{el}(B_\lambda) = \lambda^{-1} \varphi_{el}(B_1) \tag{2.1.6}$$

Thus the scale ratio can be defined:

$$\lambda = \frac{\varphi_{el}(B_1)}{\varphi_{el}(B_\lambda)} \tag{2.1.7}$$

---

[1] i.e. if D=2 then $\Phi(B)$ is the square root of the area

i.e. the definition of scale is:

$$\varphi = \varphi(B) = \varphi_{el}(B) = \Phi^{1/D_{el}}(B) \qquad (2.1.8)$$

(the volume of the ball to the power of $1/D_{el}$) for a magnification in scale.

Above, it was stated that any power of the volume may be chosen as a definition of scale. This can be shown in an example. If a GSI system has T_λ as its scaling operator, with G as its corresponding generator and φ as its definition of scale, then $\varphi' = \varphi^p$ and $G' = G/p$ form an equally good GSI system. If $T_\lambda' = (\lambda')^{-G'}$,

where $$\lambda' = \frac{\varphi'(B_1)}{\varphi'(B_\lambda)} = \frac{\varphi^p(B_1)}{\varphi^p(B_\lambda)} = \lambda^p$$

$$\Rightarrow \quad T_\lambda' = (\lambda^p)^{-G'}$$

then, if $G' = \frac{G}{p}$, $T_\lambda = T_\lambda'$.

This implies that the primed and unprimed systems are equivalent and thus the primed system is valid. Note that this also implies a different $D_{el} \Rightarrow D_{el}/p$. It can be seen that, given our definition of scale (equation 2.1.8), the choice of the power of the volume determines D_{el}, or conversly, the choice of D_{el} determines the definition of scale. As stated earlier, this choice is a matter of convenience or convention.

D_{el}, the elliptical dimension can be described as the effective dimension of the space, (for given a defintion of scale, since D_{el} depends on this choice). For example, using horizontal distance as scale, a three-dimensional field, that is infinitely stratified, has $D_{el} = 2$. If it is completely non-stratified, it has $D_{el} = 3$. It is possible that the stratification due to gravity will cause the atmosphere to have some intermediate value (see introduction). Lovejoy and Schertzer (1987) found empirically that $D_{el} = 2.22$ in rain and cloud radar reflectivities.

Figure 2.2 shows examples of different GSI systems. The special isotropic case is when the generator is the identity (G=**1**) and the (metric based) definition of φ is the modulus (conventional length) of the vectors that form the balls, which are circles (in the

two-dimensional case shown). Note that the measure based definition of φ is equivalent. The square root of the area can be a consistent definition and it is proportional to the modulus of the vectors that form the ball.

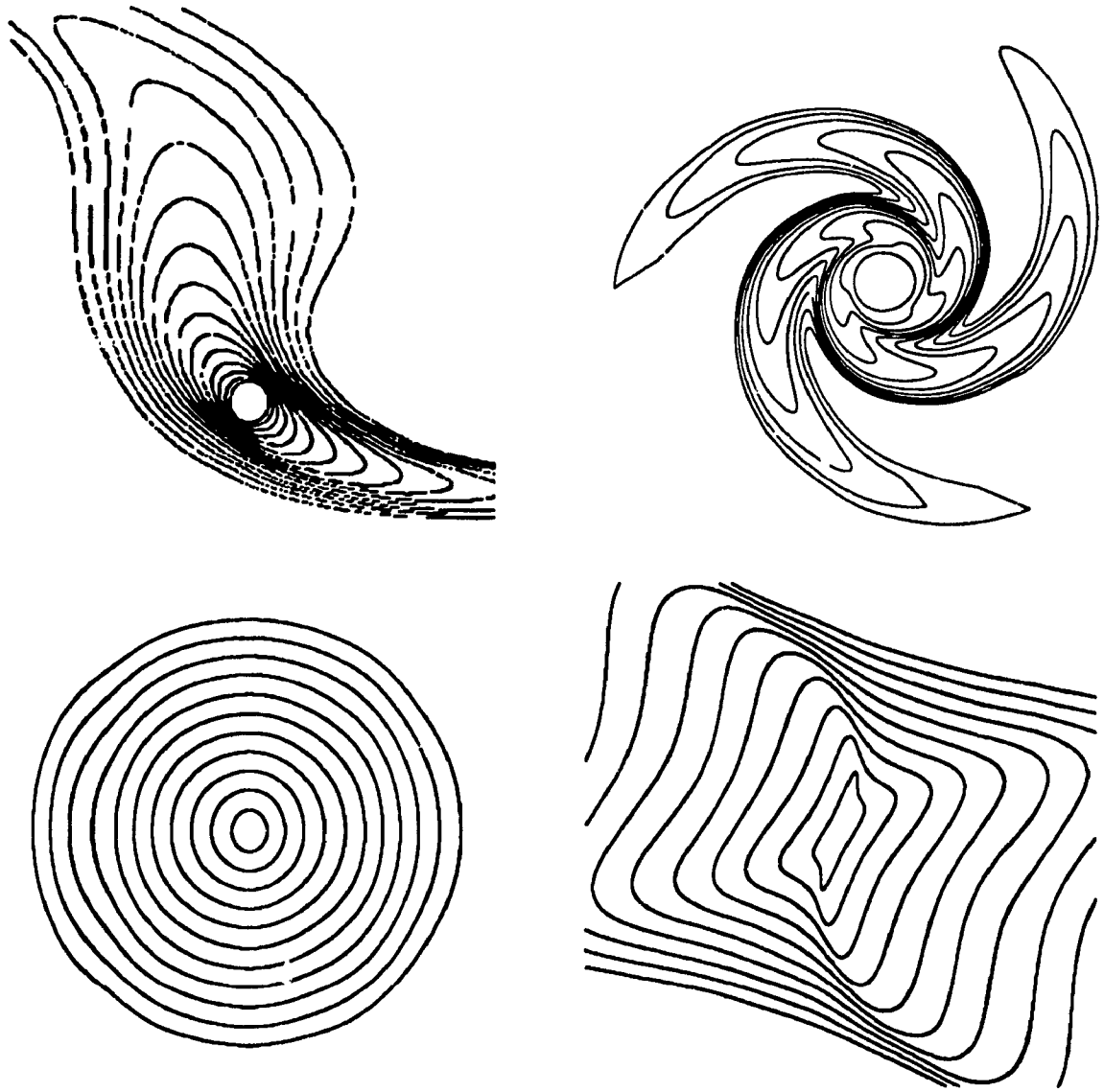

Figure 2.2 : Examples of balls: Non-linear GSI (top, left and right) from Schertzer and Lovejoy, 1985b. Isotropic case (bottom left). Linear GSI (bottom right).

Before continuing, a clarification may be required. If all the vectors associated with the ball B_{λ_1} are operated on by T_λ, the vectors $\mathbf{x}_2$ will form another ball, B_{λ_2}. The scale of B_{λ_1}, λ_1, and the scale of B_{λ_2} will be related by $\lambda_2 = \lambda^{-1}\lambda_1$. For a valid GSI

system, this will hold for any pair of members of the family of balls such that all vectors are uniquely related to a scale.

An alternative way of looking at the problem is to invoke the idea of a 'trajectory'. If a vector is related to another by T_λ (e.g. $\mathbf{x}_2 = T_\lambda \mathbf{x}_1$), then it is said that they lie on the same trajectory. More completely, a trajectory can be generated by (repeatedly) operating T_λ, with generator G, on a vector while varying λ over all possible values. One vector for every λ will be generated. These vectors will trace out a continuous curve which is called a trajectory. Note that the same trajectory will be generated if any vector in the trajectory is chosen as the initial vector, when the same steps are followed. This is a consequence of the group properties of the T_λ. Each vector of the field is a member of one and only one trajectory and a given G will generate a whole series of trajectories as in figure 2.3. Also, there is a unique set of trajectories for every G.

It can be said that the trajectory can be generated from a vector by T_λ with the *parameter* λ. This means a trajectory can be created with only knowledge of G and independently of the family of balls. That is, as yet, the vectors have not been associated to a ball. If a scale is imposed at some point along a trajectory, it is then defined for all vectors along the trajectory. e.g. if $\mathbf{x}_1$ and $\mathbf{x}_2$ are related by T_λ, and if a scale, λ_1, is imposed at $\mathbf{x}_1$, then

$$\lambda_2 = \lambda^{-1}\lambda_1 \tag{2.1.9}$$

since $\lambda = \lambda_1 / \lambda_2$ where λ is known since it is the parameter relating vectors along a trajectory. Therefore, once the trajectories are known, a scale invariant system is generated when a scale is imposed on one, and only one, vector on every trajectory with the restriction that the vectors of this scale must form a measurable ball. This imposed scale is the unit ball. For the above conditions to be observed, there are certain restrictions on G which are discussed in section 2.4.

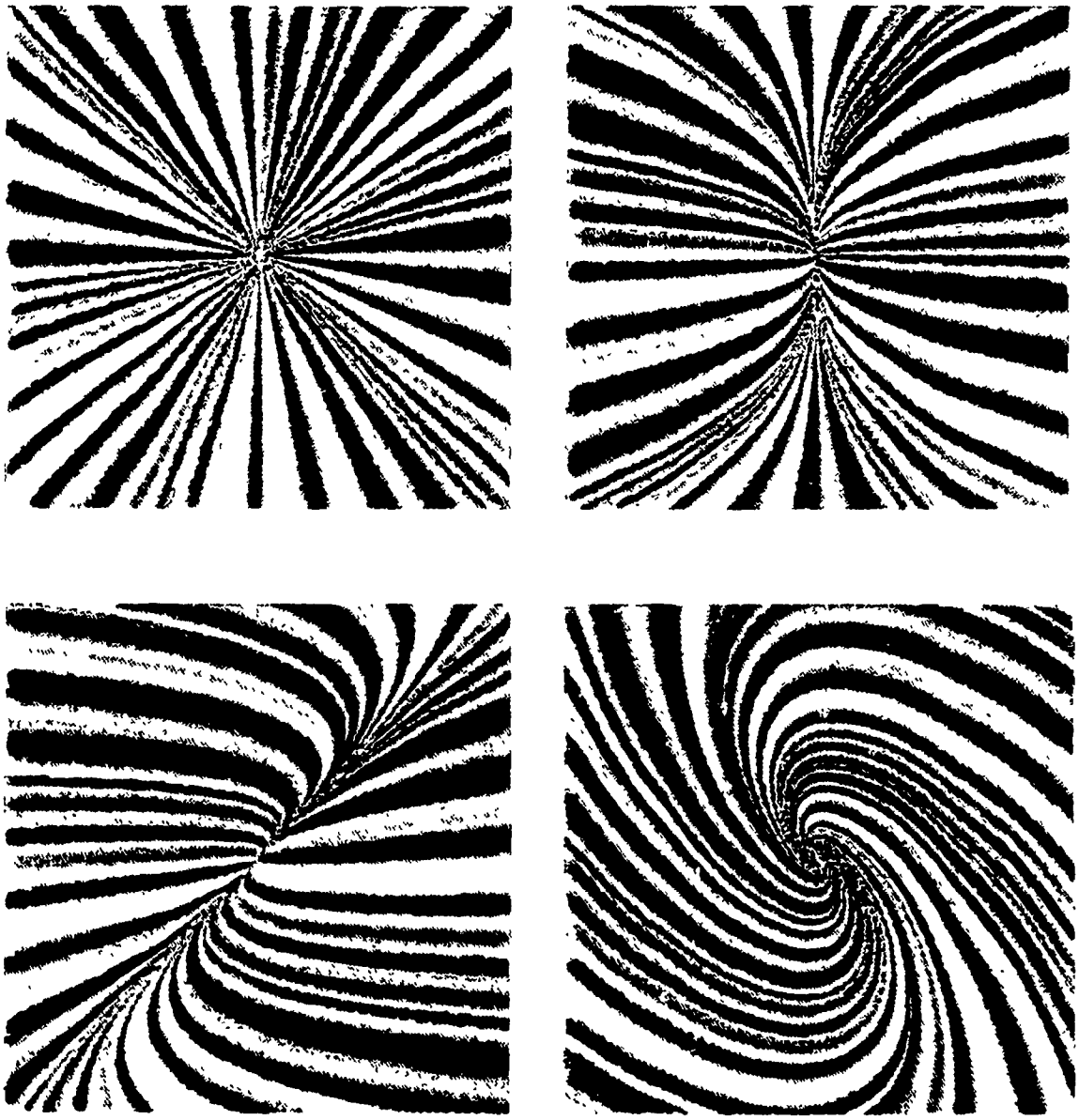

Figure 2.3 : Examples of trajectories for the isotropic case (top left), for the self-affine case (top right) and for two cases of linear GSI (bottom left and right). Different colors represent different trajectories (starting in the center).

2.2 Generalized Scale Invariance for Geophysical Applications

In geophysical applications, the scaling of the structure function:

$$S(\mathbf{x},\Delta\mathbf{x}) = \left\langle [f(\mathbf{x}) - f(\mathbf{x}+\Delta\mathbf{x})]^2 \right\rangle \qquad (2.2.1)$$

of a field, $f(\mathbf{x})$, is often studied ($\mathbf{x}$ is a position vector and $\Delta\mathbf{x}$ is a lag with respect to $\mathbf{x}$ and '$\langle\ \rangle$' denote an ensemble average quantity). If a scaling field is statistically translationally invariant, then the structure function is independent of $\mathbf{x}$ and will scale as:

$$S(T_\lambda \Delta\mathbf{x}) = \lambda^{-\xi} S(\Delta\mathbf{x}) \qquad (2.2.2)$$

where ξ is the scaling exponent and T_λ is the scale changing operator. The structure function, and thus the scaling, is defined as an average over an ensemble of realizations (e.g. an average over all the possible cloud scenes that can be generated with the same scaling properties, where a realization is one particular cloud scene). Therefore, the scaling is not expected to hold exactly on any given realization.

Assuming statistical translational invariance, it is convenient to study the scaling in Fourier space. The relevant scaling quantity is the spectral energy density, which is the Fourier transform of the auto-correlation function, or equivalently, the modulus squared of the Fourier amplitude of the field:

$$P(\mathbf{k}) = |F(\mathbf{k})|^2 \qquad (2.2.3)$$

where $F(\mathbf{k})$ is the Fourier transform of $f(\mathbf{x})$ and $\mathbf{k}$ is the wave number. Given the independence of the structure function with $\mathbf{x}$, linear GSI (see section 2.3) will be used. Note that many geophysical fields of interest do not satisfy the condition of statistical translational invariance (e.g. atmospheric motions, since coriolis forces are a function of latitude). However, in many cases, it is plausible to assume that the assumption will hold over a small range. Therefore, if the field does not globally statisfy the assumption of statistical translational invariance, in principle, it is possible to consider a series of sub-regions of the field, where the assumption will be expected to hold.

The spectral energy density of a scaling field whose structure function satisfies equation (2.2.2) will have the property:

$$\left\langle P\left(\tilde{T}_\lambda \mathbf{k}\right)\right\rangle = \lambda^{-s}\langle P(\mathbf{k})\rangle \qquad (2.2.4)$$

where $\tilde{T}_\lambda = \lambda^{\tilde{G}}$ is the scale changing operator in Fourier space and $s = \xi + D_{el}$ is the anisotropic scaling exponent. $\tilde{G} = G^T$ is the generator in Fourier space, and in the case of linear GSI, is equivalent to the transpose of the real space generator (Schertzer and Lovejoy, 1991a; Pflug, 1991a). Since we will deal exclusively in Fourier space, the tilda will be dropped with the understanding that we are referring to the Fourier space version of the GSI elements.

Since equation (2.2.4) applies to position vectors, $\mathbf{k}$, rather than the relative vectors, $\Delta\mathbf{x}$, the balls can now be given a physical interpretation. A scaling spectral energy density will be constant on the perimeter of the balls and thus the balls can be defined as the volume bounded by a contour of $\langle P\rangle$ (see Figure 2.4). Each ball will represent a contour of $\langle P\rangle$ and the amplitudes of B_{λ_1}, $\langle P_{\lambda_1}\rangle$ and that of B_{λ_2}, $\langle P_{\lambda_2}\rangle$ will be related by $\langle P_{\lambda_2}\rangle = \lambda^{-s}\langle P_{\lambda_1}\rangle$. This will hold for any pair of contours of $\langle P\rangle$. The balls can take on any shape as long as the GSI system remains valid (i.e. each vector is related to one, and only one, measurable ball). Thus it can be seen that the conventional length of a vector is no longer an adequate definition of scale.

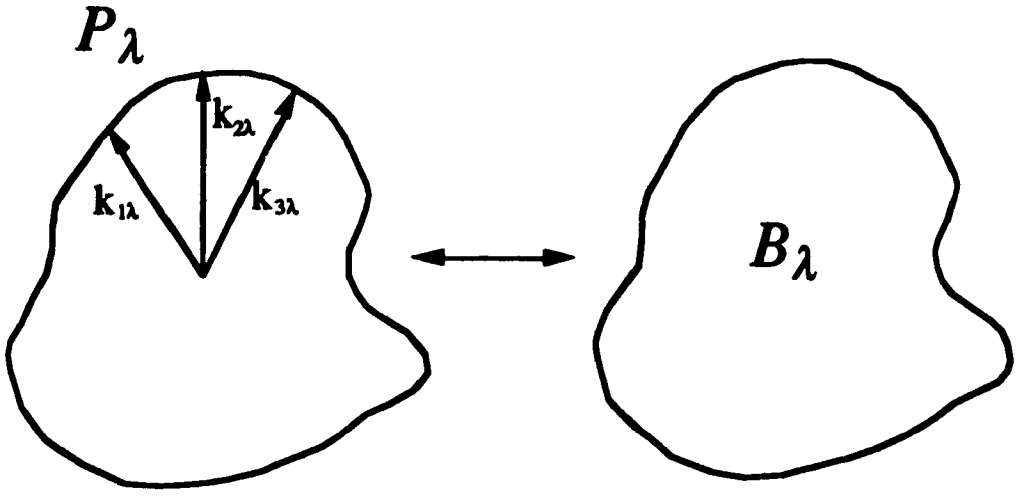

Figure 2.4 : The balls of the GSI system are related to the contours of a scaling energy spectral density as depicted above. For instructive purposes, three of the vectors that are associated with the contours, and thus the balls, are shown.

Invoking, once again, the concept of trajectory: if the amplitude of $\langle P \rangle$ is known for one vector along the trajectory, it is known for *all* vectors along the trajectory, via equation (2.2.4). This is a vector equation and does not depend on the family of balls. It is this concept that will be used in the Scale Invariant Generator technique discussed in section 3.3.

2.3 Linear Generalized Scale Invariance

For the purpose of analysis, it is useful to investigate the case when the scale changing operator is approximated by a linear transformation: linear Generalized Scale Invariance (Schertzer and Lovejoy, 1985b). In linear GSI, G is a matrix and thus has D*D parameters (where D is the dimension of space). It is convenient to discuss linear GSI, in a format analogous to that of section 2.1, by investigating the consequences of the approximation on the three essential elements needed in a scale invariant system: a family of balls (a unit ball), the scale changing operator, and a measure of scale.

The family of balls is needed to describe the contours of constant scale, where the boundary of a ball is some continuous closed curve. Although it is theoretically possible to use any form of equation to describe the curve, it is useful to choose a form that is invariant under the scale changing operation. This simply means that if the equation describing B_1 is of a certain form, and $B_2 = T_\lambda B_1$, then B_2 is of the same form with different coefficients. In the case of linear GSI, this means that the form of the equation remains invariant under linear transformations. This leads to the consideration of bivariate polynomials. Noting that the spectral energy density, $P(\mathbf{k})$, of real fields, must satisfy $P(\mathbf{k}) = P(-\mathbf{k})$, there will be a restriction to polynomials of even order. Again, the most general case would be a polynomial of infinite order, however, for the purpose of the analysis, an approximation is needed. In the case of GSI in two dimensions, the two most simple even order bivariate polynomials are the second and fourth order equations:

$$Ax^2 + 2Bxy + Cy^2 = 1 \tag{2.3.1}$$

$$Ax^4 + 2Bx^3y + Cx^2y^2 + 2Dxy^3 + Ey^4 = 1 \tag{2.3.2}$$

where A, B, C, D, E are real numbers and x, y are the coordinate axes (for simplicity $k_x \Rightarrow x$, etc.).

For equation (2.3.1), the condition that the equation describes a closed curve imposes the constraints :

$$A, C > 0 \quad \text{and} \quad AC - B^2 > 0 \tag{2.3.3}$$

Under these conditions, the equation describes an ellipse or a circle. It is useful to transform equations (2.3.1) and (2.3.2) to polar form by making the substitution:

$$\mathbf{x} = \begin{pmatrix} x \\ y \end{pmatrix} = \begin{pmatrix} r\cos\theta \\ r\sin\theta \end{pmatrix} \tag{2.3.4}$$

Using basic trigonometric identities, the polar form of equation (2.3.1) may be written as:

$$r = \left[r_0 + a_1 \cos 2\theta + b_1 \sin 2\theta\right]^{-1/2} \tag{2.3.5}$$

where $$r_0 = \frac{1}{2}(A + C), \quad a_1 = \frac{1}{2}(A - C) \quad \text{and} \quad b_1 = B \tag{2.3.6}$$

The constraints (2.3.3) are: $r_0 > 0$ and $r_0^2 > a_1^2 + b_1^2$.

Similarly, the polar form of equation (2.3.2) is:

$$r = \left[r_0 + a_1 \cos 2\theta + b_1 \sin 2\theta + a_2 \cos 4\theta + b_2 \sin 4\theta\right]^{-1/4} \tag{2.3.7}$$

The second order equation (2.3.1) or (2.3.5) is that of an ellipse. Therefore, the family of balls is a subset of the family of ellipses. The fourth order equation (2.3.2) or (2.3.7) is the next level of generalization. By inspection of the spectral energy densities of actual satellite radiances of clouds and by Pflug (1991a), it was concluded that although the second order equation is adequate for many cases, a more general form is sometimes needed.

If there exists a scale where the field is isotropic, the corresponding ball will be spherical (circular for GSI in two dimensions). This scale will be called a 'sphero-scale' (Schertzer and Lovejoy, 1983, 1984). In the case of linear GSI where a sphero-scale exists, all the balls will be of the form of equation (2.3.1). Since linear GSI with a sphero-scale is the most simple case, it will be used often as an example. See figures 2.5 and 2.6 for examples of scaling spectral energy densities where the balls are described by the second order equation (figure 2.5) and by the fourth order equation (figure 2.6).

Since satellite radiances are a form of data that will often be analyzed, GSI in two dimensions will be examined. G will be a 2 X 2 matrix. G will be written as a linear combination of the basis of two dimensional matrices (pseudo-quaternions, Schertzer and Lovejoy, 1985b; Lovejoy and Schertzer, 1985):

$$G = d\mathbf{1} + c\mathbf{K} + f\mathbf{J} + e\mathbf{I} \tag{2.3.8}$$

where $\mathbf{1}=\begin{pmatrix}1 & 0\\ 0 & 1\end{pmatrix}$, $\mathbf{K}=\begin{pmatrix}1 & 0\\ 0 & -1\end{pmatrix}$, $\mathbf{J}=\begin{pmatrix}0 & 1\\ 1 & 0\end{pmatrix}$, $\mathbf{I}=\begin{pmatrix}0 & 1\\ -1 & 0\end{pmatrix}$

Thus,
$$G=\begin{pmatrix}d+c & f+e\\ f-e & d-c\end{pmatrix} \tag{2.3.9}$$

Written as such, the parameters, d, c, f, and e, have more significance.

The diagrams of figure 2.7 show the effect of the parameters in the case of linear GSI with a sphero-scale. d determines how the volume of the balls changes with scale since $\mathrm{Trace}(G) = 2d = D_{el}$. D_{el} will be chosen to be 2, hence d=1 (see discussion below). In the diagrams, it can be seen that c determines the relative scaling of the axes. The trajectories tend more toward the horizontal with increasing c and thus the scale defining ellipses become more stratified. The matrix **J**, of above, is a reflection across a plane oriented 45 degrees with respect to both x and y axes. Therefore, the larger f becomes, the more the trajectories tend toward the plane of reflection. This also means it has a stratifying effect. Since the matrix **I** is a rotation, e is a measure of the degree of rotation.

With G written as in equation (2.3.9), a functional form of T_λ can be found:

$$T_\lambda = \lambda^G = \lambda^d \lambda^{(G-1d)} \quad \Rightarrow \quad T_\lambda = \lambda^d \exp[(G-1d)\ln\lambda] \tag{2.3.10}$$

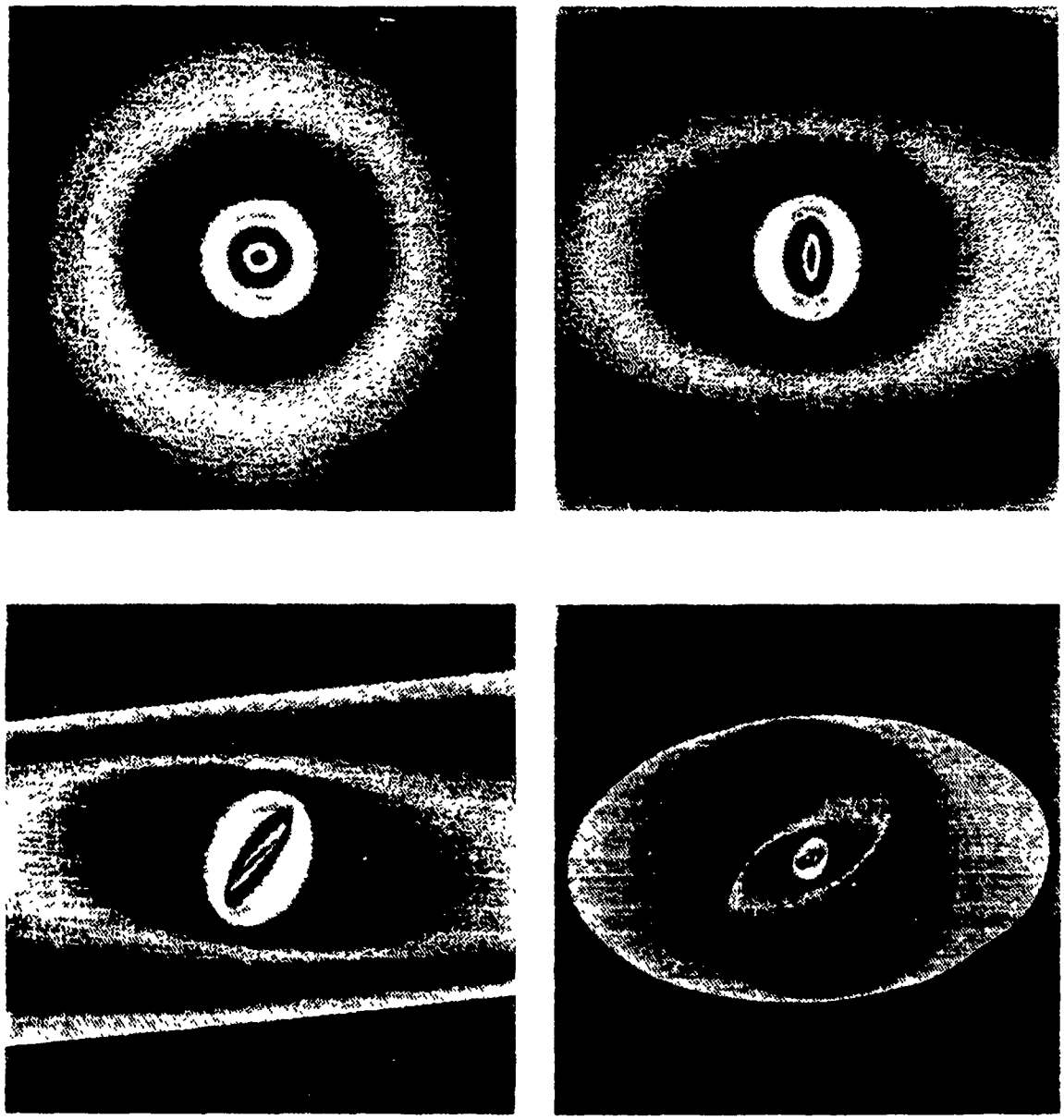

Figure 2.5 : Examples of theoretical ensemble average scaling spectral energy densities for the case of linear GSI with sphero-scale. The units of the sphero-scale are given relative to the external scale = 1 unit.
Top left: isotropic case: c=0.0, f=0.0, e=0.0, all balls are circular;
Top right: self-affine case: c=0.3, f=0.0, e=0.0 with sphero-scale at 0.14 units;
Bottom left: stratification dominant case ($a^2 > 0$) : c=0.6, f=0.5, e=0.6 with sphero-scale at 0.14 units;
Bottom right: rotation dominant case ($a^2 < 0$): c=0.8, f=0.4 e=2.0 with sphero-scale at 0.3 units;
d=1 for all cases. (See below for description of generator parameters (c, f, e) and $a^2 = c^2 + f^2 - e^2$). The amplitude of the fields are presented as ln$P$ with Palette 1 (see Appendix B). Palette 1 is discontinuous so that the contours of ln$P$ are highlighted.

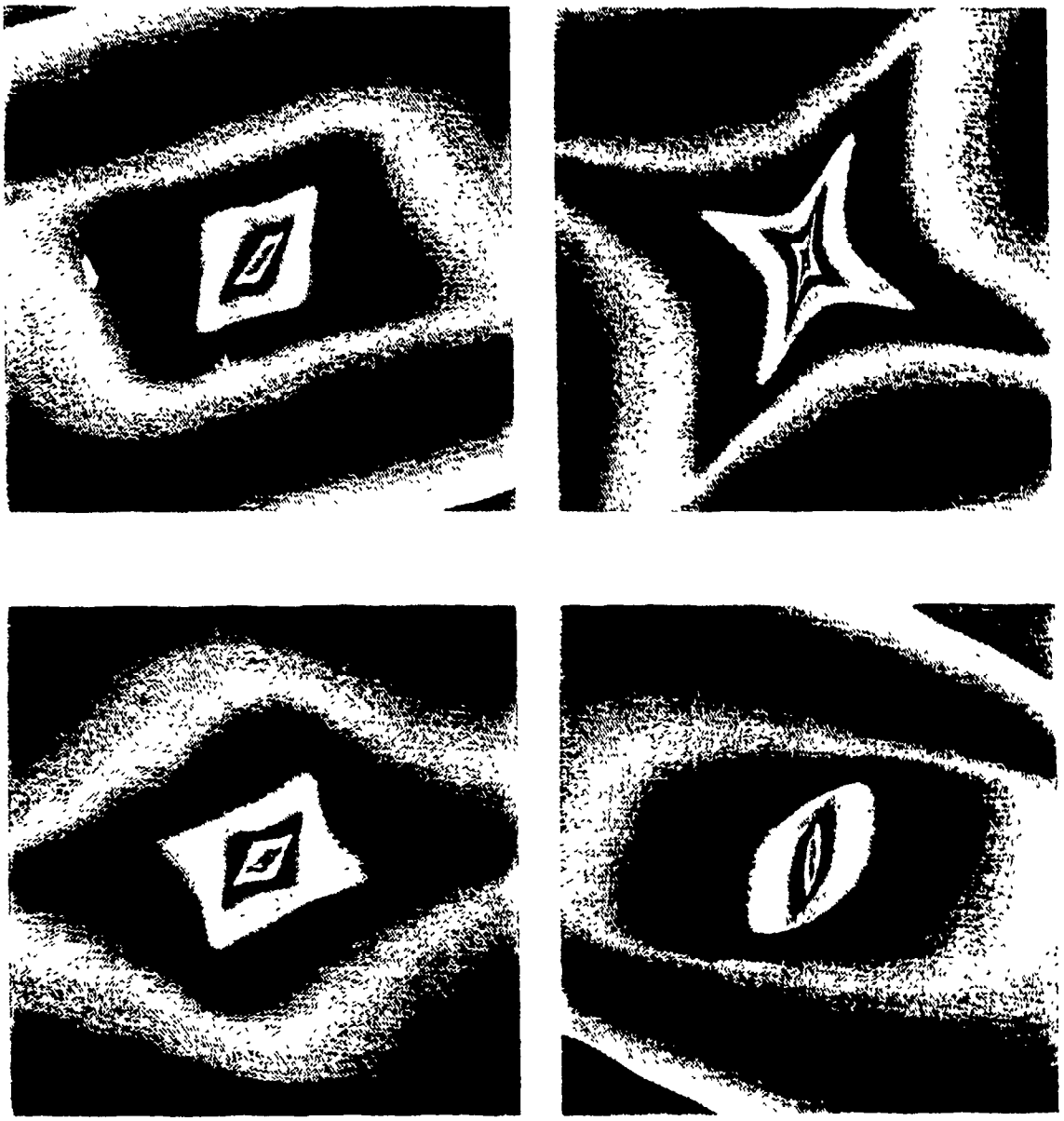

Figure 2.6 : Examples of theoretical ensemble average scaling spectral energy densities for linear GSI with balls described by fourth order equation (equation 2.3.7).
Top Left: c=0.45, f=0.2, e=0.4, $r_0 = 2.17 \cdot 10^3$, $a_1 = b_1 = a_2 = b_2 = 0.80\ 10^3$.
Top Right: c=0.3, f=0.1, e=0.0, $r_0 = 2.17\ 10^3$, $a_1 = b_1 = a_2 = 0.0$, $b_2 = 2.06\ 10^3$.
Bottom Left: c=0.35, f=0.2, e=0.5, $r_0 = 1.24\ 10^3$, $a_1 = 0.60\ 10^3$, $b_1 = 0.85\ 10^3$, $a_2 = -0.40\ 10^3$, $b_2 = 0.61\ 10^3$.
Bottom Right: c=0.3, f=-0.3, e=0.3, $r_0 = 2.17\ 10^3$, $a_1 = 0.56\ 10^3$, $b_1 = 1.48\ 10^3$, $a_2 = b_2 = 0.22\ 10^3$.
The ball parameters are in (units)$^{-4}$, where external scale = 1 unit. d=1 for all cases. (See below for description of generator parameters: c, f, e). The amplitude of the fields are presented as ln$P$ and labeled with the colours of Palette 1 (see Appendix B). Palette 1 is discontinuous so that the contours of ln$P$ are highlighted.

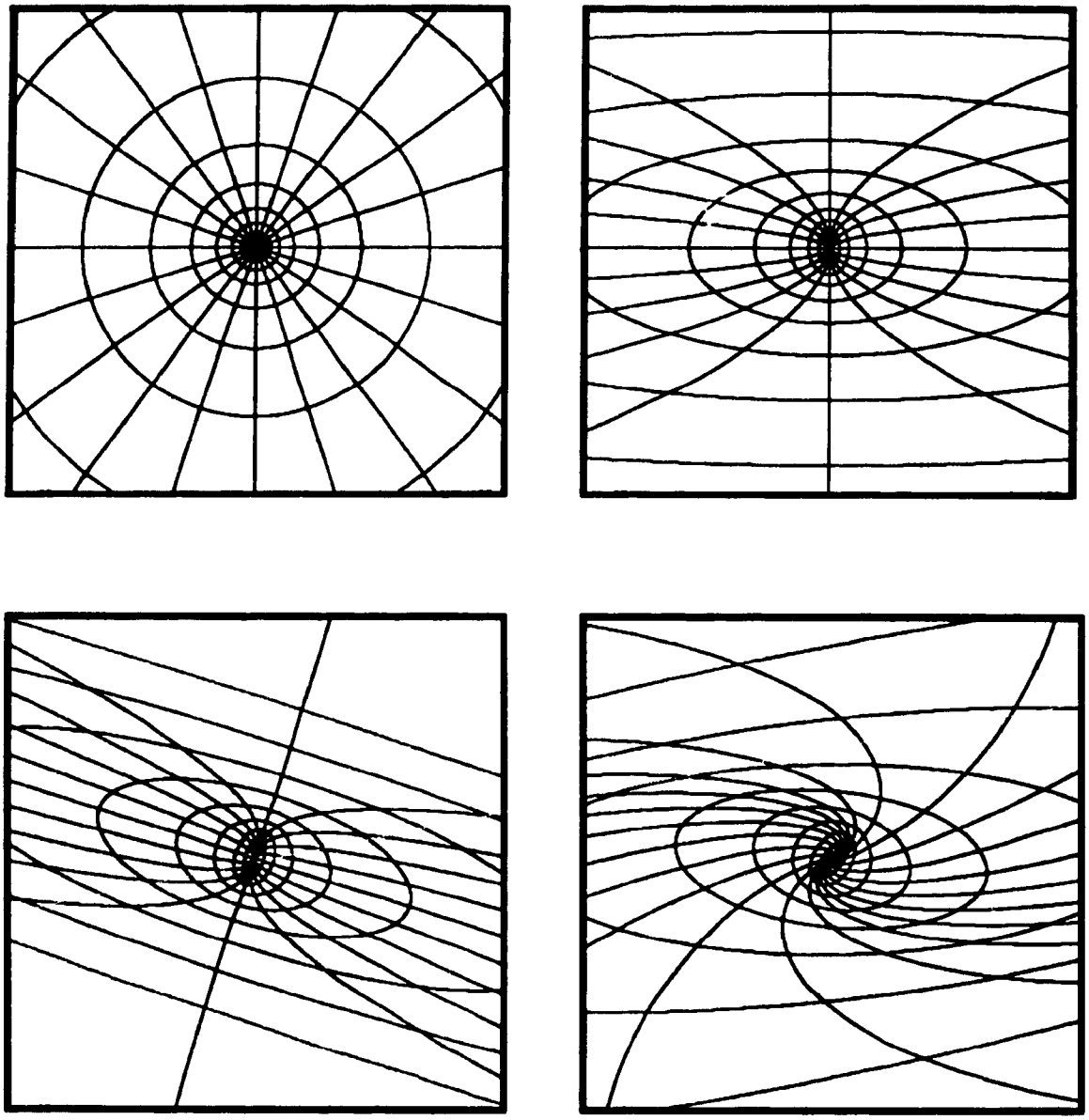

Figure 2.7 : Examples of balls and trajectories for linear GSI with sphero-scale: isotropic case: c=0.0, f=0.0, e=0.0 (top left); self-affine case: c=0.35, f=0.0, e=0.0 (top right); stratification dominant case ($a^2 > 0$) with no rotation: c=0.35, f=0.25, e=0.0 (bottom right); rotation dominant case ($a^2 < 0$): c=0.35, f=0.25 e=0.6. d=1 for all cases with sphero-scale at 0.06 units (where the external scale = 1 unit).

Writting this as a series, with $u \equiv \ln\lambda$:

$$T_\lambda = \lambda^d \sum_{n=0}^{\infty} \frac{(-u)^n (\mathbf{1}d - G)^n}{n!} \tag{2.3.11}$$

Defining $$a^2 \equiv c^2 + f^2 - e^2 \tag{2.3.12}$$

For the case when $a^2 > 0$:

$$(G - \mathbf{1}d)^{2n} = a^{2n}\mathbf{1} \quad \text{and} \quad (G - \mathbf{1}d)^{2n+1} = \frac{(G - \mathbf{1}d)a^{2n}}{a}$$

Then, separating into even and odd terms:

$$T_\lambda = \lambda^d \left(\mathbf{1}\cosh(au) + \frac{(G - \mathbf{1}d)\sinh(au)}{a} \right) \tag{2.3.13}$$

or

$$T_\lambda = \lambda^d \begin{pmatrix} \cosh(au) + \frac{c}{a}\sinh(au) & \frac{f+e}{a}\sinh(au) \\ \frac{f-e}{a}\sinh(au) & \cosh(au) - \frac{c}{a}\sinh(au) \end{pmatrix} \tag{2.3.14}$$

Similar calculations for $a^2 < 0$ yield the same result with the exception that the hyperbolic trigonometric functions are replaced by their regular counterparts and $a \Rightarrow |a|$. The case for a=0 yields:

$$T_\lambda = \lambda^d \begin{pmatrix} 1 + cu & (f+e)u \\ (f-e)u & 1 - cu \end{pmatrix} \tag{2.3.15}$$

Applying the different cases of the transformation yields two different morphologies that correspond to the sign of a^2: stratification dominant, corresponding to the case when $a^2 > 0$ and rotation dominant ($a^2 < 0$) (Schertzer and Lovejoy, 1985b). Stratification dominance is characterized by a limit to the rotation of the balls and no

limit to their stratification. In the case of linear GSI with a sphero-scale, (see figure 2.7), the ellipses become increasingly elongated while they have limited rotation. This can also be seen in the trajectories. In this case, only one sphero-scale exists. Note that there is a change in the major axes as you vary the scale through the sphero-scale. Rotation dominance is characterized by a limit to the stratification of the balls and no limit to rotation (see figure 2.7). The trajectories are spirals. In linear GSI with a sphero-scale, there are multiple sphero-scales. For further discussion see Pflug 1991a.

To complete the linear GSI system, the definition of scale must be completed. In the previous section it was argued that φ can be taken as some power of the volume bounded by the associated contour. The power was chosen to be $1/D_{el}$ where D_{el} is the elliptical dimension. In the horizontal plane of the atmosphere, we do not expect the elliptical dimension to be different than the topological dimension since there is no mechanism that causes differential stratification. Therefore, $D_{el}=2$ and thus φ is the square root of the area of the balls. Since,

$$D_{el} = \text{Trace}(G) = 2d, \tag{2.3.16}$$

we have

$$d = 1 \tag{2.3.17}$$

2.4 Restrictions on the Generator and Balls of a Generalized Scale Invariant System

Every vector of the field must be associated to one, and only one, scale and one, and only one, trajectory. The curves that describe the balls cannot cross, nor can the trajectories. This restriction is necessary to ensure that no vector is associated to more than one scale (i.e. the vector must have only one size). Since the balls necessarily cross if the trajectories cross and the converse is not true, it is a more stringent restriction that the balls do not cross. The above restrictions correspond to restrictions on the generator and ball parameters.

The condition that the real parts of the (generalized) eigenspectrum of the generator, G, must be positive (Schertzer and Lovejoy, 1985b) ensures that the trajectories are unique and increasing. If this condition is not satisfied, a trajectory in the

direction of a negative eigenvalue would move inwards with increasing scale (as opposed to outwards as it must). This can be seen because a vector in the direction of an eigenvector will be transformed to another vector in the same direction multiplied by the scale ratio raised to the power of the corresponding eigenvalue (by the properties of eigenvalues). Therefore, if the eigenvalue has a negative real part, the vector will be reduced (if $\lambda > 1$). The eigenvalues of T_λ will be λ^{e_i} where e_i are the eigenvalues of G.

The above condition is sufficient to ensure that there is some ball that can be drawn such that each vector of the ball is associated with a unique trajectory. However, a priori, it is impossible to determine what equation can describe this ball. Therefore, it is necessary to make some approximation to the balls so that they may be described by a predetermined form. For linear GSI, we chose the second and fourth order bivariate polynomials, equations (2.3.1) and (2.3.2) respectively, since these forms are invariant under linear transformations (see section 2.3). This is a necessity if the constraints on G and the balls are to be found.

The condition of non-intersection of the balls, B_1 and $B_2 = T_\lambda B_1$, implies that B_1 must be completely enclosed within B_2 for all $\lambda > 1$ (magnifications). That is,

$$r_2 - r_1 > 0 \qquad (2.4.1)$$

where r_i is the curve in polar form that describes the ball, B_i. This condition must hold for all θ and also for all the balls related by T_λ. However, if the condition is violated at one scale, it is necessarily violated at all scales. This can be seen by noting that if a vector, $\mathbf{x}_a$, is associated wih two scales, λ_1 and λ_2, then all vectors on the trajectory $\mathbf{x}_b = T_\lambda \mathbf{x}_a$ (see sections 2.1 and 2.2) are also associated with two scales, $\lambda\lambda_1$ and $\lambda\lambda_2$. Therefore, it is sufficient to compare any ball with its infinitesimal neighbour. Thus, restrictions can be placed on the ball, B_1, and the generator to ensure that the GSI system which they describe is valid. These restrictions are found below for the case of linear GSI when the balls are described by the second order equation (2.3.5). The restrictions for the fourth order case (2.3.7) can be found with an identical procedure and they are stated below.

The ball, B_1, will be described by:

$$r_1 = \left[r_{0_1} + a_{1_1}\cos 2\theta + b_{1_1}\sin 2\theta\right]^{-\frac{1}{2}} \tag{2.4.2}$$

and its infinitesimal neighbour,

$$r_2 = \left[r_{0_2} + a_{1_2}\cos 2\theta + b_{1_2}\sin 2\theta\right]^{-\frac{1}{2}} \tag{2.4.3}$$

can be found by operating the infinitesimal scale changing operator, T_{du}, (where $u = \ln\lambda$ and $du = d\lambda/\lambda$) on every vector in r_1. More practically, since the form of the equation is invariant under linear transformations, the parameters of r_2 can be found as functions of the parameters of r_1 and G by finding the transformation that T_{du} (operating on the vectors) will 'induce' on r_1 (see Elliott and Dawber, 1979). To facilitate this, r_1 will be written in matrix form:

$$A_1x^2 + 2B_1xy + C_1y^2 = 1 \quad \Rightarrow \quad \mathbf{x}^T\mathbf{M}_1\mathbf{x} = 1 \tag{2.4.4}$$

where

$$\mathbf{x} = \begin{pmatrix} x \\ y \end{pmatrix} \text{ and } \mathbf{M}_1 = \begin{pmatrix} A_1 & B_1 \\ B_1 & C_1 \end{pmatrix} \tag{2.4.5}$$

and the transformation between the parameters of $\mathbf{M}_1$ and r_1 are as equation (2.3.6):

$$r_0 = \frac{1}{2}(A + C)\,, \quad a_1 = \frac{1}{2}(A - C) \text{ and } b_1 = B \tag{2.4.6}$$

Then, T_{du} will induce a transformation on $\mathbf{M}_1$ as follows:

$$\mathbf{x}^T\left(\mathbf{T}_{du}^{-1}\right)^T\mathbf{M}_1\left(\mathbf{T}_{du}^{-1}\right)\mathbf{x} = 1 \tag{2.4.7}$$

$$\Rightarrow \quad \mathbf{x}^T\mathbf{M}_2\mathbf{x} = 1 \tag{2.4.8}$$

$$\text{where} \quad \mathbf{M}_2 = \left(\mathbf{T}_{du}^{-1}\right)^T\mathbf{M}_1\left(\mathbf{T}_{du}^{-1}\right)$$

and $\mathbf{M}_2$ will be related to r_2 by the simple transformations of equation (2.4.6).

Before continuing, the infinitesimal scale changing operator, T_{du}, must be found. This can be done by expanding the Fourier space scale changing operator, $T_\lambda = \lambda^G$, in a Taylor series to first order about $u = \ln\lambda = 0$.

$$\mathbf{T}_\lambda = \exp(Gu) \tag{2.4.9}$$

$$\mathbf{T}_{du} = 1 + \left.\frac{dT_\lambda}{du}\right|_{u=0} du = 1 + G\,du \tag{2.4.10}$$

and

$$T_{du}^{-1} = 1 - G\,du \tag{2.4.11}$$

where the inverse operator was found from $T_\lambda^{-1} = T_{\lambda^{-1}}$ i.e. by replacing $u \Rightarrow -u$.

Now, $\mathbf{M}_2$ can be found using the inverse infinitesimal operator of equation (2.4.11):

$$\begin{aligned}\mathbf{M}_2 &= \left(\mathbf{T}_\lambda^{-1}\right)^T \mathbf{M}_1 \left(\mathbf{T}_\lambda^{-1}\right) \\ &= (1 - G\,du)^T \mathbf{M}_1 (1 - G\,du) \\ &= (1 - G^T du)(\mathbf{M}_1 - \mathbf{M}_1 G\,du) \\ &= \mathbf{M}_1 - \mathbf{M}_1 G\,du - G^T \mathbf{M}_1\,du + G^T \mathbf{M}_1 G(du)^2\end{aligned}$$

neglecting the term of order $(du)^2$

$$\mathbf{M}_2 = \mathbf{M}_1 - (\mathbf{M}_1 G + G^T \mathbf{M}_1)\,du \tag{2.4.12}$$

$$\mathbf{M}_2 = \mathbf{M}_1 - \frac{d\mathbf{M}}{du}\,du \tag{2.4.13}$$

where $\dfrac{d\mathbf{M}}{du} = \mathbf{M}_1 G + G^T \mathbf{M}_1$. Finding $\dfrac{d\mathbf{M}}{du}$ explicitly:

$$\frac{d\mathbf{M}}{du} = \begin{pmatrix} A_1 & B_1 \\ B_1 & C_1 \end{pmatrix}\begin{pmatrix} g_{11} & g_{12} \\ g_{21} & g_{22} \end{pmatrix} + \begin{pmatrix} g_{11} & g_{21} \\ g_{12} & g_{22} \end{pmatrix}\begin{pmatrix} A_1 & B_1 \\ B_1 & C_1 \end{pmatrix} \tag{2.4.14}$$

where

$$G = \begin{pmatrix} g_{11} & g_{12} \\ g_{21} & g_{22} \end{pmatrix} = \begin{pmatrix} d+c & f+e \\ f-e & d-c \end{pmatrix} \tag{2.4.15}$$

$$\frac{\mathrm{dM}}{\mathrm{d}u}=\begin{pmatrix}\frac{\mathrm{d}A}{\mathrm{d}u} & \frac{\mathrm{d}B}{\mathrm{d}u}\\ \frac{\mathrm{d}B}{\mathrm{d}u} & \frac{\mathrm{d}C}{\mathrm{d}u}\end{pmatrix}=\begin{pmatrix}2g_{11}A_1+2g_{21}B_1 & g_{12}A_1+(g_{11}+g_{22})B_1+g_{21}C_1\\ g_{12}A_1+(g_{11}+g_{22})B_1+g_{21}C_1 & 2g_{12}B_1+2g_{22}C_1\end{pmatrix} \tag{2.4.16}$$

Therefore, since $A_2=A_1-\frac{\mathrm{d}A}{\mathrm{d}u}\mathrm{d}u$, from equation (2.4.13), and similarly for B_2 and C_2, we can write:

$$r_{0_2}=\frac{1}{2}(A_2+C_2)=\frac{1}{2}(A_1+C_1)-\frac{1}{2}\left(\frac{\mathrm{d}A}{\mathrm{d}u}+\frac{\mathrm{d}C}{\mathrm{d}u}\right)\mathrm{d}u \tag{2.4.17}$$

Then,

$$r_{0_2}=r_{0_1}-\frac{\mathrm{d}r_0}{\mathrm{d}u}\mathrm{d}u \tag{2.4.18}$$

where $$\frac{\mathrm{d}r_0}{\mathrm{d}u}=\frac{1}{2}\left(\frac{\mathrm{d}A}{\mathrm{d}u}+\frac{\mathrm{d}C}{\mathrm{d}u}\right)=(d+c)A_1+2fB_1+(d-c)C_1 \tag{2.4.19}$$

or $$\frac{\mathrm{d}r_0}{\mathrm{d}u}=2\left(r_{0_1}d+a_{1_1}c+b_{1_1}f\right) \tag{2.4.20}$$

from equations (2.4.6), (2.4.15), (2.4.16) and (2.4.17). There are similar calculations for a_{1_2} and b_{1_2}. In summary:

$$\begin{aligned} r_{0_2}&=r_{0_1}-\frac{\mathrm{d}r_0}{\mathrm{d}u}\mathrm{d}u\\ a_{1_2}&=a_{1_1}-\frac{\mathrm{d}a_1}{\mathrm{d}u}\mathrm{d}u\\ b_{1_2}&=b_{1_1}-\frac{\mathrm{d}b_1}{\mathrm{d}u}\mathrm{d}u \end{aligned} \tag{2.4.21}$$

where $$\begin{aligned} \frac{\mathrm{d}r_0}{\mathrm{d}u}&=2\left(r_{0_1}d+a_{1_1}c+b_{1_1}f\right)\\ \frac{\mathrm{d}a_1}{\mathrm{d}u}&=2\left(r_{0_1}c+a_{1_1}d-b_{1_1}e\right)\\ \frac{\mathrm{d}b_1}{\mathrm{d}u}&=2\left(r_{0_1}f+a_{1_1}e+b_{1_1}d\right) \end{aligned} \tag{2.4.22}$$

We now return to the restriction: $r_2 - r_1 > 0$ or equivalently $r_2^2 - r_1^2 > 0$. Investigating further, using equations (2.4.2) and (2.4.3):

$$\frac{1}{r_{0_2} + a_{1_2}\cos 2\theta + b_{1_2}\sin 2\theta} - \frac{1}{r_{0_1} + a_{1_1}\cos 2\theta + b_{1_1}\sin 2\theta} > 0$$

$$\left(r_{0_1} + a_{1_1}\cos 2\theta + b_{1_1}\sin 2\theta\right) - \left(r_{0_2} + a_{1_2}\cos 2\theta + b_{1_2}\sin 2\theta\right) > 0$$

$$\left(r_{0_1} - r_{0_2}\right) + \left(a_{1_1} - a_{1_2}\right)\cos 2\theta + \left(b_{1_1} - b_{1_2}\right)\sin 2\theta > 0 \qquad (2.4.23)$$

Using equation (2.4.21) and dividing through by du:

$$\frac{dr_0}{du} + \frac{da_1}{du}\cos 2\theta + \frac{db_1}{du}\sin 2\theta > 0 \qquad (2.4.24)$$

where $\frac{dr_0}{du}$, $\frac{da_1}{du}$ and $\frac{db_1}{du}$ are as in equation (2.4.22).

This equation can be simplified further by noting that it must hold for all θ and therefore, it is adequate to impose the condition on the minimum of the equation:

$$\frac{d}{d\theta}\left[\frac{dr_0}{du} + \frac{da_1}{du}\cos 2\theta + \frac{db_1}{du}\sin 2\theta\right] = 2\frac{da_1}{du}\sin 2\theta - 2\frac{db_1}{du}\cos 2\theta = 0 \qquad (2.2.25)$$

$$\tan 2\theta = \frac{db_1}{da_1} \quad \Rightarrow \quad \theta = \frac{1}{2}\tan^{-1}\left(\frac{db_1}{da_1}\right) + \phi \qquad (2.4.26)$$

where $da_1 = \frac{da_1}{du}du$, $db_1 = \frac{db_1}{du}du$, $\phi = 0$ or π corresponding to a maximum or a minimum and depending on the four different cases (the four possible combinations of signs of da_1 and db_1). However, in all cases (with the correct choice of ϕ), by substituting equation (2.4.26) into equation (2.4.24) and using basic trigonometric identities, the inequality becomes:

$$\frac{dr_0}{du} - \frac{\left(\frac{da_1}{du}\right)^2}{\sqrt{\left(\frac{da_1}{du}\right)^2 + \left(\frac{db_1}{du}\right)^2}} - \frac{\left(\frac{db_1}{du}\right)^2}{\sqrt{\left(\frac{da_1}{du}\right)^2 + \left(\frac{db_1}{du}\right)^2}} > 0 \qquad (2.4.27)$$

$$\frac{dr_0}{du} > \sqrt{\left(\frac{da_1}{du}\right)^2 + \left(\frac{db_1}{du}\right)^2} \qquad (2.4.28)$$

while noting the condition $\frac{dr_0}{du} > 0$, the restriction on the generator and ball parameters can be written:

$$\left(\frac{dr_0}{du}\right)^2 > \left(\frac{da_1}{du}\right)^2 + \left(\frac{db_1}{du}\right)^2 \qquad (2.4.29)$$

Using equation (2.4.22) and noting that this restriction must hold when r_1 describes any member of the family of balls, and thus the subscripts of the coefficients of r_1 can be dropped, the general condition becomes:

$$(r_0 d + a_1 c + b_1 f)^2 > (r_0 c + a_1 d - b_1 e)^2 + (r_0 f + a_1 e + b_1 d)^2 \qquad (2.4.30)$$

The above restriction can be simplified if the initial contour is of a less general form. For example, in the case where a sphero-scale exists (see section 2.3), there will be a ball that is spherical ($a_1 = b_1 = 0$). Therefore, the restriction for the case of linear GSI with a sphero-scale is that the GSI parameters must satisfy the simple inequality:

$$d^2 > c^2 + f^2 \qquad (2.4.31)$$

When there is no assumption of the existence of a sphero-scale, it is more difficult to obtain such a general form that does not depend on the ball parameters. However, it is possible to prove the inequalities,

$$d^2 > c^2 \quad \text{and} \quad d^2 > f^2 \qquad (2.4.32)$$

for the cases where $a_1 = 0$ and $b_1 = 0$ respectively.

In the fourth order case, the condition remains $r_2 - r_1 > 0$ (for $du > 0$) or equivalently, $r_2^4 - r_1^4 > 0$, where the fourth order equation is written as in equation (2.3.7):

$$r = [r_0 + a_1 \cos 2\theta + b_1 \sin 2\theta + a_2 \cos 4\theta + b_2 \sin 4\theta]^{-1/4} \qquad (2.4.33)$$

Following the same procedure, the restriction can be found:

$$\frac{dr_0}{du} + \frac{da_1}{du}\cos 2\theta + \frac{db_1}{du}\sin 2\theta + \frac{da_2}{du}\cos 4\theta + \frac{db_2}{du}\sin 4\theta > 0 \qquad (2.4.34)$$

where:
$$\frac{dr_0}{du} = 4r_0 d + \frac{1}{3}a_1 c + \frac{1}{3}b_1 f$$
$$\frac{da_1}{du} = 4\left(r_0 c + a_1 d - \frac{1}{2}b_1 e + a_2 c + b_2 f\right)$$
$$\frac{db_1}{du} = 4\left(r0_1 f + \frac{1}{2}a_1 e + b_1 d - a_2 f + b_2 c\right)$$
$$\frac{da_2}{du} = a_1 c - b_1 f + 4a_2 d - 4b_2 e$$
$$\frac{db_2}{du} = a_1 f + b_1 c - 4a_2 e + 4b_2 d$$

This condition must hold for all angles. No analytic solution was found for the minimum of equation (2.4.34) as a function of θ, therefore no simplification along the lines of the second order case was possible. Although this form is not ideal, it is possible to tell if a given set of generator and ball parameters is a valid GSI system. This can be done by simply plotting equation (2.4.34) numerically as a function of θ. If the value is positive for all θ, the GSI parameters described a valid system. This method must be used, for example, if valid simulations are to be generated.

The results of this section will also be used to restrict the search of the parameter space that is necessary in GSI analysis techniques (see chapter 3, in particular 3.3.2d)

Chapter 3

ANALYSIS TECHNIQUES FOR LINEAR GENERALIZED SCALE INVARIANCE

3.1 Method of Least-Squares for Linear Generalized Scale Invariance

The purpose of the analysis techniques discussed below is to test the hypothesis of Generalized Scale Invariance by determining the parameters of the scale invariant generator and the balls that best describe a scaling field. The problem is complicated by the fact that the scaling is not expected to hold on a single realization, but only when averaged over an ensemble of realizations with the same generator and family of balls. In such an ensemble average, the field will satisfy:

$$\langle P_\lambda \rangle = \lambda^{-s} \langle P_1 \rangle \tag{3.1.1}$$

or

$$\ln\langle P_\lambda \rangle = -s \ln \lambda + \ln\langle P_1 \rangle \tag{3.1.2}$$

exactly, for every contour and every vector of the contour, where $\langle\ \rangle$ indicates an ensemble average quantity, $\langle P_1 \rangle$ is the amplitude of the spectral energy density about a unit ball, B_1, λ is the scale ratio with respect to the unit ball and s is the anisotropic scaling exponent. The generator parameters themselves are possibly stochastic (i.e. they will vary randomly from scene to scene). An attempt to empirically estimate the ensemble average by averaging many arbitrary realizations would result in a smearing of the parameters (since each realization would have a different generator). Therefore, only one realization will be analyzed at a time and fluctuations about the ensemble average contours of the spectral energy density are expected. (Figure 3.1 shows the spectral energy density of a simulated single realization and its ensemble average counterpart.)

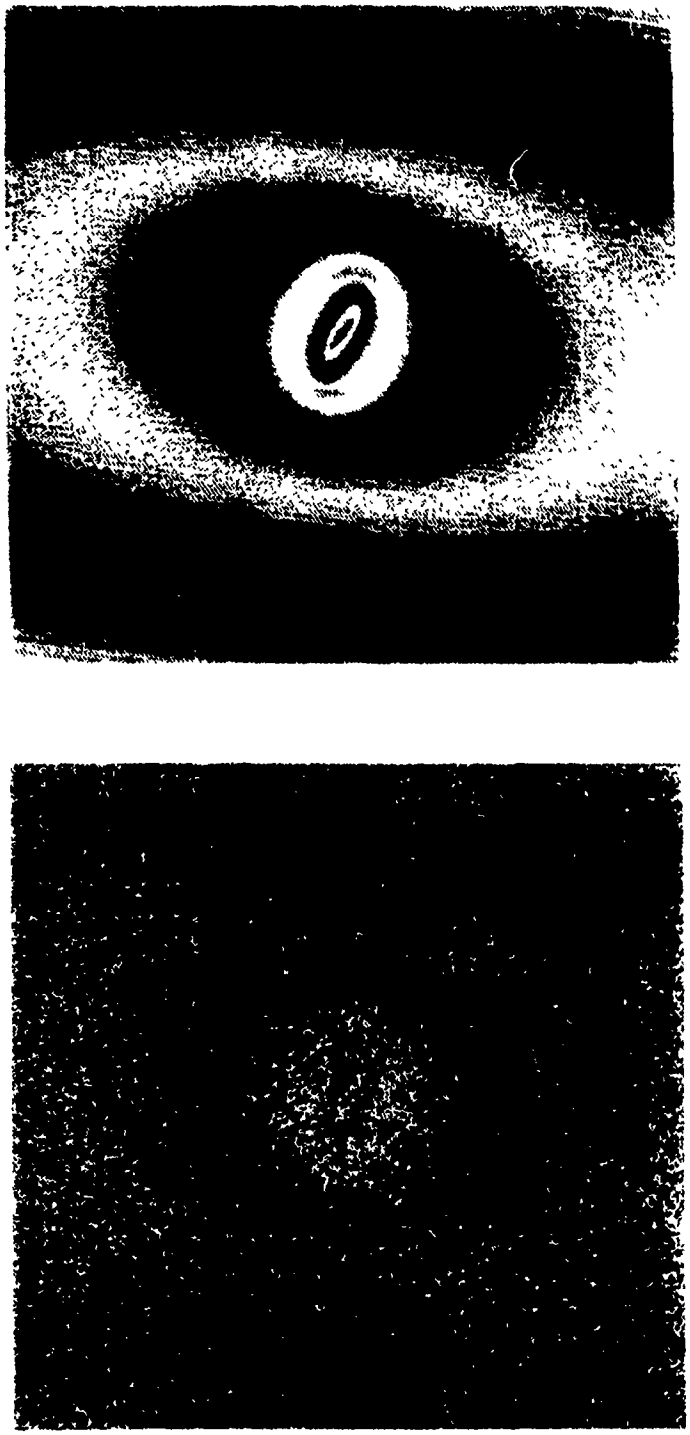

Figure 3.1 : Theoretical ensemble average spectral energy density (top), and a corresponding single realization (bottom) (from a multifractal simulation). An average over an ensemble of such single realizations would produce an image as above (top). Images have linear GSI parameters: s=2.68, G: c=0.3, f=0.2 and e=0.3 and B_1: sphero-scale at 0.14 units (where external scale = 1 unit). Intensities are presented as ln$P$ and labeled by the colours of the discontinuous Palette 1 of Appendix B.

The problem of the estimation of the GSI parameters can be considered as one of a non-linear statistical regression. That is, the N data points, $P(\mathbf{k}_i)$, of the spectral energy density of a single realization are fit to a theoretical function, $P_t(\mathbf{k}) = \langle P(G, B_1, \langle P_1 \rangle, s, \mathbf{k}) \rangle$, which is the ensemble average spectral energy density generated from the linear GSI parameters: $G(c, f, e)$ (since by convention $d = 1$), $B_1 = B_1(r_0, a_1, b_1, [a_2, b_2])$, s, and $\langle P_1 \rangle$, where a unit ball, B_1, is estimated by the second [fourth] order equation (2.3.5) [(2.3.7)]. Usual procedures involve the method of least-squares, where the parameter estimates can be determined by minimizing the 'error function':

$$E^2(G, B_1, \langle P_1 \rangle, s) = \frac{1}{N} \sum_{i=1}^{N} \left[\ln P(\mathbf{k}_i) - \ln P_t(\mathbf{k}_i, G, B_1, \langle P_1 \rangle, s) \right]^2 \qquad (3.1.3)$$

Other E^2 may be defined for the same purpose, but we choose to use the difference of logarithms (see section 3.3.1 for reasons and implications). Note that, from equation (3.1.2), $\ln P_t(\mathbf{k}_i) = -s \ln \lambda(G, B_1, \mathbf{k}_i) + \ln \langle P_1 \rangle$, where the function $\lambda(G, B_1, \mathbf{k}_i)$ is the solution of a non-trivial transendental equation (involving G and B_1) which must be solved for each $\mathbf{k}_i$.

Since it is not possible to analytically solve for the minimum of E^2, it is necessary to consider E^2 as a continuous function of the p parameters that describes a p-dimensional hypersurface in parameter space (where p is, at least, eight, depending on B_1, as above). Therefore, the space must be searched for the appropriate minimum (Bevington, 1969, Chapter 11) i.e. E^2 must be found numerically at intervals in parameter space to trace out the behavior of the hypersurface. In general, E^2 can be a complex function with multiple extrema. Therefore, if the absolute minimum is to be found, the intervals must be fine enough such that the estimate of the hypersurface exhibits the same extrema. Since the analysis is performed on a single realization, the actual explicit values of E^2 will be statistically scattered around the continuous hypersurface expected when an infinity of independent data points are used (this would require knowledge of P over an infinite range of scales). This continuous hypersurface, which will be denoted by E^2_{-}, will have similar characteristics as the hypersurface expected when $P(\mathbf{k}_i)$ are ensemble average quantities. The hypersurface of the ensemble average will be denoted as $E^2_{\langle\rangle}$ and the usual E^2 will be reserved for the hypersurface of a single realization. Figure 3.2 shows a one-dimensional cross-section of a possible

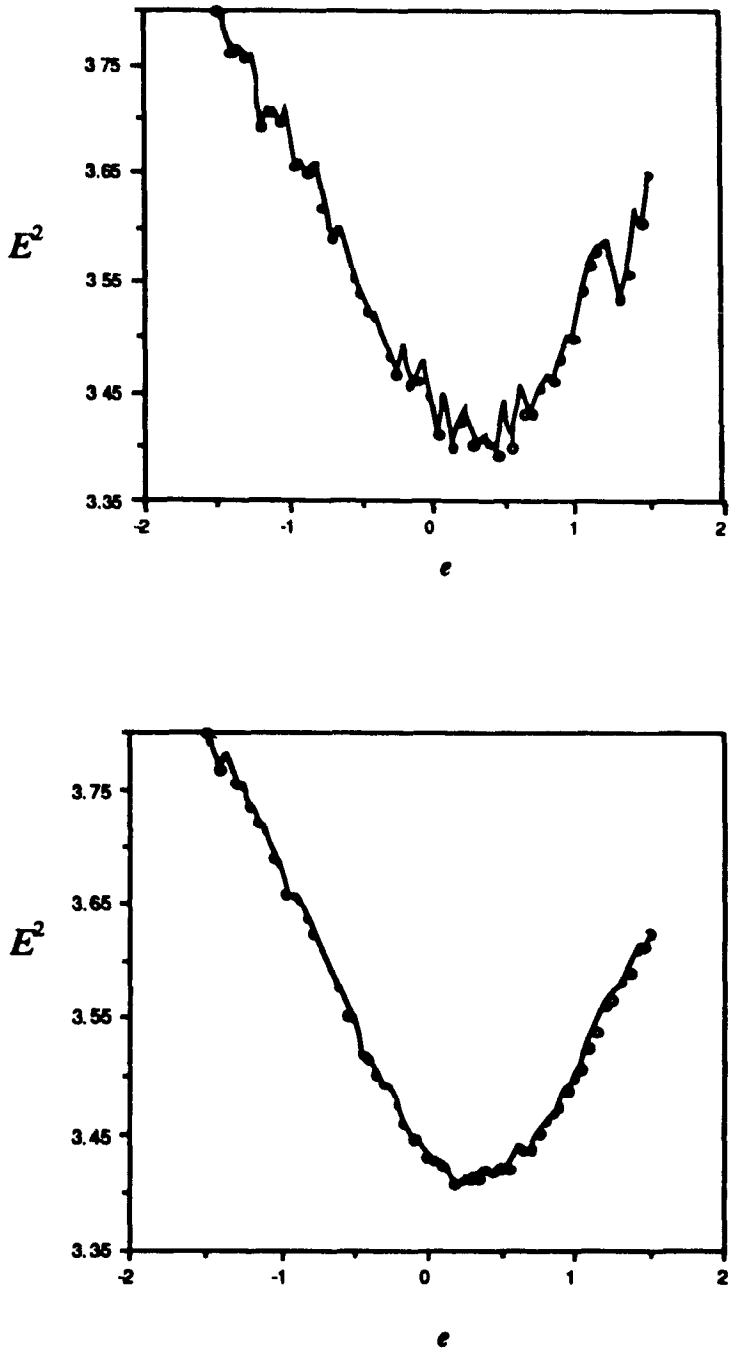

Figure 3.2 : The effect of an increase in the number of points used to calculate E^2. Shown are the one-dimensional cross sections (c and f fixed) for the hypersurfaces of a multifractal simulation (see figure 3.1, bottom) calculated using ~15 000 points (top) and ~450 000 points (bottom). As the number of statistically independent points goes to infinity, the hypersurface is expected to become smooth. The explicit values of E^2 have been connected by a continuous line to highlight the point to point fluctuations.

hypersurface for a single realization calculated using two different numbers of data points. It can be seen that the hypersurface becomes smoother as the number of points increases. Due to these high frequency fluctuations, a function is fit to the explicit values of E^2 in an attempt to estimate E^2_{∞}. The estimated minimum of E^2 can then be found by calculating the minimum of the function.

The full search required for (at least) an eight-dimensional parameter space is computationally prohibitive, even when a transcendental equation need not be solved. Therefore, it is necessary to make some approximation to the error function of equation (3.1.3). In this chapter, two such approximations will be discussed: The Monte Carlo Differential Rotation method of Pflug (1991a) and the Scale Invariant Generator technique (presented here for the first time).

3.2 Monte Carlo Differential Rotation Method

The Monte Carlo Differential Rotation method started with explicit guesses for the parameters and used a Monte Carlo approximation to the error function of equation (3.1.3). Instead of solving for $\ln P_i(\mathbf{k}_i)$ using the transcendental equation, an estimated value was calculated from $-s\ln\lambda_i + \ln\langle P_1\rangle$, where λ_i is a randomly chosen scale ratio. Then the position of the corresponding data point was computed from: $\mathbf{k}_i = \lambda_i^G \mathbf{k}_{1_i}$, where $\mathbf{k}_{1_i}$ is a randomly chosen vector on the unit ball. Thus, prior knowledge of s, $\langle P_1\rangle$ and the parameters of B_1 was required, therefore, they were estimated prior to the estimation of G. Unless the anisotropy is quite extreme, s can be reasonably estimated from the isotropic energy spectral slope, β (see section 1.2), since the anisotropy tends to be 'washed out' by angular integration in Fourier space. B_1 was estimated by fitting a curve to the levelset of the field at $\langle P_1\rangle$ (the set of data points that have amplitude within the range $\langle P_1\rangle \pm \Delta P$) (see figure 3.3). Since, within the scaling regime, any ball is equivalent to any other ball, P_1 can be chosen arbitrarily. The curve describing B_1 was of the form:

$$|\mathbf{k}_1| = k_1(\theta) = q_0 + q_1\cos(2\theta) + q_2\sin(2\theta) + q_3\cos(4\theta) + q_4\sin(4\theta) \quad (3.2.1)$$

where q_j are real numbers.[1]

[1] This curve describing B_1 is different then the one used in the Scale Invariant Generator technique (see section 3.3). This curve is not invariant under linear transformations (see section 2.3).

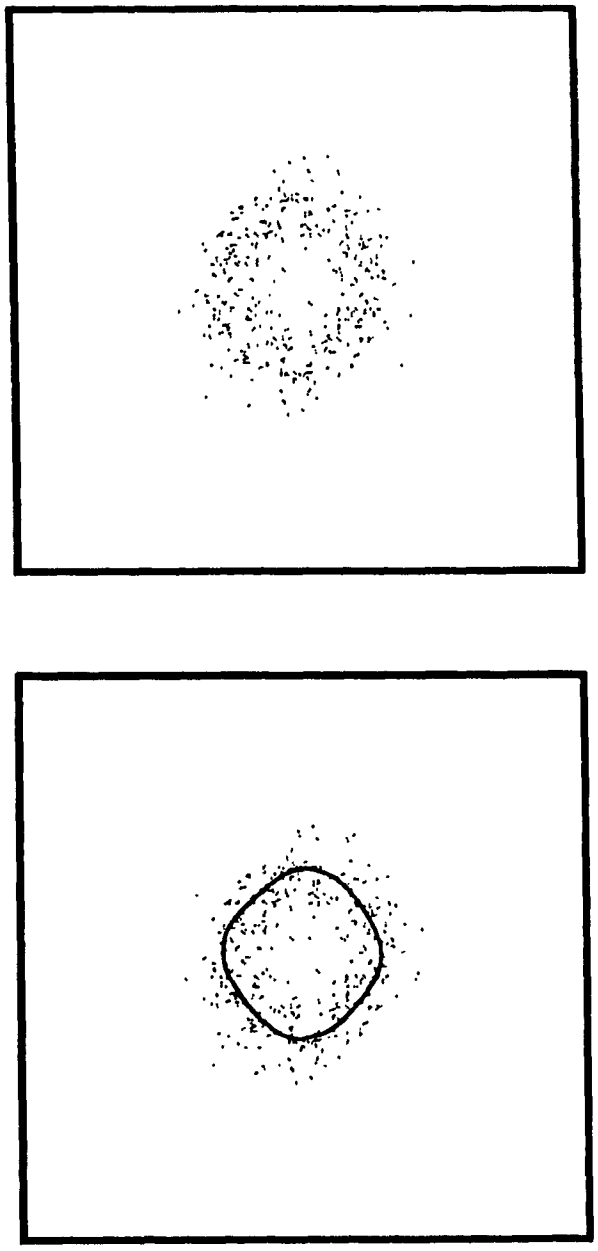

Figure 3.3 : A levelset of a spectral energy density of a satellite cloud radiance (top) and the same levelset with curve drawn (bottom). This curve (of the form of equation 3.2.1) is the estimated unit ball, B_1.

An error function[2], that was only a function of three parameters, $G = G(c, f, e)$, was defined :

$$E^2_{MCDR}(G) = \frac{1}{n}\sum_i \left[\ln P\left(\lambda_i^{-G}\mathbf{k}_{1_i}\right) + s\ln\lambda_i - \ln\langle P_1\rangle\right]^2 \qquad (3.2.2)$$

The sum is over n random combinations of $\mathbf{k}_{1_i}$ and λ_i, and therefore n data points, $P_i = P\left(\lambda_i^{-G}\mathbf{k}_{1_i}\right)$.

The random $\mathbf{k}_{1_i}$ were found by choosing a point on B_1 from a randomly chosen angle, θ_i, between 0 and 2π. Then $\mathbf{k}_{1_i}$ was computed from $k_1(\theta_i)$, equation (3.2.1). λ_i was a random number between 0 and λ_{max} (λ_{max} was an estimation of the maximum scale ratio). n was chosen such that the fluctuations due to adding another data point were much smaller than the gradient of the hypersurface.

The estimates for c, f and e were found using a 'grid search' (Bevington, 1969) of the parameter space: explicit guesses were made for two of the parameters then E^2_{MCDR} (equation 3.2.2) was found as a function of the third, while the other two were held fixed at their guessed values, (i.e. a one-dimensional cross section of the hypersurface was investigated). A one-dimensional parabola was fit, near the minimum, to smooth the high frequency fluctuations. The first estimate of the third parameter was the value for which the parabola was a minimum. With the third parameter held fixed at its first estimate value, the other two were varied successively. The successive variation of all three parameters was then iterated until convergence was reached.

3.3 The Scale Invariant Generator Technique

In order for a GSI analysis technique to be numerically efficient, it must necessarily reduce the dimension of the parameter space. The Monte Carlo Differential Rotation method attempted to do this by estimating many of the parameters before searching the parameter space of $G(c, f, e)$. However, this is not an ideal solution since

---

[2] Pflug studied the error functions defined using the difference of logarithms of P as well as that of the difference of P and the results were found to be similar.

errors in the estimations (of B_1 in particular) were magnified increasingly with scale ratio when the $\mathbf{k}_i$ were calculated. The errors were due to the statistical scatter of the levelsets from which the B_1 were estimated. In some cases, it may have been possible to completely miscalculate the unit ball since a levelset of P may not resemble the family of curves that describes it. The reason is because the position of the data points of a given value of P can be considered to statistically fluctuate about the ensemble average contour. The fluctuations are predominantly uniformly spread between the theoretical contours $\langle P \rangle \pm \Delta P$, where ΔP depends on the magnitude of the fluctuations. Therefore, since the contours can be closer together at some angles, the spread of points in space at those angles will be smaller. Fitting a curve to a levelset of such a case will cause biased, hence poor, parameter estimates.

The Scale Invariant Generator technique, described in this thesis, has the very significant advantage of avoiding the problems of making initial estimations to reduce the parameter space (e.g. of B_1, as above) by separating the estimations of G and B_1. The Scale Invariant Generator technique estimates the more fundamental G without prior knowledge of B_1. It then uses G to 'enhance' the spectral energy density and thus enable an accurate estimate of B_1. The discussion of the technique will therefore start with the estimation of G.

3.3.1 Estimation of the Generator, G

(a) Determination of the error function

G can be estimated by searching a three-dimensional parameter space without introducing errors due to the prior estimation of other parameters (with the exception of s, which can usually be accurately estimated using β, as before). The Scale Invariant Generator (SIG) technique can do this by moving away from the idea of comparing the value of a data point to a theoretical ensemble average value of P and by exploiting the fact that the amplitude of any two points on the same trajectory, $\mathbf{k}_{\lambda_1}$ and $\mathbf{k}_{\lambda_2} = \lambda_2^G \mathbf{k}_{\lambda_1}$, (see sections 2.1 and 2.3) will *on average* be related by:

$$\left\langle P\left(\lambda_2^G \mathbf{k}_{\lambda_1}\right)\right\rangle = \lambda_2^{-t}\left\langle P\left(\mathbf{k}_{\lambda_1}\right)\right\rangle \qquad (3.3.1)$$

or

$$\ln\left\langle P\left(\lambda_2^G \mathbf{k}_{\lambda_1}\right)\right\rangle = -s\ln\lambda_2 + \ln\left\langle P\left(\mathbf{k}_{\lambda_1}\right)\right\rangle \qquad (3.3.2)$$

If a field is scaling (in this case with respect to the linear Fourier space scale changing operator, $T_\lambda = \lambda^G$), this relation holds independently of the shape of the balls, for all pairs $\mathbf{k}_{\lambda_1}$, $\mathbf{k}_{\lambda_2} = \lambda_2^G \mathbf{k}_{\lambda_1}$ where λ_2 is any positive real number such that $\mathbf{k}_{\lambda_2}$ lies within the range of the data and $\mathbf{k}_{\lambda_1}$ is itself any point along the trajectory (parametrized by λ_1). Recall, from section 2.1, that a trajectory can be parametrized by λ. Therefore, to parametrize pairs of points, two parameters, λ_1 and λ_2, are needed.

A (normalized) error function, that is only a function of $G(c,f,e)$, can be defined. Since theory states that every point along a trajectory must satisfy equation (3.3.2) for continuous λ, the error function would take the form[3]:

$$E^2_{\lambda_2,\lambda_1,\zeta}(G) = \frac{1}{A}\iiint\left[\ln P\left(\lambda_2^G \mathbf{k}(\lambda_1,\zeta)\right) + s\ln\lambda_2 - \ln P\left(\mathbf{k}(\lambda_1,\zeta)\right)\right]^2 d\lambda_2 d\lambda_1 d\zeta \quad (3.3.3)$$

where ζ parametrizes the trajectories and the λ_1 and λ_2 integrations compare all pairs of points (within the range of scales where P is known) on the same trajectory, ζ, and A is the appropriate normalization factor. Note that since only points along trajectories are compared, there is no reference to the balls i.e. no unit ball need be known. The integral of equation (3.3.3), however, requires specific knowledge of $\mathbf{k}(\lambda_1,\zeta)$, which is as difficult to determine as $P_t(\mathbf{k})$. Yet, the integration over $d\lambda_1 d\zeta$ is simply an integration over an area in Fourier space (i.e. λ_1 and ζ is a coordinate system that uniquely defines a point in Fourier space, see section 2.1 and figure 2.3). Therefore, with a change of variables (or re-parametrization) to the Cartesian system, $(\lambda_1,\zeta) \Rightarrow (k_x,k_y)$ and $\lambda_2 \Rightarrow \lambda$, equation (3.3.3) may be rewritten as:

$$E^2_{\lambda,\mathbf{k}}(G) = \frac{1}{A}\int_{-k_{x\max}}^{k_{x\max}}\int_{-k_{y\max}}^{k_{y\max}}\int_1^{\lambda_m}\left[\ln P\left(\lambda^G \mathbf{k}\right) + s\ln\lambda + \ln P(\mathbf{k})\right]^2 d\lambda dk_x dk_y \qquad (3.3.4)$$

where $A = (\lambda_m - 1)\iint dk_x dk_y$

---

[3] Note that this error function can be interpreted as a least-squares fit of an experimental value (which is a function of data points) to the theoretical value zero.

and no a priori knowledge of the trajectories or balls is necessary. $k_{x\max}$ and $k_{y\max}$ are the maximum wave numbers for which P is known. Note that there will actually be a region about the origin (corresponding to the minimum know wave number) that will not be included in the integral. λ_m depends on k_x and k_y and is determined by $k_{x\max}$ and $k_{y\max}$. Only $\lambda > 1$ (i.e. only magnifications) were considered since this avoids the comparison of the same pair twice. Note that the Jacobian of the transformation is unity since $D_{el} = 2$. Since the uncertainties in estimating the parameters depend on the characteristics of the hypersurface (see below), equation (3.3.4), will determine the maximum accuracy with which the parameters can be measured using the technique. However, to evaluate $E^2_{\lambda,\mathbf{k}}$, equation (3.3.4), $P(\mathbf{k})$ must be known in functional form and not as discrete data points as is the case. Therefore, $E^2_{\lambda,\mathbf{k}}$ must be approximated as:

$$E^2_{SIG}(G) = \frac{1}{n}\sum_{i,j}\left[\ln P\left(\lambda_i^G \mathbf{k}_j\right) + s\ln\lambda_i - \ln P\left(\mathbf{k}_j\right)\right]^2 \qquad (3.3.5)$$

The sum is over all the data points, $P(\mathbf{k}_j)$, and all the possible (discrete) scale ratios, λ_i, which form the unique pair $\left[P\left(\lambda_i^G \mathbf{k}_j\right), P\left(\mathbf{k}_j\right)\right]$. It is important to note that $P\left(\lambda_i^G \mathbf{k}_j\right)$ and $P\left(\mathbf{k}_j\right)$ are data points (i.e. random variables) and therefore both will fluctuate about their average values. This will cause the minimum variance (the minimum value of E^2_{SIG}, equation 3.3.5) to be larger than the case when only one point is uncertain. However, as more statistically independent pairs are summed, the results should converge to the value of the smooth hypersurface, E^2_{∞}. As before, the number of statistically independent pairs will depend on the minimum and maximum scales (and also on the resolution) of the data set. Since all pairs along trajectories are compared, the number of pairs will be greater than the number of data points. Below, since we will deal exclusively with equation (3.3.5), the subscript will be dropped: $E^2_{SIG} \Rightarrow E^2$.

A further complication to the problem is that the fluctuations could possibly be much more variable than those described by multi-variate Gaussian distributions[4]. Therefore, there is no rigorous theoretical justification for using the method of least-

---

[4] Work on complex cascades (Schertzer and Lovejoy, 1993) indicates that the Fourier space fluctuations have essentially the same extreme variability as the real space fluctuations; for example, an $\alpha = 2$ universal multifractal with log-normal probabilities in real space will also have log-normal variations about the mean in Fourier space (see Duncan et al., 1993, for numerical study).

squares. However, it is still plausible to assume that the behavior of the hypersurface near the minimum will not be substantially altered if the fluctuations are not too violent. Logarithms of P were used in E^2, equation (3.3.5), since taking the logarithm has the effect of decreasing the variability. This could possibly lead to biased estimates. However, a similar error function, without logarithms, is not necessarily an unbiased estimator. In fact, it is possible that the bias is decreased by taking the logarithm The results shown in Chapter 4 justify the use of the method of least squares and indicate that the bias due to taking the logarithm was small.

(b) Method of searching parameter space

The preferred method of searching the parameter space for the appropriate minimum must be determined. To do this, the behavior of $E^2_{( )}$ was examined, for a large portion of the parameter space (i.e. E^2 was calculated explicitly for a theoretical ensemble average spectral energy density). $E^2_{( )}$ is shown in figure 3.4 as a function of the GSI parameters through a series of cross-sections where the parameter c is held constant. The horizontal and vertical axes are f and e, respectively. In order for the three-dimensional hypersurface to be more easily visualized, another hypersurface is shown through a series of cross-sections of constant e (figure 3.5, where the horizontal and vertical axes are c and f, respectively). It can be seen, from figure 3.4, that the concavity of $E^2_{( )}$ along the e axis is much larger relative to the concavity along the f axis. This is important since the concavity, in part, determines the accuracy with which the parameters can be estimated.

A possible method of searching the parameter space for the global minimum is the grid search (successive variation of the parameters), the method used in the Monte Carlo Differential Rotation method (see section 3.2). It was found that the characteristics of the hypersurface were such that the convergence to the absolute minimum was extremely slow (i.e. many iterations were needed to reach the minimum). It was so slow, in fact, that the change in amplitude of a parameter, due to one iteration, could possibly be smaller than the uncertainty in the estimation of the parameter. Such a search was performed on the hypersurface of figure 3.5 (with minimum at c=-0.3, f=-0.2 and e=0.2). A value of $e = -0.4$ (top center of figure 3.5) was chosen for the initial value of e. The minimum of $E^2_{( )}$, with respect to c and f, for $e = -0.4$, was found to be at $c = -0.5$ and $f = 0.3$. Note that these estimates of the absolute minimum, at c=-0.3, f=-0.2 and e=0.3, are inaccurate, therefore, at least another iteration is needed. Holding $c = -0.5$ and

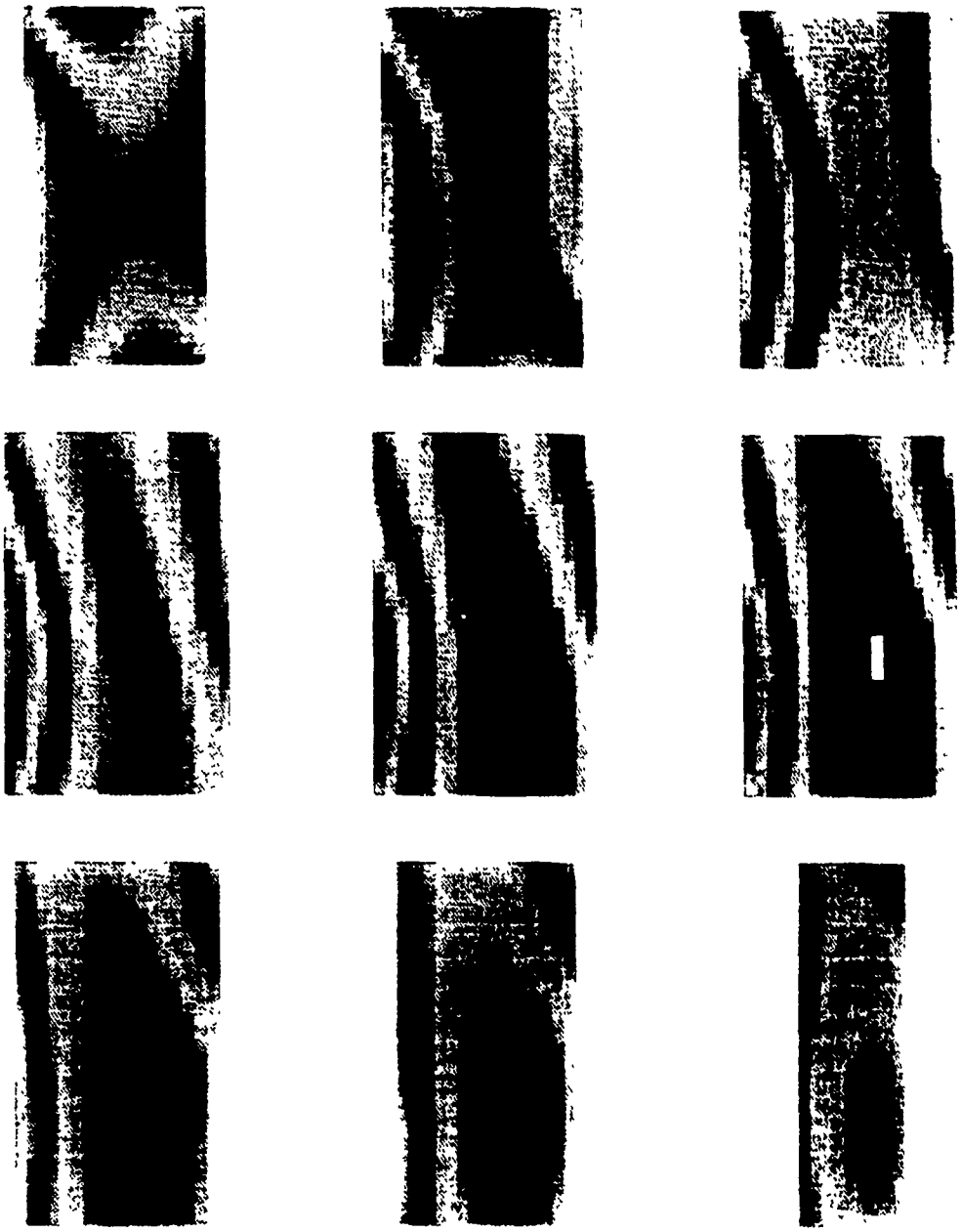

Figure 3.4 : Hypersurface of a theoretical ensemble average spectral energy density, $E^2_{(\ )}$, presented as a series of cross-sections of constant c. For a given image, f and e (the x and y axes respectively) are varied while c is held fixed. The images from left to right are the cross-sections where c=-0.7 to 0.9 in increments of 0.2. The numerical values of E^2 have been rescaled to enhance contours (values correspond to those of Palette 2 in Appendix B, gray is high, green is low and white is very low). The edges of the cross-sections correspond to $c^2 + f^2 = 1$ (see section 2.4 concerning restrictions of the GSI parmeters) and e=±1.5. The GSI parameters of P are s=2.0, G: c=0.3, f=0.2, c=0.3.

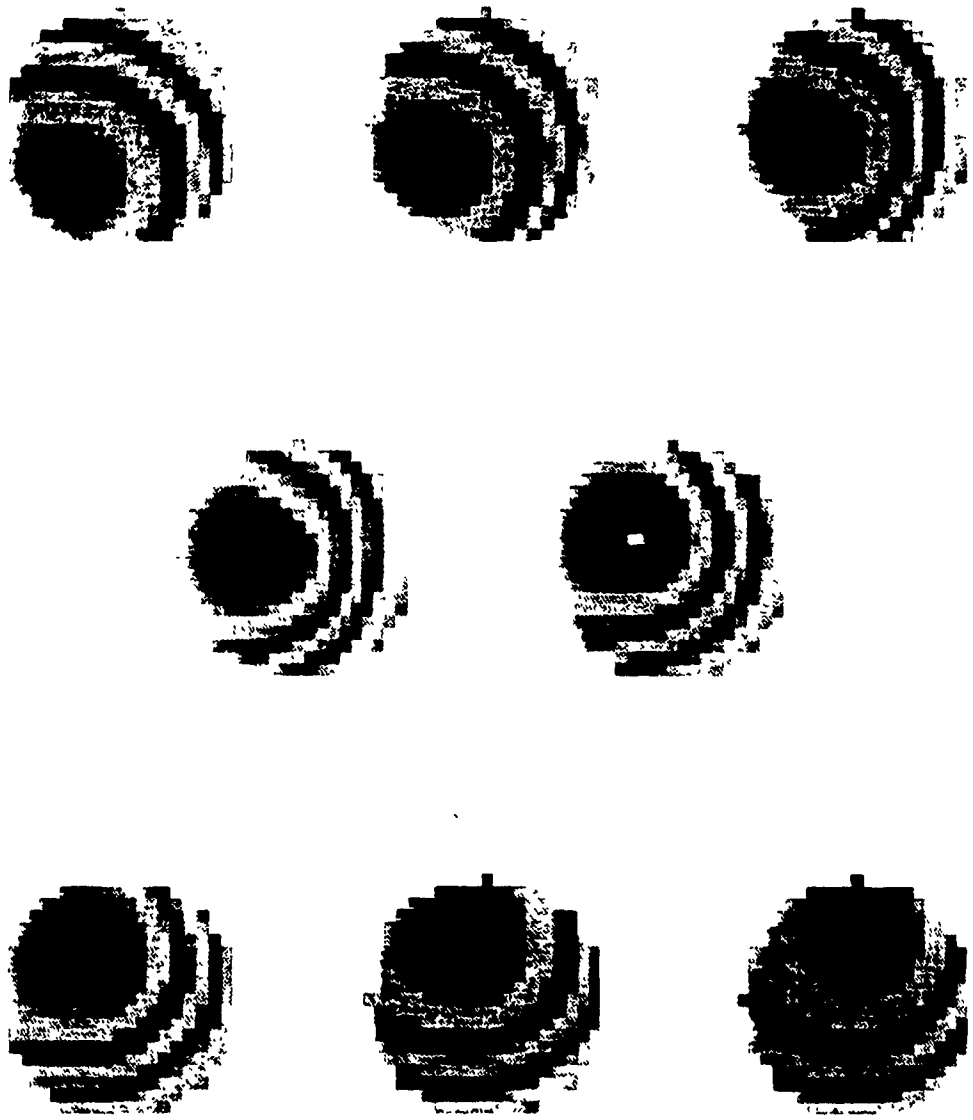

Figure 3.5 : Hypersurface of a theoretical ensemble average spectral energy density, $E^2_{\langle\ \rangle}$, presented as a series of cross-sections of constant e. For a given image, c and f (the x and y axes respectively) are varied while e is held fixed. The images from left to right are the cross-sections where e=-0.6 to 0.8 in increments of 0.2. The numerical values of $E^2_{\langle\ \rangle}$ have been rescaled to enhance contours (values correspond to those of Palette 2 in Appendix B). The edges of the cross-sections correspond to $c^2 + f^2 = 1$ (see section 2.4 concerning restrictions of the GSI parmeters). The GSI parameters of P are: s=2.0, G: c=-0.3, f=-0.2, c=0.2.

$f = 0.3$, $E^2_{(\,)}$ was plotted as a function of e (figure 3.6). The minimum was found to be at $e = -0.33$. The case examined was an ensemble average case, therefore, it is conceivable that, for a single realization, the error on the estimate of e would be of the same order of magnitude as $\Delta e = -0.33 - (-0.4) = 0.07$. This would mean the convergence would be undetectable over the noise. Also, several iterations would be needed to find the absolute minimum, thus increasing the time needed for the calculation. Another possible problem is that this technique may fail to converge to the absolute minimum if there are multiple minima. The above arguments make the grid search method unappealing. Therefore, we chose an alternative involving a parabolic expansion of the hypersurface close to the absolute minimum.

A parabolic expansion of E^2 not only smoothes the high frequency fluctuations about $E^2_{\_}$, but is also convenient because the minimum of E^2 (and thus the estimates of the parameters) is simply the solution of a system of linear equations. However, the hypersurface is not globally parabolic, therefore, the expansion is a reasonable estimate only in a neighbourhood of the absolute minimum. The neighbourhood was found to be much smaller than the extent in parameter space in which the absolute minimum would be expected to lie (see section 3.3.2d). Therefore, it was necessary to obtain initial estimates of the parameters. Conventional estimation methods (e.g. gradient search, Press et al., 1986) were not used since substantial difficulty is caused by the fluctuations about $E^2_{\_}$. A less efficient but more accurate method, a type of ravine search, was used.

A ravine is the path of least resistance toward the minimum (e.g. in analogy to topography, it is the course a river would follow). Good initial estimates of the parameters can be found by fitting a one-dimensional parabola to the projection of the ravine onto the respective axes. However, if the ravine is not steep, relative to the fluctuations, it will cause errors in the initial estimates. Approximations to the projections of the ravine were found by searching the portion of parameter space where the minimum was expected to lie and recording the minimum of the hypersurface for the given value of the parameter, regardless of the value of the others. For example, the value of $E^2_e(e=0)$ (where E^2_e is the projection of the ravine onto the e axis) was the minimum value of $E^2(c,f,e=0)$ over all possible values of c and f. On average, this point will be along the ravine. This was carried out for several values of e for the theoretical hypersurface of figure 3.5. The minimum of each cross-section is plotted in figure 3.7. The initial estimate of e is the minimum of the one-dimensional parabola fit to the values of E^2_e.

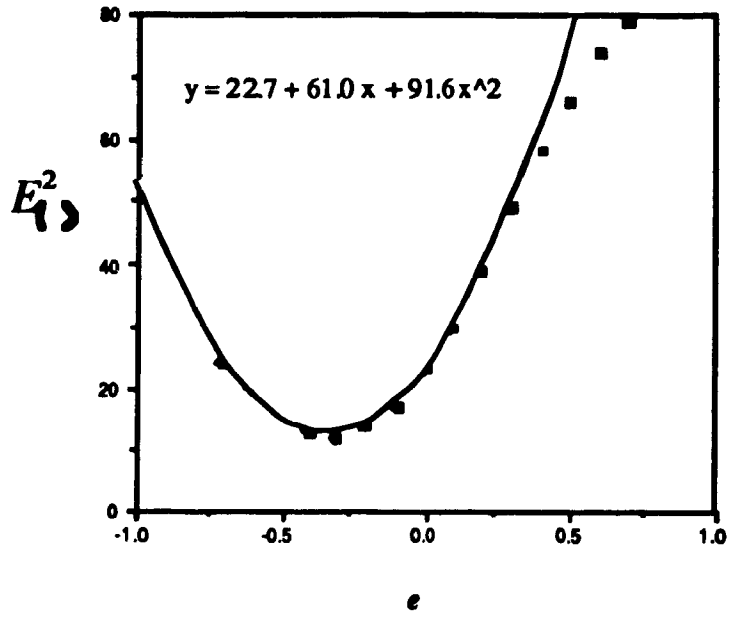

Figure 3.6 : Results of a grid search of the hypersurface of Figure 3.5, where e was varied while c and f were held fixed at -0.5 and 0.3, respectively (see text). The minimum is at e=-0.33. The equation of the parabola that was fit to the data near the minimum is included in the figure. The absolute minimum is at: c=-0.3, f=-0.2, e=0.3. Numerical values are as in figure 3.5.

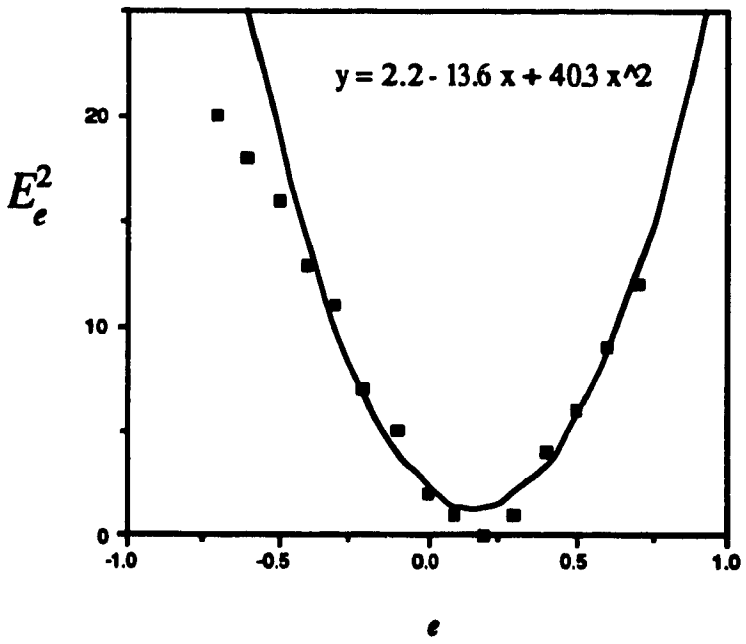

Figure 3.7 : Results of a ravine search of the hypersurface of figure 3.5, where the data points represent the minimum of the hypersurface of the corresponding value of e (over all possible c and f). The minimum is at e=0.17 and the equation of the parabola, that is fit to the data near the minimum, is shown. The absolute minimum is at: c=-0.3, f=-0.2, e=0.3. Numerical values are as in Figure 3.5.

In summary, SIG calculates E^2, the error function of equation (3.3.5), numerically at intervals in parameter space. Due to the fluctuations of the data points about the ensemble average, the numerical values of E^2 fluctuate about E^2_{∞}. Initial estimates of the parameters are found using the ravine search and a parabolic expansion of E^2 in three dimensions is then made about the initial estimates. The parabolic expansion is necessary to smooth the fluctuations about E^2_{∞}. The parameter estimates are taken to be the minimum of the parabola.

3.3.2 Further Details of the Scale Invariant Generator Technique

Before the Scale Invariant Generator technique can be applied, some details must be examined. For example, the error function, E^2 of equation (3.3.5), compares all pairs of points along a trajectory. This would mean comparing approximately $L^2/4$ pairs, where there are L^2 data points. It is expected that not all pairs need be considered in order to obtain a reasonable estimate of the value of E^2_{∞} (if only because many of the $L^2/4$ pairs will be statistically dependent). If this is true, the number of pairs that are necessary, and a method of choosing these pairs, must be found. Also, it must be determined how many points in parameter space (where E^2 will be found explicitly) are needed for a reasonable estimate of E^2_{∞}. The uncertainties will be used to determine the appropriate choices since the uncertainties theoretically determine the accuracy of the estimates. Therefore, the effects of the above choices on the uncertainties will be examined. These choices are important since our goal is not only to find a method that produces good estimates, but one that is efficient as well.

(a) Uncertainties

To determine the uncertainties, the procedure of estimating the parameters will be examined in more detail. The hypersurface was estimated by a function of the form:

$$E^2 \sim E^2_{est} = E^2_o + \sum_{k=1}^{3} \frac{\partial E^2_o}{\partial g_k} \Delta g_k + \frac{1}{2} \sum_{k=1}^{3} \sum_{l=1}^{3} \frac{\partial^2 E^2_o}{\partial g_k \partial g_l} \Delta g_k \Delta g_l \qquad (3.3.6)$$

i.e. a parabolic expansion about the initial estimates, g_{o_k}, found using the ravine search, where g_k are the GSI parameters (c, f, e), $\Delta g_k = \left(g_k - g_{o_k}\right)$ and the ten parabolic coefficients, $p^{(i)}$:

$$p^{(0)} = E_o^2, \quad p_k^{(1)} = \frac{\partial E_o^2}{\partial g_k}, \quad p_{kl}^{(2)} = \frac{\partial^2 E_o^2}{\partial g_k \partial g_l} \tag{3.3.7}$$

are the derivatives of E^2 with respect to g_k at $\left(g_{o_1}, g_{o_2}, g_{o_3}\right)$.

The $p^{(i)}$ were found by a least-squares fit to the numerically calculated values of E^2 at m points in parameter space (this will be discussed further below). The parameter estimates were then $g_{\min_k} = \Delta g_{\min_k} + g_{o_k}$, where $\Delta g_{\min_k}$ were the solutions to the system of linear equations:

$$\frac{\partial E_{est}^2}{\partial \Delta g_k} = 0 \tag{3.3.8}$$

i.e. $$\alpha(\Delta \mathbf{g}) = \beta \quad \text{or} \quad \Delta \mathbf{g} = \beta\varepsilon \tag{3.3.9}$$

where $\varepsilon = \alpha^{-1}$, $\Delta \mathbf{g} = \left(\Delta g_1, \Delta g_2, \Delta g_3\right)$, $\alpha_{ij} = \frac{1}{2}\frac{\partial^2 E_o^2}{\partial g_k \partial g_l}$, and $\beta_k = -\frac{1}{2}\frac{\partial E_o^2}{\partial g_k}$. α is called the curvature matrix because it contains the information about the curvature of the parabola. ε is the error matrix (it will be used to determine the uncertainties).

Since the minimum of E^2 was not found analytically, neither can the uncertainties. However, they can be estimated by making an analogy to the case when an analytic solution is possible (i.e. the case when the curvature matrix describes the hypersurface exactly, see Bevington, 1969 for discussion). The estimated uncertainties on $g_{\min_k}$ will then be:

$$\sigma_{g_k}^2 = \frac{\varepsilon_{kk} E_{\min}^2}{n} \tag{3.3.10}$$

where ε_{kk} are the diagonal elements of the error matrix, n is the number of pairs of data points compared (as in E^2) and E^2_{min} is the value of E^2 at its minimum (approximately equal to the sample variance).

The estimated uncertainties, $\sigma^2_{f_k}$, are expected to approach the actual uncertainties as the hypersurface is more accurately approximated by a parabola and as the error in determining the parabolic coefficients decreases. Note that equation (3.3.10) also assumes that the n pairs are statistically independent. Since this condition is not expected to hold for all pairs, it will be an additional source of error.

(b) Choice of pairs

A better estimate of the parameters is expected as $\sigma^2_{f_k}$ decreases. Therefore, increasing the number of pairs or decreasing the ε_{kk} (i.e. increasing the curvature since $\varepsilon = \alpha^{-1}$) will improve the results. Considering this, the effect on the curvature due to the choice of pairs, $\left[P\left(\lambda_i^G \mathbf{k}_j\right), P\left(\mathbf{k}_j\right)\right]$, was examined. The choice of pairs corresponds to a choice of $\mathbf{k}_j$ and λ_i. Since the location of the first element of the pair, $P\left(\lambda_i^G \mathbf{k}_j\right)$, is calculated, it is not known a priori if that element lies within the range of the data. If a choice, $\left(\lambda_i, \mathbf{k}_j\right)$, is made such that $\lambda_i^G \mathbf{k}_j$ lies outside the range, it cannot be considered as one of the n pairs used in E^2 and thus it will not contribute to reducing the uncertainty. The same may be said if the same pair is considered twice. Since all pairs take the same time to be calculated, it would be more efficient to avoid the pairs which did not contribute. For this reason, it would be beneficial to control the choice of pairs by choosing them systematically as opposed to randomly (as in the Monte Carlo Differential Rotation method).

The initial distribution, $\mathbf{k}_j$, was chosen from a rectangular region about the origin in Fourier space (i.e. $k_x = [-W, 0]$ and $k_y = [-W, W]$, where W is the width of the rectangular region). See figure 3.8. A rectangular region is considered since the spectral energy density will have the property $P(\mathbf{k}) = P(-\mathbf{k})$. Δk is the interval at which the points inside the rectangle will be chosen (i.e. $\Delta k = 2$ means every other point will be taken). The λ_i will be chosen from $\lambda_i = \left[\Delta\lambda, \lambda_{max}\right]$ at certain intervals. These intervals will be taken uniformly in $\ln\lambda$ because the fluctuations about the theoretical contours of the spectral energy density go as $\ln\lambda$. This will slightly alter the error function, however, the difference will be an unimportant weighting factor. All the $\ln\Delta\lambda$ will be positive so that only magnifications are considered. This is to ensure that all the pairs are

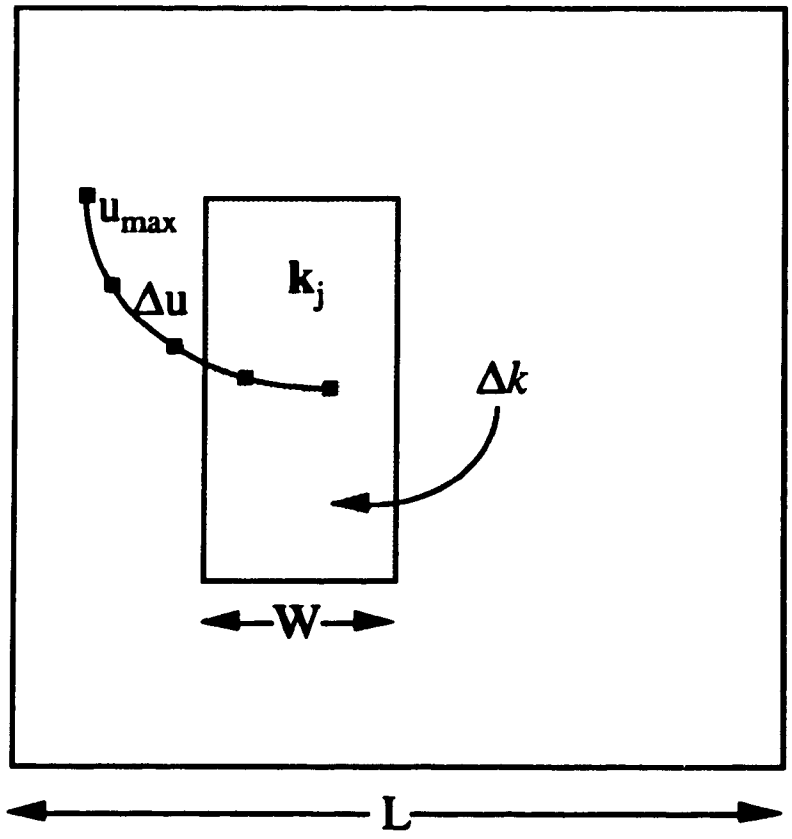

Figure 3.8 : Pictorial demonstration of variables involved in the choice of pairs for the numerical calculation of equation (3.3.5).

unique. It is more convenient to write λ_i as $u_i = \ln \lambda_i$ such that: $u_i = [\Delta u, u_{max}]$ in steps of Δu.

The effects on the hypersurface (and thus on the uncertainties) for changes in W, Δk, Δu and u_{max} were investigated by performing the analysis on a theoretical ensemble average energy spectral density (figure 3.1). The investigation was performed for a single choice of G. Although this choice is expected to cause small changes in the observations, the general behavior of all hypersurfaces due to changes in W, Δk, Δu and u_{max} is expected to be very similar. To facilitate the computation and presentation, $E^2_{(\,)}$ was found as a function of e while c and f were fixed at their theoretical values. The same behavior is expected on this one-dimensional cross-section as on the full hypersurface.

Varying Δk, W and Δu, while all others were held fixed, showed little effect on the cross-section of the hypersurface (see figures 3.9, 3.10 and 3.11). u_{max} (figure 3.12), however, was shown to have a substantial influence (the larger the u_{max}, the greater the concavity). This implies that it would be beneficial to use a large u_{max}. However, for a given W and Δk, n will generally decrease as u_{max} increases, since more pairs will fall outside the range of the data due to larger magnifications. Consequently, if a larger u_{max} is desired, a smaller W is needed. However, it is not desirable to over sample a small subset of points since it could possibly introduce biases. To keep n large, it is also possible to decrease Δk or Δu. Yet there will be correlations between neighbouring points in Fourier space. If the data points at $\left(e^{l\Delta u}\right)^G \mathbf{k}_j = \lambda^G \mathbf{k}_j$ and $\left(e^{(l+1)\Delta u}\right)^G \mathbf{k}_j$ (where $\ln \lambda = l\Delta u$ and l is some integer between 1 and $u_{max}/\Delta u$) are correlated, then the situation is similar to when the same pair is considered twice: the repeated pair will not contribute to a reduction of the uncertainties. Thus, it is not beneficial to choose Δu to be too small. Unfortunately, any Δu (for which the choice of n corresponds to reasonable uncertainties) might yield correlated pairs. In effect, this will cause an underestimation of the uncertainties of equation (3.3.10), since not all pairs will be independent.

Yet another factor to consider is how n effects the fluctuations about E_∞^2. An increase in n will cause a decrease in the amplitude of the scatter (in some non-trivial manner), such that a more accurate estimate of the hypersurface can be made. Unfortunately, there is no analytical method for solving for the optimum combination of W, Δk, Δu and u_{max} since the possibility of biasing due the choice of W, the correlations, and n for given W, Δk, Δu and u_{max} will differ from scene to scene depending on the data and the GSI parameters that best describe the field. In effect, the above arguments can only guide our selection which will be, to some degree, arbitrary.

In summary, W, Δk and Δu effect the accuracy of the estimates primarily in their contribution to n. However, correlations and sample biasing must be considered when choosing them. An increase in u_{max} will increase accuracy, however, it must alter the choice of Δu and W and more pairs can be expected to fall outside the range of the data.

The choices of W, Δk, Δu and u_{max} were made such that:

$$\sigma_\varepsilon^2 = \frac{\varepsilon_{\varepsilon\varepsilon} E_{min}^2}{n} \sim 0.05 \qquad (3.3.11)$$

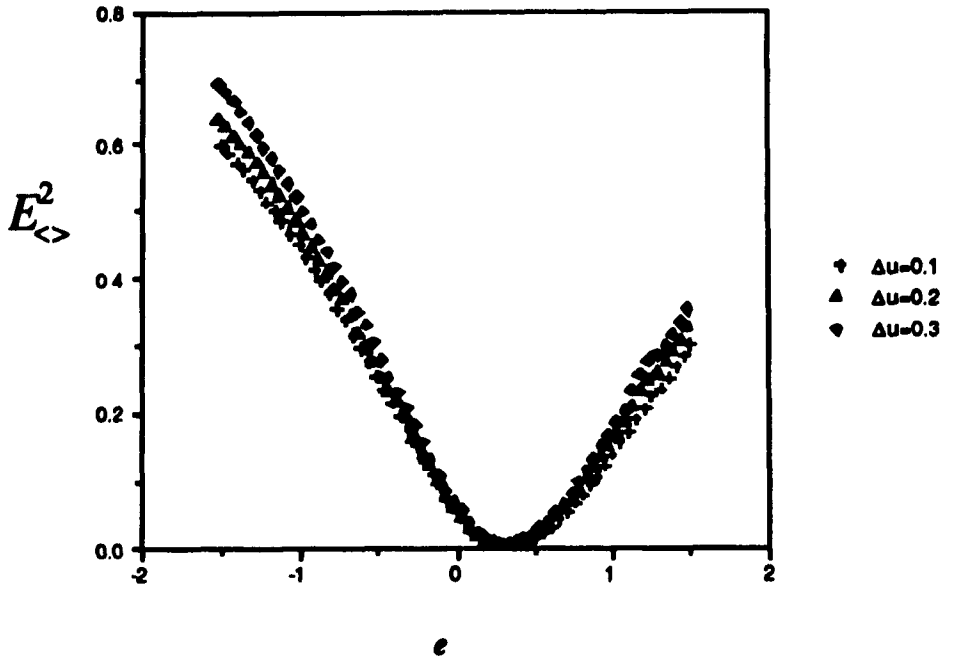

Figure 3.9 : Effect of change in Δu on hypersurface of a theoretical ensemble average spectral energy density shown in three one-dimensional cross-sections for Δu=0.1, Δu=0.2 and Δu=0.3. It can be seen that, near the minimum, there is little difference in the curvature for the different cross-sections.

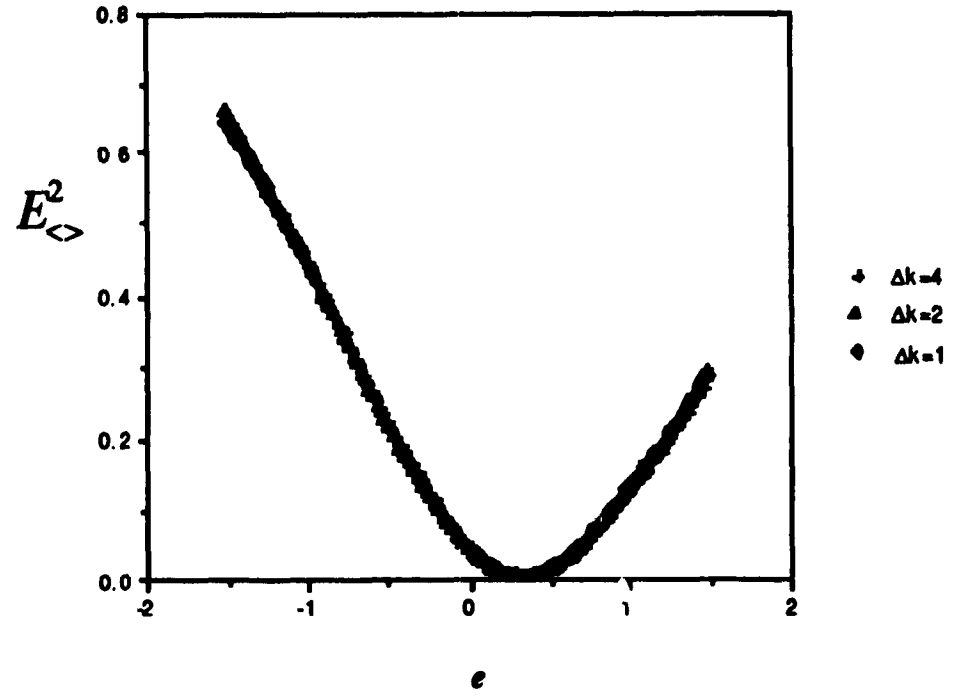

Figure 3.10 : Effect of change in Δk on hypersurface of a theoretical ensemble average spectral energy density shown in three one dimensional cross-sections for Δk=1, Δk=2 and Δk=4. It can be seen that this change has little effect.

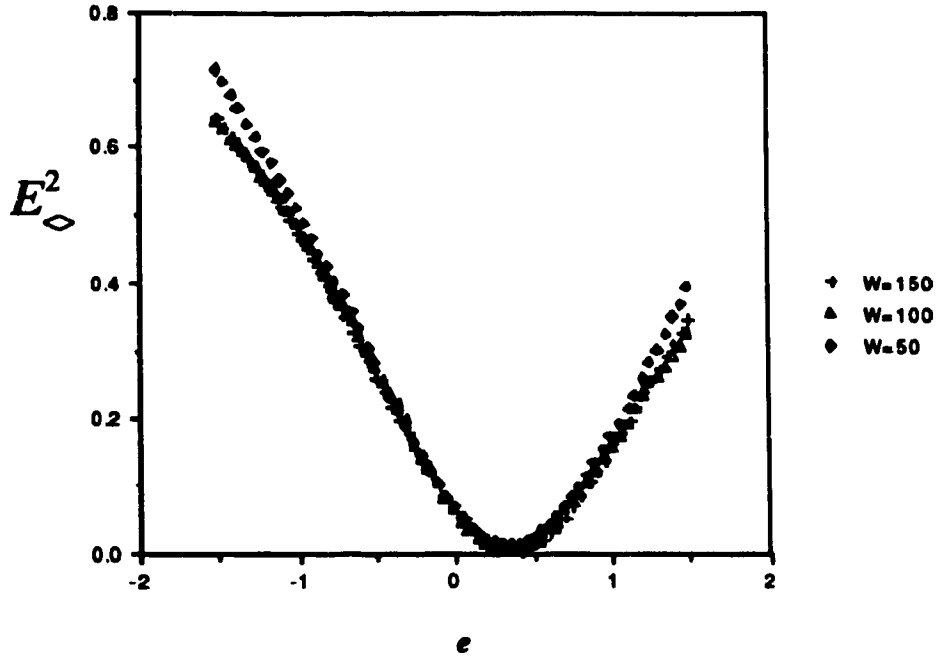

Figure 3.11 : Effect of change in W on hypersurface of a theoretical ensemble average spectral energy density shown in three one-dimensional cross-sections for W=50, W=100 and W=150. It can be seen that, near the minimum, there is little difference in the curvature for the different cross-sections.

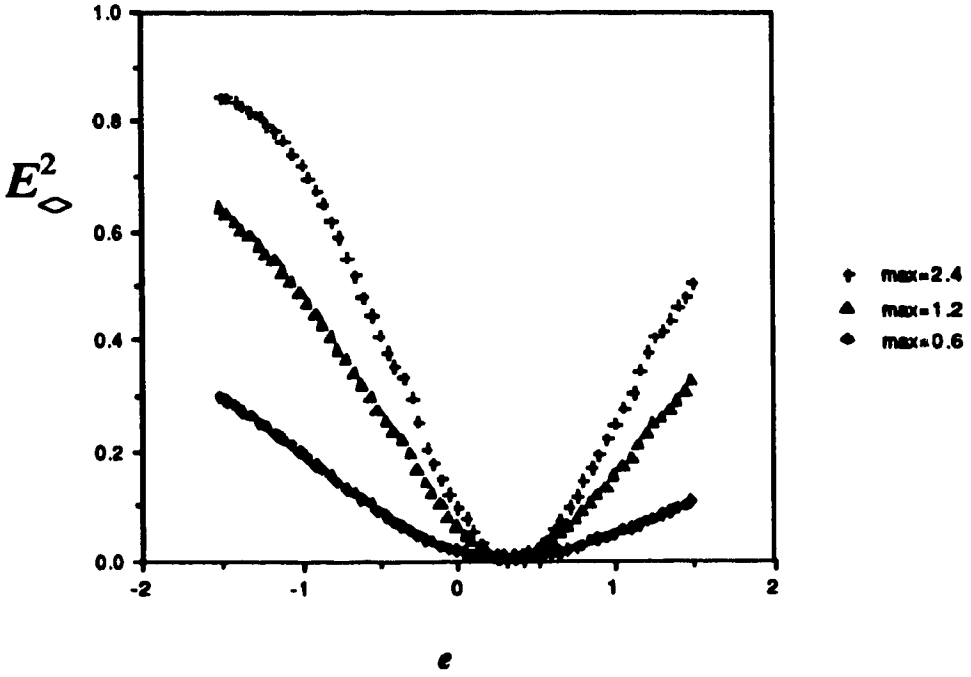

Figure 3.12 : Effect of change in u_{max} on hypersurface of a theoretical ensemble average spectral energy density shown in three one-dimensional cross-sections for u_{max}=2.4, u_{max}=1.2 and u_{max}=0.6. It can be seen that changes in u_{max} have a substantial effect on the curvature of the hypersurface.

from equation (3.3.10) with k=3 (c and f are generally more accurate). This number was chosen because it is of the same order of magnitude as the error expected due to making the parabolic expansion over too large of a range about the first estimate of the minimum (i.e. the points used to estimate the parabola covered too large a volume for the surface to be well approximated by a parabola, see below). The numbers quoted directly below apply to an image size of 512×512 pixels, with multifractal parameters approximately those measured empirically in cloud radiances (see table 1.1). The extent of the validity of these choices, with respect to a change in the multifractal parameters, are discussed in section 4.3. For this case, W, Δk, Δu and u_{max} were chosen as:

$$W = 100 \qquad \Delta k = 2 \qquad \Delta u = 0.2 \qquad u_{max} = 1.2 \qquad \Rightarrow \qquad n \sim 31000 \tag{3.3.12}$$

It should be noted that there are many other possible choices that could have been made. In fact, other choices were tested and were found to give similar results (which indicates the robustness of the technique).

(c) Parabolic expansion of E^2

We now consider the problem of the parabolic expansion of the hypersurface. If E^2 is found numerically at more points in parameter space, a better approximation can be made. The error on the parabolic coefficients, $p^{(i)}$, from equation (3.3.7), will result in an error in the minimum. However, the estimates of the parameters cannot be more accurate than the sample variance, E^2_{min}, and the curvature of the parabola permit. Therefore, it is not necessary to obtain excessive accuracy for an estimate of the hypersurface. Note that the uncertainties on the $p^{(i)}$, $\sigma^2_{p^{(i)}}$, and thus the uncertainties on the minimum of the parabola due to $\sigma^2_{p^{(i)}}$, are dependent on the estimated uncertainties, $\sigma^2_{\delta_k}$. Therefore , the 'total' uncertainty on the parameters will not be the sum of the two. Actually, we will assume that the uncertainties of the minimum of the parabola due to $\sigma^2_{p^{(i)}}$ will be negligible if they are of the same order of magnitude as $\sigma^2_{\delta_k}$. Thus, the number of points, m, in parameter space where E^2 will be calculated, will be chosen such that $\sigma^2_{\epsilon_p} \sim 0.05$ and similarly for the other parameter's uncertainties.

The uncertainties on the parabolic coefficients, $\sigma^2_{p^{(i)}}$, can be found from the error matrix of the least-squares fit of the m points to the parabola, E^2_{est} (equation 3.3.6) and the sample variance, s^2_p, due to the scatter about the hypersurface:

$$\sigma^2_{p^{(i)}} = \frac{\varepsilon_{pp} s^2_p}{m} \tag{3.3.13}$$

It would be algebraically tedious to solve explicitly for the error on the minimum due to $\sigma^2_{p^{(i)}}$ (the minimum is the solution to the system of equations shown in equation 3.3.8). Therefore, since only an order of magnitude estimate is required, we will estimate the error by examining the one-dimensional cross-section of the three parameters about the (known) minimum of E^2 of a (simulated) single realization. That is, one-dimensional parabolas, which are functions of only one parameter while the others are held fixed, will be examined. The one-dimensional cross-section of the hypersurface as a function of e is:

$$E^2_{est}(c = c_{\min}, f = f_{\min}, e) = p^{(2)}_{33} e^2 + \left(p^{(2)}_{31} c_{\min} + p^{(2)}_{32} f_{\min} + p^{(1)}_3\right) e + A \tag{3.3.14}$$

where $p^{(2)}_{33} = \frac{1}{2}\frac{\partial^2 E^2_o}{\partial e^2}$, $p^{(2)}_{31} = \frac{1}{2}\frac{\partial^2 E^2_o}{\partial e \partial c}$, $p^{(2)}_{32} = \frac{1}{2}\frac{\partial^2 E^2_o}{\partial e \partial f}$, $p^{(1)}_3 = \frac{\partial E^2_o}{\partial e}$ and A is independent of e. These are the $p^{(i)}$ of equation (3.3.7) with g_k replaced explicitly with the GSI parameters and the $g_{\min_k}$ are also explicitly replaced.

The minimum is located at:

$$e_{\min} = \frac{-\left(c_{\min} p^{(2)}_{31} + f_{\min} p^{(2)}_{32} + p^{(1)}_3\right)}{2 p^{(2)}_{33}} \tag{3.3.15}$$

Assuming that the $\sigma^2_{p^{(i)}}$ are independent, the standard deviation of $e_{\min}$ due to $\sigma^2_{p^{(i)}}$ is:

$$\Delta e = \sum_i \frac{\partial e_{\min}}{\partial p^{(i)}} \sigma_{p^{(i)}} \tag{3.3.16}$$

where $\sigma^2_{p^{(i)}}$ is the standard deviation of $p^{(i)}$. So,

$$\frac{\Delta e}{e} = \frac{\sigma_{p_{33}^{(2)}}}{p_{33}^{(2)}} + \frac{c_{\min}\sigma_{p_{31}^{(2)}} + f_{\min}\sigma_{p_{32}^{(2)}} + \sigma_{p_3^{(1)}}}{c_{\min}p_{31}^{(2)} + f_{\min}p_{32}^{(2)} + p_3^{(1)}} \qquad (3.3.17)$$

(There are similar expressions for the other parameters.) Varying m gave the results in Table 3.1. Thus, m=250 was used.

m	σ in c due to $\sigma_{p^{(i)}}$	σ in f due to $\sigma_{p^{(i)}}$	σ in e due to $\sigma_{p^{(i)}}$
48	0.055	0.075	0.259
250	0.008	0.013	0.036
1500	0.001	0.002	0.007

Table 3.1 : Estimation of the standard deviations in the measurement of the minimum of the parabola (and thus the parameter estimates) due to uncertainties in the parabolic coefficients.

Finally, the optimum range of the parabolic expansion must be considered. Ideally, the range would correspond to the neighbourhood, about the minimum, where the hypersurface is well approximated by a parabola. However, if the range is too small, it is possible that the curvature would not be detectable over the fluctuations. If the range is too great, the higher order terms in the expansion of the hypersurface become non-negligible and errors are introduced. The optimum range was estimated by performing the analysis on a theoretical ensemble average spectral energy densities. The results of two cases studied, over the ranges given in Table 3.2, are presented in Tables 3.3 and 3.4. Although Range 3 seems to give the better results in the cases below, when the analysis was performed on single realizations, it was found to be too small (relative to fluctuates). Therefore, Range 2 is a better choice when considering multifractal parameters as those found empirically in clouds, since the biases are not too great. The error due to the non-infinitesimal range is expected to change depending on the choice of parameters, as well as the fluctuations. It was *judged* that there was fairly small change in the contours and that the morphology of the fields did not differ greatly due to changes of this magnitude in the parameters. Figure 3.13 shows two simulations whose parameter e differs by 0.1.

	c	f	e
Range 1	± 0.4	± 0.3	± 0.4
Range 2	± 0.3	± 0.2	± 0.3
Range 3	± 0.2	± 0.1	± 0.2

Table 3.2 : Definition of ranges of the parabolic expansion of hypersurface used for Tables 3.3 and 3.4.

	c	f	e
theoretical values	0.3	0.2	0.3
Range 1	0.318	0.208	0.387
Range 2	0.302	0.202	0.354
Range 3	0.300	0.200	0.313

Table 3.3 : Results of the analysis on theoretical ensemble average spectral energy density for different ranges in the parabolic expansion (Case 1). See Table 3.2 for definitions of ranges.

	c	f	e
theoretical values	0.1	0.1	0.5
Range 1	0.080	0.096	0.535
Range 2	0.084	0.098	0.501
Range 3	0.091	0.099	0.501

Table 3.4 : Results of the analysis on theoretical ensemble average spectral energy density for different ranges in the parabolic expansion (Case 2). See Table 3.2 for definitions of ranges.

It should be noted that if the absolute minimum is outside the range of the expansion, the parameter estimates will generally be as well. The estimates will be poor and will generally lie in the direction of the absolute minimum. Therefore, if the parameter estimate lies outside the initial range, another parabolic expansion should be made, where the range should be adjacent to the initial and in the direction of the estimates. However, this was rarely the case since the first estimates of the ravine search were fairly accurate.

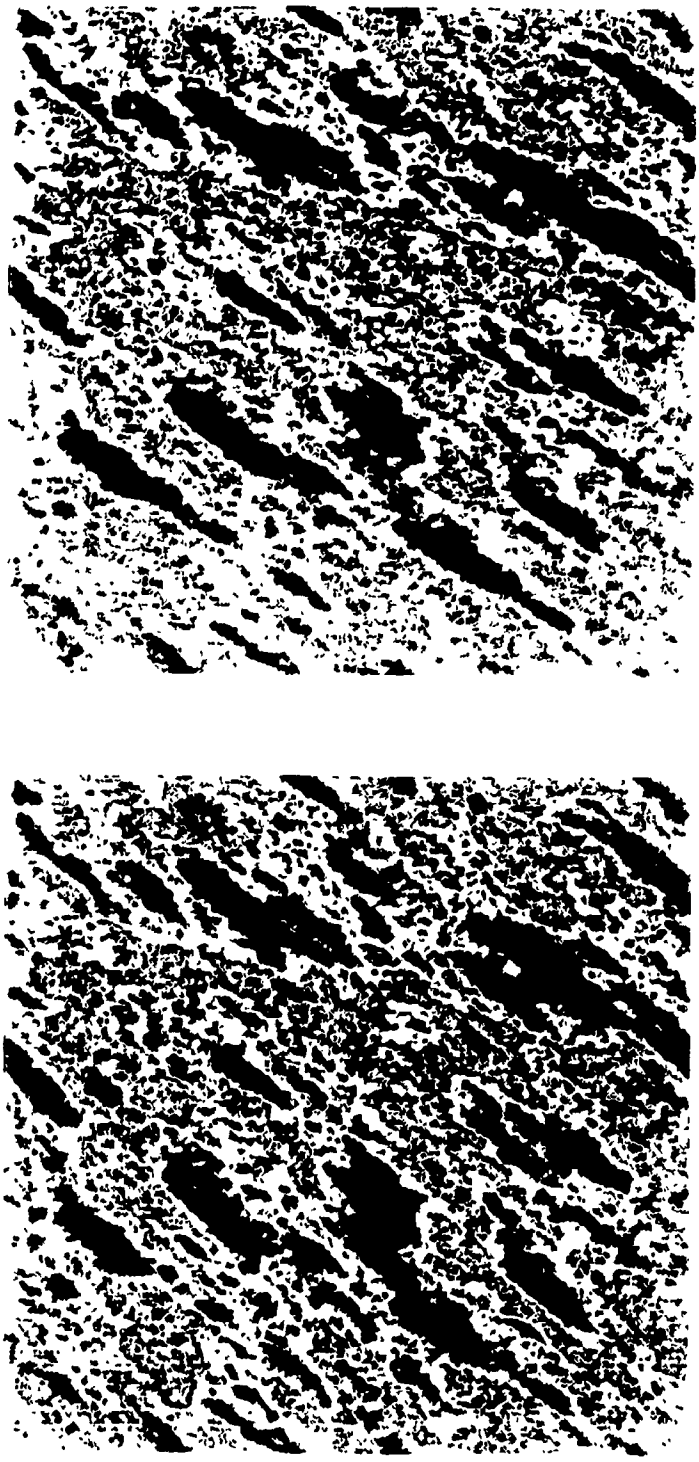

Figure 3.13 : Comparison of multifractal simulations with similar GSI parameters: c=0.3, f=0.2, e=0.3 (top), and c=0.3, f=0.2, e=0.2 (bottom). The continuous Palette 3 is used. Red represent high values and blue low.

(d) Details of the ravine search

Since the ravine search found the values of E^2 explicitly for points at intervals in the parameter space, it is desirable to restrict the search to a volume where the minimum is expected to lie. Restrictions on the generator (i.e. the real parts of the eigenspectrum must be positive, see section 2.4) could be used to limit the search. This restriction for the case of linear GSI is:

$$c^2 + f^2 - e^2 < 1 \qquad (3.3.18)$$

(where d=1)This still corresponds to an infinite volume in parameter space, therefore, further restrictions should be made. It may be possible to use the fact that, after the generator parameters are found, equations of the form (2.3.5) and (2.3.7) are to be used to approximate the balls. This imposes further constraints on the generator parameters to ensure the validity of the GSI system (see section 2.4). These restrictions generally depend on both the generator and the ball parameters and, since the ball is not known a priori, they are of limited usefulness. Nevertheless, they may be used to estimate the relevant volume.

If a sphero-scale is assumed to exist, the parameters must satisfy equation (2.4.31):

$$c^2 + f^2 < 1 \qquad (3.3.19)$$

In most of the cases when the ball is approximated by an equation of the forms (2.3.5) or (2.3.7), this is nearly a sufficient restriction. For example, $c^2 < 1$ and $f^2 < 1$ (the condition of equation 2.4.32) is imposed if any member of the family of balls has a_1 or b_1 equal 0 and the conditions of equation (2.4.34) are often more stringent than equation (3.3.19). Also, the magnitude of e is not expected to exceed 1.5 (by inspection of the restrictions of equations (2.4.30) and (2.4.34) and by the limited experience we have with geophysical fields analyzed so far). Therefore, the volume of the search can be chosen so that it satisfies:

$$c^2 + f^2 < 1, \qquad e = [-1.5, 1.5] \qquad (3.3.20)$$

Although, all possible cases will not satisfy these conditions, most will. If the absolute minimum lies outside this region, the ravine search will not find a minimum within the volume and the search must be readjusted. This solution is not ideal, however, if the restrictions are not made, computation time increases substantially. One of the simulations that was analyzed (see Chapter 4) had parameters that did not satisfy equation (3.3.20) and valid results were still obtained. Examples of a ravine search are plotted in section 4.1 and 5.2.

3.3.3 Estimation of the GSI Ball Parameters

The next step in the Scale Invariant Generator technique is the estimation of the family of balls. Once any one member of the family of balls is found, the whole family can be generated, since the generator has already been estimated (see section 2.1 and 3.3.1). Thus, the estimation consists of finding the parameters that describe a unit ball. As stated in section 2.3, the balls will be approximated by the second or fourth order bivariate polynomials of equation (2.3.1) and (2.3.2), respectively. The relevant parameter space will therefore be three or five dimensional.

Unlike the generator parameters, the ball parameters may be found using an analytic method. The ball parameters may be found by fitting a curve of the appropriate form to a levelset of the spectral energy density (as discussed in section 3.2). It was stated that the large fluctuations about the ensemble average contours cause undesirable errors in the parameter estimates. Ideally, the spectral energy density, P, could be smoothed before the fitting procedure. However, conventional smoothing (e.g. averaging adjacent data points) causes non-uniform spreading of the contours of P and consequently, the smoothed field will not be described by the same GSI parameters as the actual P.

Assuming that the estimates of the generator parameters, found using the error function of equation (3.3.5), E^2, are reasonably accurate, they can be used to 'enhance' the contours of P without effecting the scaling of the field. Regardless of this assumption, fitting a curve to a levelset of the enhanced P will find the best estimate of a unit ball given the estimated generator parameters.

The enhancing technique consists of applying a running average to the data points that lie on the same trajectory (see section 2.1). The same principle, that was used for E^2, is implemented again i.e. the fact that the amplitude of any two data points on the same trajectory will be on average related by equation (3.3.1):

$$\left\langle P\left(\lambda_2^G \mathbf{k}_{\lambda_1}\right)\right\rangle = \lambda_2^{-s}\left\langle P\left(\mathbf{k}_{\lambda_1}\right)\right\rangle \tag{3.3.21}$$

Thus, if the amplitude of all the points along a trajectory, $\mathbf{k}_{\lambda_2} = \lambda_2^G \mathbf{k}_{\lambda_1}$, are transformed to a point, $\mathbf{k}_{\lambda_1}$, then the transformed amplitudes, $\lambda_2^s P\left(\lambda_2^G \mathbf{k}_{\lambda_1}\right)$, will fluctuate about the ensemble average value, $\left\langle P\left(\mathbf{k}_{\lambda_1}\right)\right\rangle$. Averaging the $\lambda_2^s P\left(\lambda_2^G \mathbf{k}_{\lambda_1}\right)$ will then give an estimate of $\left\langle P\left(\mathbf{k}_{\lambda_1}\right)\right\rangle$.

As in section 3.3.1, an approximation is made such that only M data points are used in the running average. That is, to generate the enhanced P, $P_{en}\left(\mathbf{k}_j\right)$, the amplitude of each data point, $P\left(\mathbf{k}_j\right)$, is replaced by:

$$P_{en}\left(\mathbf{k}_j\right) = \frac{1}{M}\sum_{i=0}^{M} \lambda_i^s P\left(\lambda_i^{-G}\mathbf{k}_j\right) \tag{3.3.22}$$

where λ_i were incremented by intervals of $\Delta u = 0.2$ (as in section 3.3.2) and M was chosen to be six. It can be see from the figures in Chapter 4 that the enhancing technique has a substantial smoothing effect. This effect can also be seen in figure 3.14, where a levelset of a $P_{en}\left(\mathbf{k}_j\right)$ and one of a normal single realization are compared. The points correspond to the data points which had amplitude 16.00 ± 0.04.

Here, the parameters of a unit ball, B_1 at some chosen P_1, were found by fitting a curve of form of equation (2.3.5) or (2.3.7) to a levelset of $P_{en}\left(\mathbf{k}_j\right)$. If increased statistics are required, the parameters of several such balls (by choosing several P_i) can be estimated and transformed (with the known generator parameters, using the idea of section 2.4) to some arbitrary scale, where they can be averaged. The scale ratio of the transformation will be:

$$\lambda = \left(\frac{P_i}{P_{orb}}\right)^{-1/s} \tag{3.3.23}$$

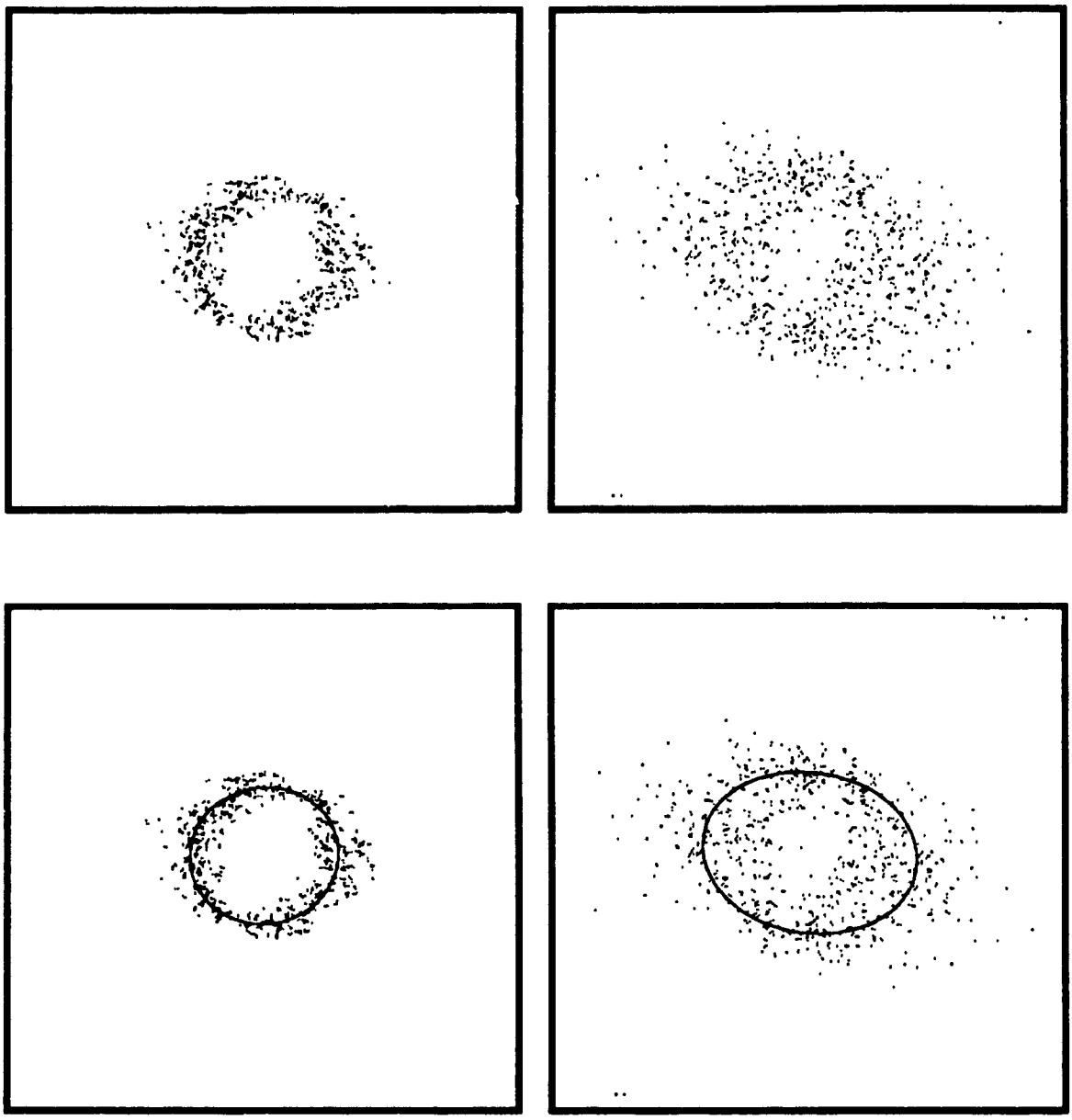

Figure 3.14 : Comparison of levelsets of the spectral energy density. TOP LEFT: levelset of enhanced P. TOP RIGHT: levelset of a single realization (before enhancing) at the same level. A curve of the form (2.3.5) is drawn through the levelsets of the enhanced P (bottom left) and single realization (bottom left). It can be seen that fitting a curve to the pre-enhanced levelset causes large biases.

where P_{arb} arbitrarily determines the choice of scale. Alternatively, all the points of $P_{sn}(\mathbf{k}_j)$ can be transformed to some arbitrary scale using the known generator, thus increasing the number of points used in the estimation of the unit ball. The scale ratio of the transformation will be:

$$\lambda = \left(\frac{P_{sn}(\mathbf{k}_j)}{P_{arb}} \right)^{-1/4} \tag{3.3.24}$$

where P_{arb} is chosen arbitrarily and determines the final scale.

Given that the family of balls are described by equation (2.3.1), it may be instructive to discover whether a sphero-scale exists. This can be done by using the equations of 'ellipticity', $\varepsilon = \frac{Q_{major}}{Q_{minor}} - 1$, where Q_{major} and Q_{minor} are the major and minor axes of the ellipse (ball) that is generated from a transformation on a sphero-scale, (Pflug, 1991a). The ellipticity can be found as a function of the scale ratio of the transformation given the linear GSI generator parameters. We, however, are interested in the inverse problem. The ball, and thus its ellipticity, are known, therefore, if the ball can be generated from a sphero-scale, the scale ratio corresponding to this transformation can be found from the inverse of the ellipticity equation. The sphero-scale can then be found by transforming the ball with the calculated scale ratio. If no sphero-scale exists, the transformed ball will not correspond to a sphero-scale.

The choice of whether to use the second or fourth order equations to model the balls is somewhat arbitrary. Often the choice is clear by inspection of the enhanced spectral energy density. However, a more objective method can be implemented if the curve that is fit to the levelset of P is found using the method described directly below. Noting that $1/r^2$ of equation (2.3.5) is the sum of the second order terms of a Fourier expansion, then the ball parameters are simply found by taking the Fourier transform of $1/r^2$, where r is of the positions of the data points as a function of angle. This can be done by discretizing the angles and calculating a Fast Fourier Transform (see Appendix A for details). The higher order terms, of the transform, are assumed to be negligible, or equivalently, they are assumed to be due to the fluctuations about the contour of P. The same method is applicable to the fourth order case (equation 2.3.7), except that $1/r^4$ is

the sum of the second and fourth order terms of the Fourier series. Note that the second and fourth order equations require the transformation of different functions i.e. $1/r^2$ or $1/r^4$. The most simple case (second order) will initially be assumed to be adequate. If the fourth order terms, determined from the transform, are comparable to the second order terms, then it is clear that a fourth order expansion is necessary and consequently the fourth order curve should be found. Conversely, if the fourth order terms are small (i.e. less than a tenth of the magnitude of the second order terms), then the second order curve is used. This was the criteria for determining the appropriate order of equation to model the balls.

3.4 Procedure of the Scale Invariant Generator Technique

The procedure of the Scale Invariant Generator technique can be summarized in point form as follows:

[1] The anisotropic scaling exponent, s, is estimated from the isotropic spectral slope, β, via $s = \beta + D_{el} - 1$. Here, $s = \beta + 1$ (see Pflug 1991a).

[2] The spectral energy density, P, is found by using an FFT technique (Press et al., 1986) to calculate the Fourier transform of the field.

[3] The error function, E^2 of equation (3.3.5), is found numerically at intervals in parameter space. The choice of pairs is made as in equation (3.3.12) (see section 3.3.2b).

[4] The first estimates are found using the ravine search (see sections 3.3.1b, 3.3.2d) over the volume in equation (3.3.20).

[5] The estimate of s is verified by investigating E^2 as a function of s while the generator parameters are held fixed at their first estimate values.

[6] A parabolic expansion of E^2 about the first estimates is made over Range 2 of Table 3.2 (see section 3.3.2c for details). The parameter estimates correspond to

the minimum the parabola. The uncertainties on the estimates are given by equation (3.3.10).

[7] P is enhanced using the generator parameters estimated above (see section 3.3.3).

[8] The parameters of a unit ball are found by fitting a curve of the appropriate form to a levelset of the enhanced P (see section 3.3.3). The appropriate form is determined by the criteria given in section 3.3.3.

Chapter 4

RESULTS ON MULTIFRACTAL SIMULATIONS

4.1 Results on Multifractal Simulations with a Variety of GSI Parameters

In this chapter, the Scale Invariant Generator technique is tested using simulations of continuous multiplicative cascades yielding universal multifractals (Schertzer and Lovejoy, 1987b; Wilson et al., 1991). The basic steps in the simulation are: (a) the production of a 'δ-correlated' (extremal) Lévy noise, the 'sub-generator' (this determines the type of probability distribution), (b) filtering to produce an (anisotropic) $1/f$ noise, the multifractal generator, (c) exponentiation to produce the conserved multifractal, (d) a final (anisotropic) fractional integration (differentiation). For details of the method used to render the algorithm anisotropic, see Pecknold et al. (1993).

A variety of different generator and ball parameters were tested following the procedure described in section 3.4. The multifractal parameters were the same for each simulation: $\alpha = 1.5$, $C_1 = 0.1$, $H = 0.4$. These values are similar to those found empirically in cloud radiances (see Table 1.1). The effects on the accuracy of the technique due to changes in these parameters are studied in section 4.3. The simulations considered were 512×512 pixels in size, (which is a typical size of many geophysical data sets). The simulations were all generated from the same random sub-generator so that the changes in the characteristics of the fields due to the different GSI parameters could be seen more clearly.

The results of each simulation are presented in a separate figure and a separate table. On the top left of the figure is the simulated field in real space, presented using the continuous Palette 3 of Appendix B. All other images are presented using the discontinuous Palette 1. On the top right is the spectral energy density, P, of the simulation. On the bottom left is the enhanced spectral energy density. On the bottom

right the balls, generated from the estimated parameters, are drawn over P; the accuracy of the estimated parameters can be seen quite well in this image and also by comparison with the enhanced P. The simulated and estimated parameters with uncertainties are presented in a table directly following the figure. A discussion of the results and the accuracy of the estimated uncertainties is given in section 4.2.

In order for the estimated ball parameters to be compared to their theoretical values (the parameters of the unit ball of the simulation), the estimated parameters must describe a ball at the scale corresponding to the unit ball. That is, the transformation on a ball, which is induced by T_λ, must be found (as in section 2.4, with the exception that the infinitesimal transformation cannot be used) and used to transform the ball, described by the estimated parameters, to the appropriate scale. Since, for the fourth order case, the algebra involved in this test is non-trivial, another, equally valid test was used. Note that if the estimated ball parameters are accurate, they should describe a contour of constant P. Thus, the accuracy of the fit can be determined by observing if the value of an ensemble average P, with the theoretical generator and ball parameters, is constant along the estimated ball. The mean-squared deviation from the constant value of P can be used as a measure the goodness of the fit. The percentage deviations from the constant were found to be very close to 1% in all cases.

In application to geophysical fields, it is instructive to discover if a sphero-scale exists. The procedure of finding the sphero-scale, discussed in section 3.3.3 (which also involves a transformation of the balls to another scale), was tested on the simulations when the appropriate curve was second order. The results are presented in the table of the corresponding simulation.

A typical example of the ravine search, described in section 3.3.1b and 3.3.2d, is given for Simulation 1. The first estimate values are given in the figure caption. The graphs are not presented in each case since the results are similar.

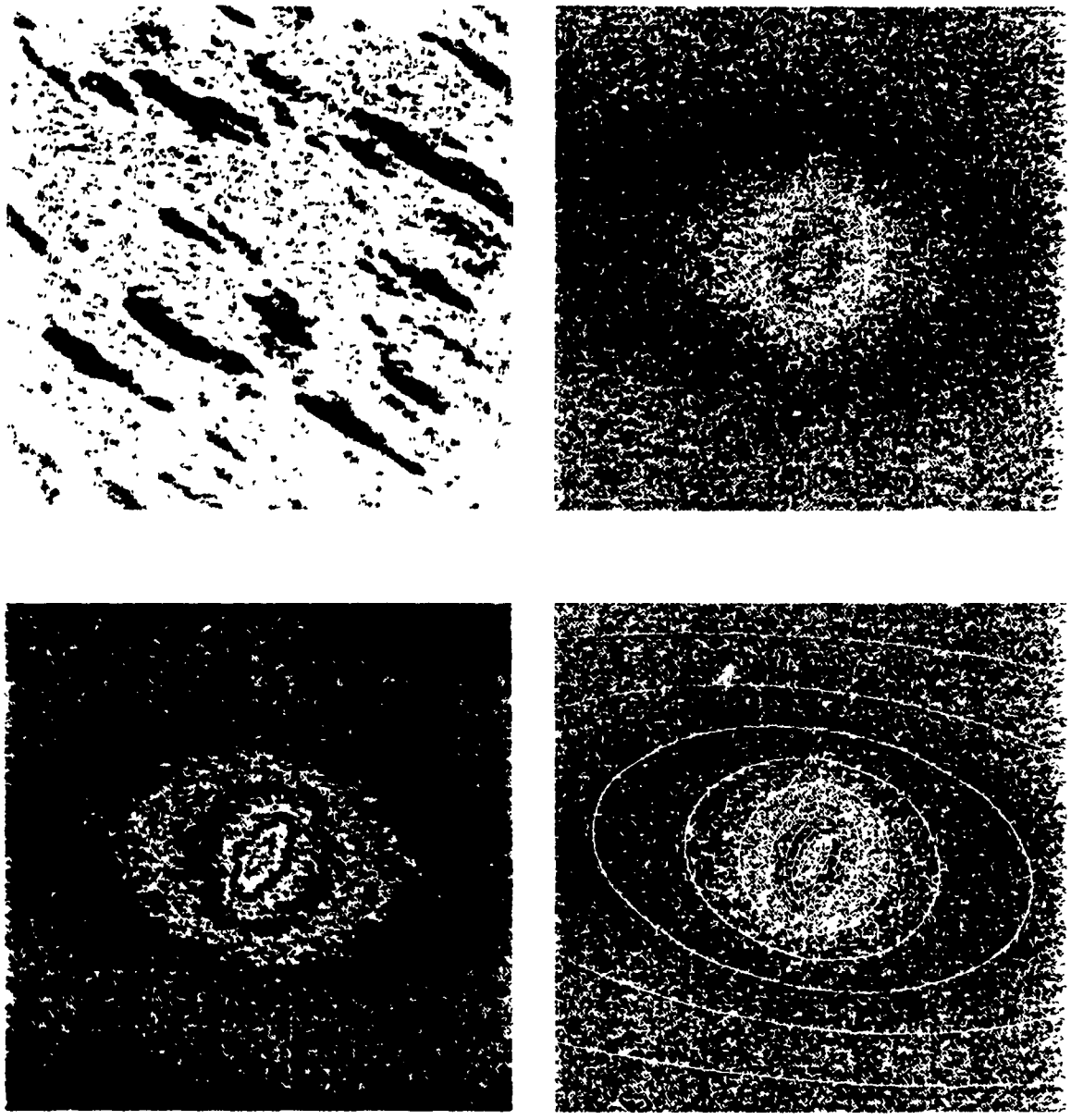

Figure 4.1 Simulation 1 : in real space (top left), spectral energy density (top right), enhanced spectral energy density (bottom left) and spectral energy density with estimated GSI contours (bottom right). See Table 4.1 for simulation and estimated GSI parameters.

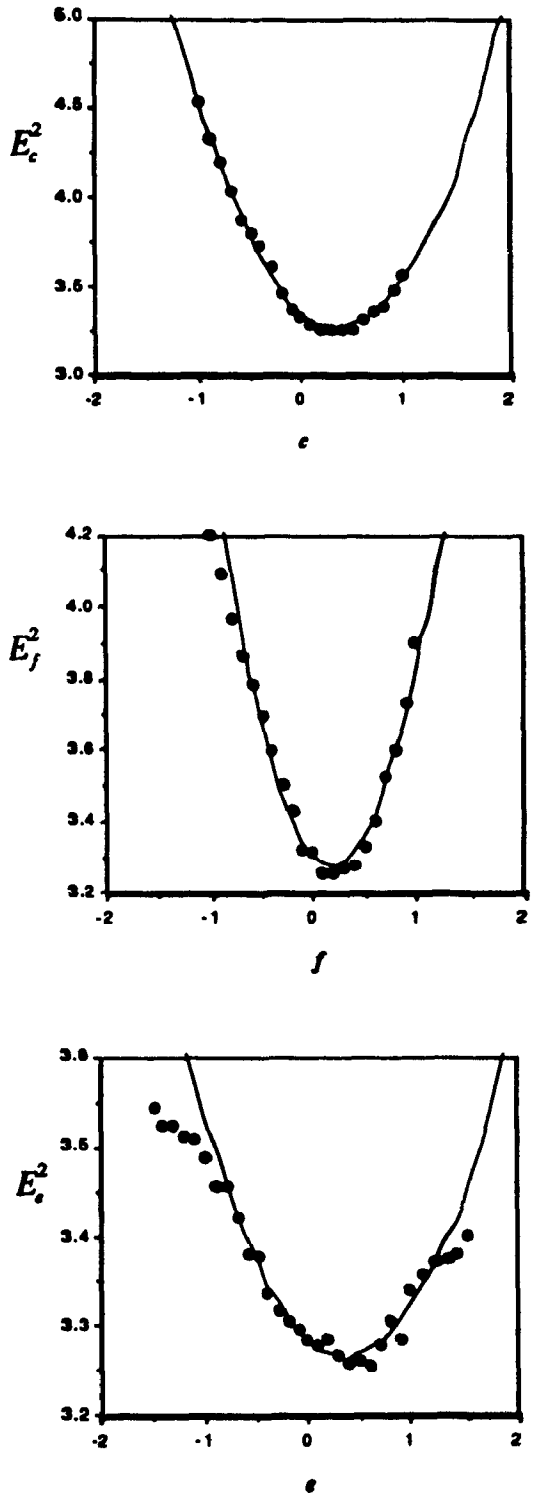

Figure 4.1b : The results of a ravine search for simulation 1 (see figure 4.1). The projections of the ravine onto the c axis (top), the f axis (middle) and the e axis (bottom). The analysis was performed on simulation 1. The parabolas fit near the minimum are shown. The first estimates are: for c: $g_{o_1} = 0.4$, for f: $g_{o_2} = 0.2$ and for e: $g_{o_3} = 0.4$.

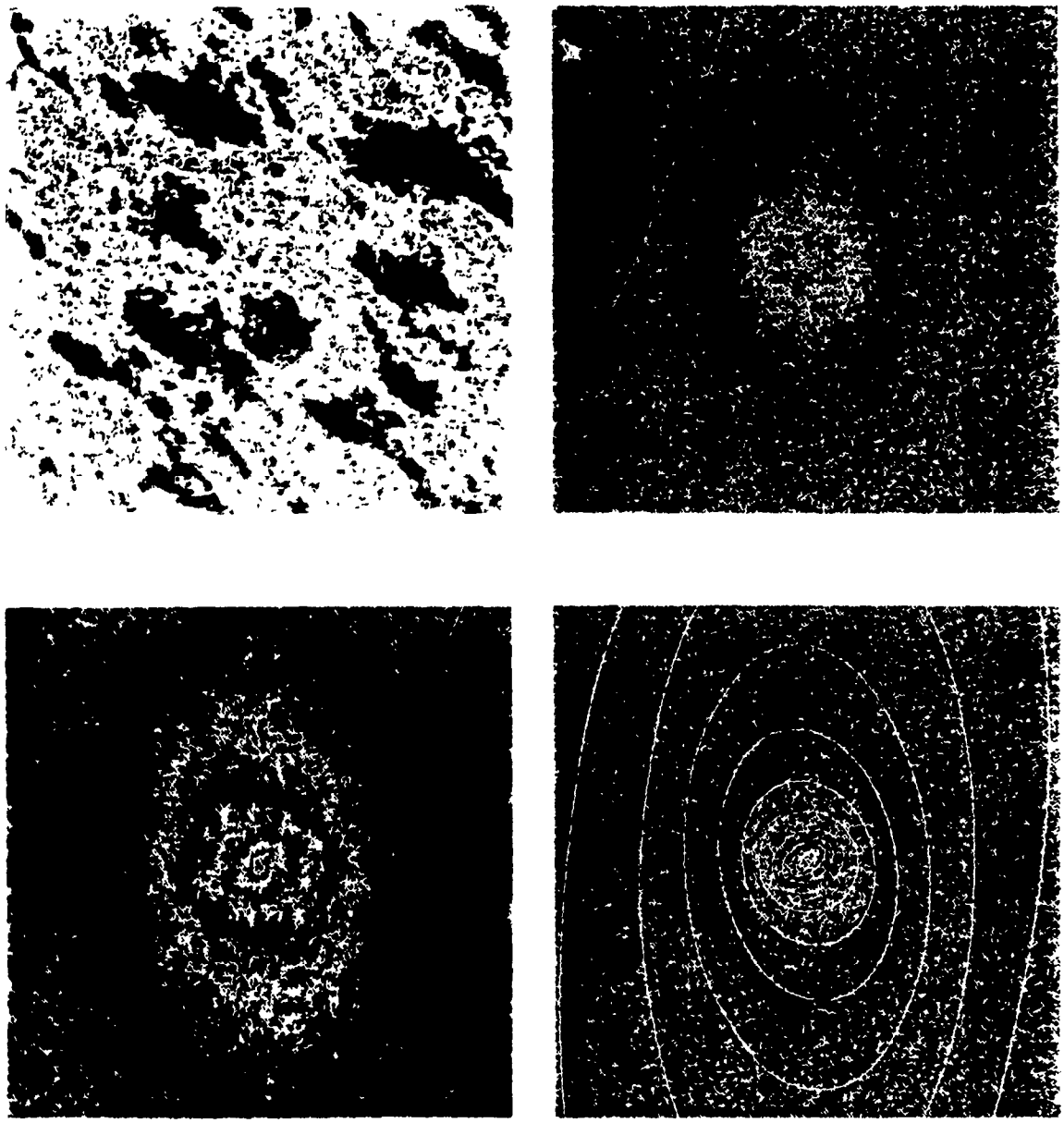

Figure 4.2 Simulation 2 : real space (top left), spectral energy density (top right), enhanced spectral energy density (bottom left) and spectral energy density with estimated GSI contours (bottom right). See Table 4.2 for simulation and estimated GSI parameters.

TABLE 4.1 : Estimated Parameters for SIMULATION 1

parameters	*s*	*c*	*f*	*e*	sphero-scale
theory	2.64	0.3	0.2	0.3	0.146
estimated	2.69 ± 0.04	0.28 ± 0.01	0.20 ± 0.01	0.31 ± 0.03	0.149

TABLE 4.2 : Estimated Parameters for SIMULATION 2

parameters	*s*	*c*	*f*	*e*	sphero-scale
theory	2.64	-0.2	0.2	-0.6	0.098
estimated	2.53 ± 0.04	-0.19 ± 0.01	0.18 ± 0.01	-0.54 ± 0.06	0.100

The sphero-scales are given in units^{-1}, where the external scale is defined to be at 1 unit. Note that the errors were not calculated on the sphero-scale measurements since the errors that were found on the ball parameters (~1%, from mean-squared deviation from a contour of ensemble average P) are magnified non-trivally with a scale transformation. The sphero-scale was found with the method discribed in section 3.3.3.

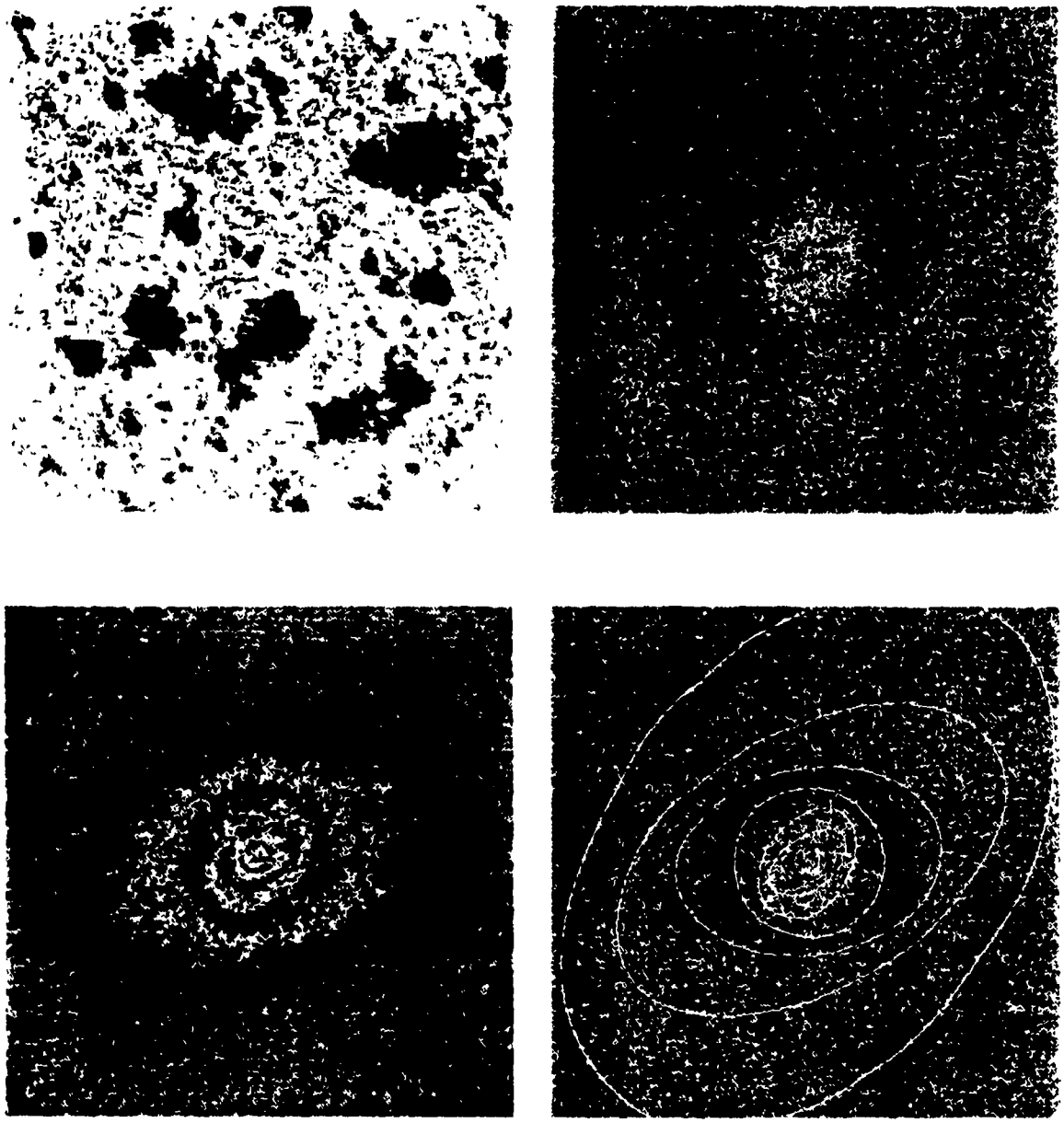

Figure 4.3 Simulation 3 : in real space (top left), spectral energy density (top right), enhanced spectral energy density (bottom left) and spectral energy density with estimated GSI contours (bottom right). See Table 4.3 for simulation and estimated GSI parameters.

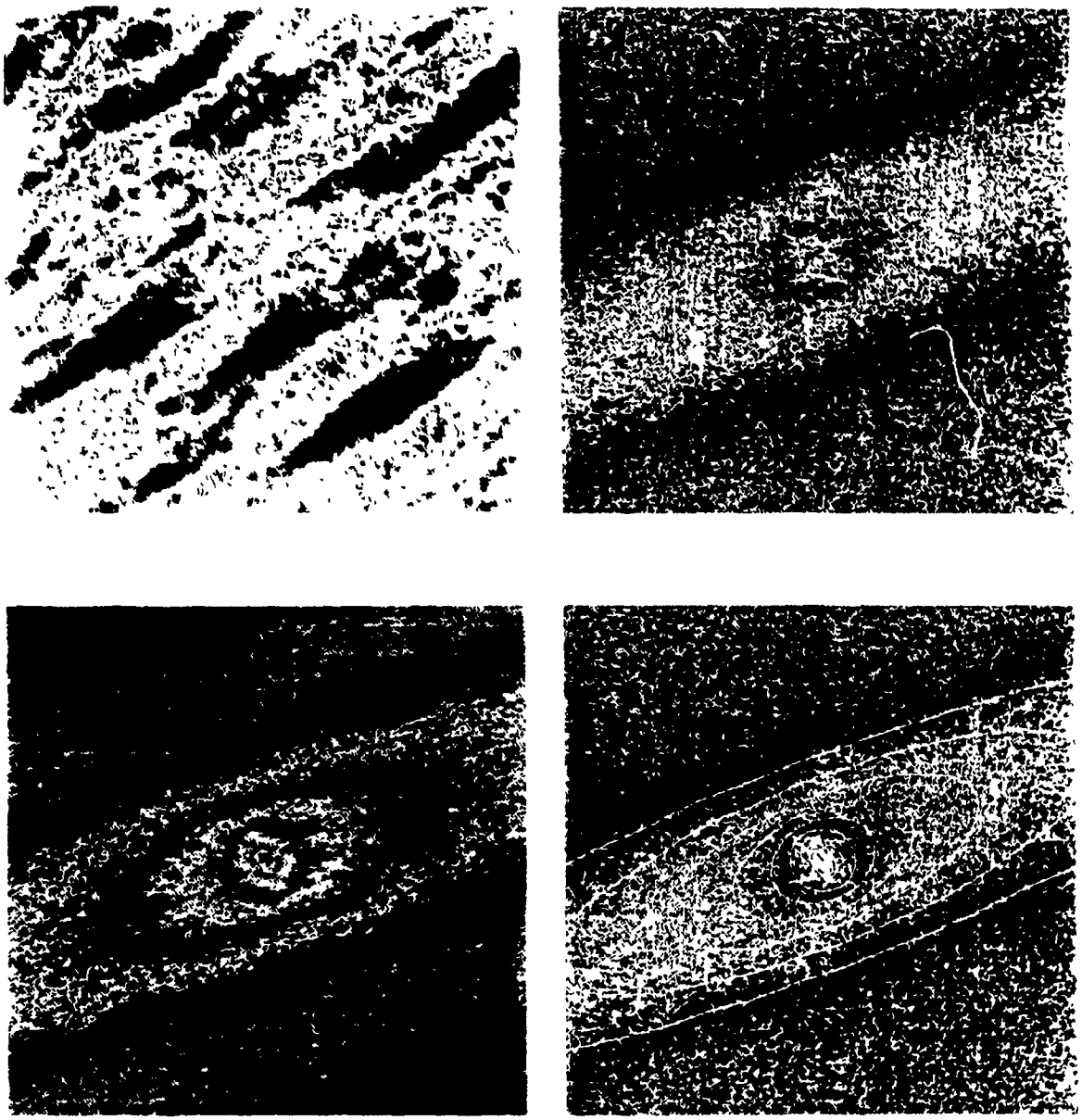

Figure 4.4 Simulation 4 : in real space (top left), spectral energy density (top right), enhanced spectral energy density (bottom left) and spectral energy density with estimated GSI contours (bottom right). See Table 4.4 for simulation and estimated GSI parameters.

TABLE 4.3 : Estimated Parameters for SIMULATION 3

parameters	*s*	*c*	*f*	*e*	sphero-scale
theory	2.64	0.5	0.2	2.0	0.146
estimated	2.64 ± 0.02	0.46 ± 0.02	0.20 ± 0.01	1.92 ± 0.03	0.150

TABLE 4.4 : Estimated Parameters for SIMULATION 4

parameters	*s*	*c*	*f*	*e*	sphero-scale
theory	2.64	0.2	-0.4	-0.2	0.059
estimated	2.60 ± 0.03	0.23 ± 0.01	-0.33 ± 0.02	-0.14 ± 0.03	0.061

The sphero-scales are given in units^{-1}, where the external scale is defined to be at 1 unit. Note that the errors were not calculated on the sphero-scale measurements since the errors that were found on the ball parameters (~1%, from mean-squared deviation from a contour of ensemble average P) are magnified non-trivally with a scale transformation. The sphero-scale was found with the method discribed in section 3.3.3.

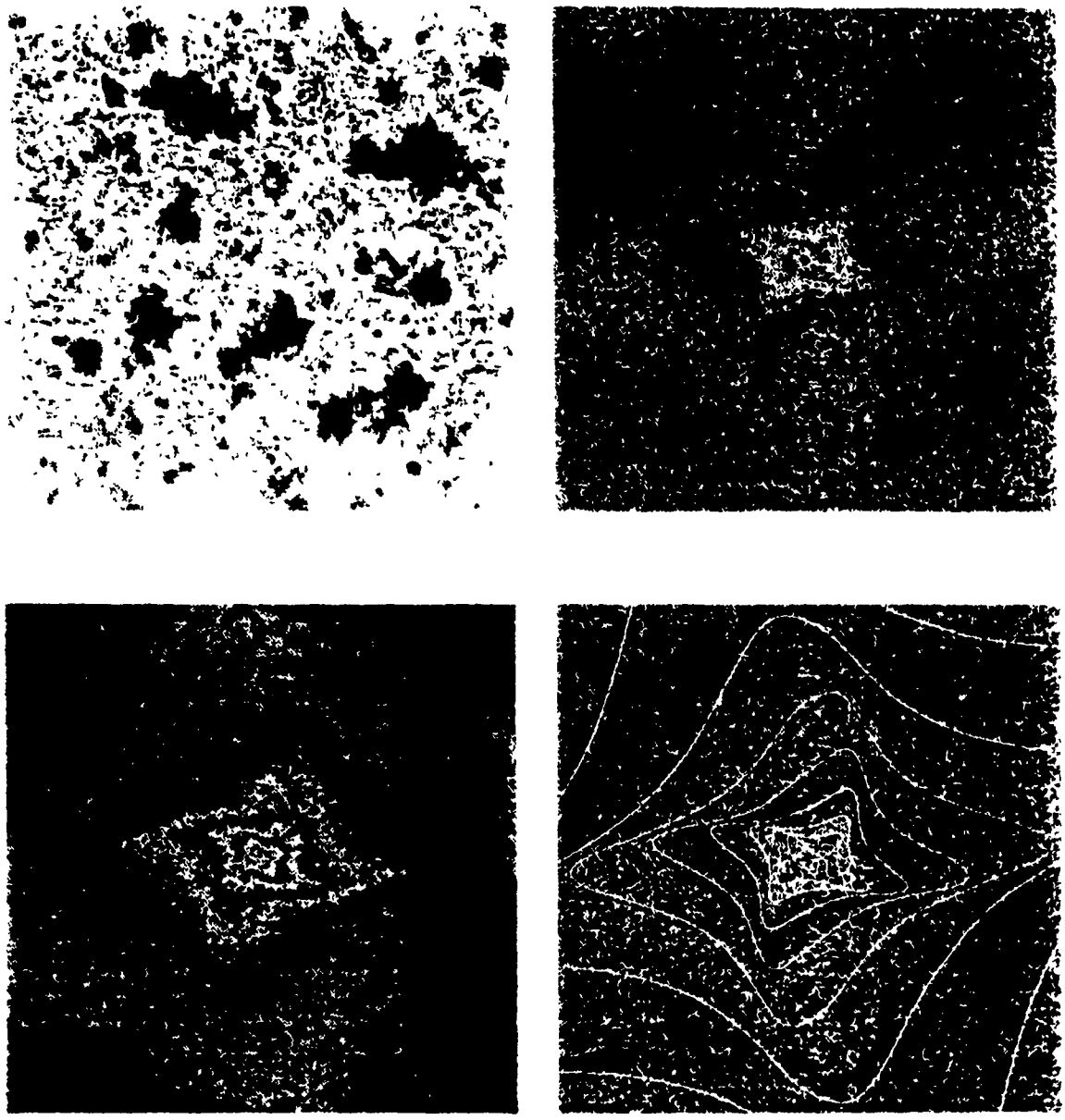

Figure 4.5 Simulation 5 : in real space (top left), spectral energy density (top right), enhanced spectral energy density (bottom left) and spectral energy density with estimated GSI contours (bottom right). See Table 4.5 for simulation and estimated GSI parameters.

TABLE 4.5 : Estimated Parameters for SIMULATION 5

parameter	theory	estimate
s	2.64	2.63 ± 0.03
c	0.1	0.05 ± 0.01
f	0.1	0.08 ± 0.01
e	0.5	0.51 ± 0.01

r_0	a_1	b_1	a_2	b_2
$5.81 \cdot 10^3$	$-3.59 \cdot 10^3$	$2.59 \cdot 10^3$	$0.36 \cdot 10^3$	$4.14 \cdot 10^3$

Note that the balls were approximated by curves of the form in equation (2.3.7) and that the errors in the ball parameters are approximately 1% (measured by the deviation from a a contour of an ensemble average, P). The ball parameters are given in $(\text{units})^4$, where the external scale is defined as 1 unit.

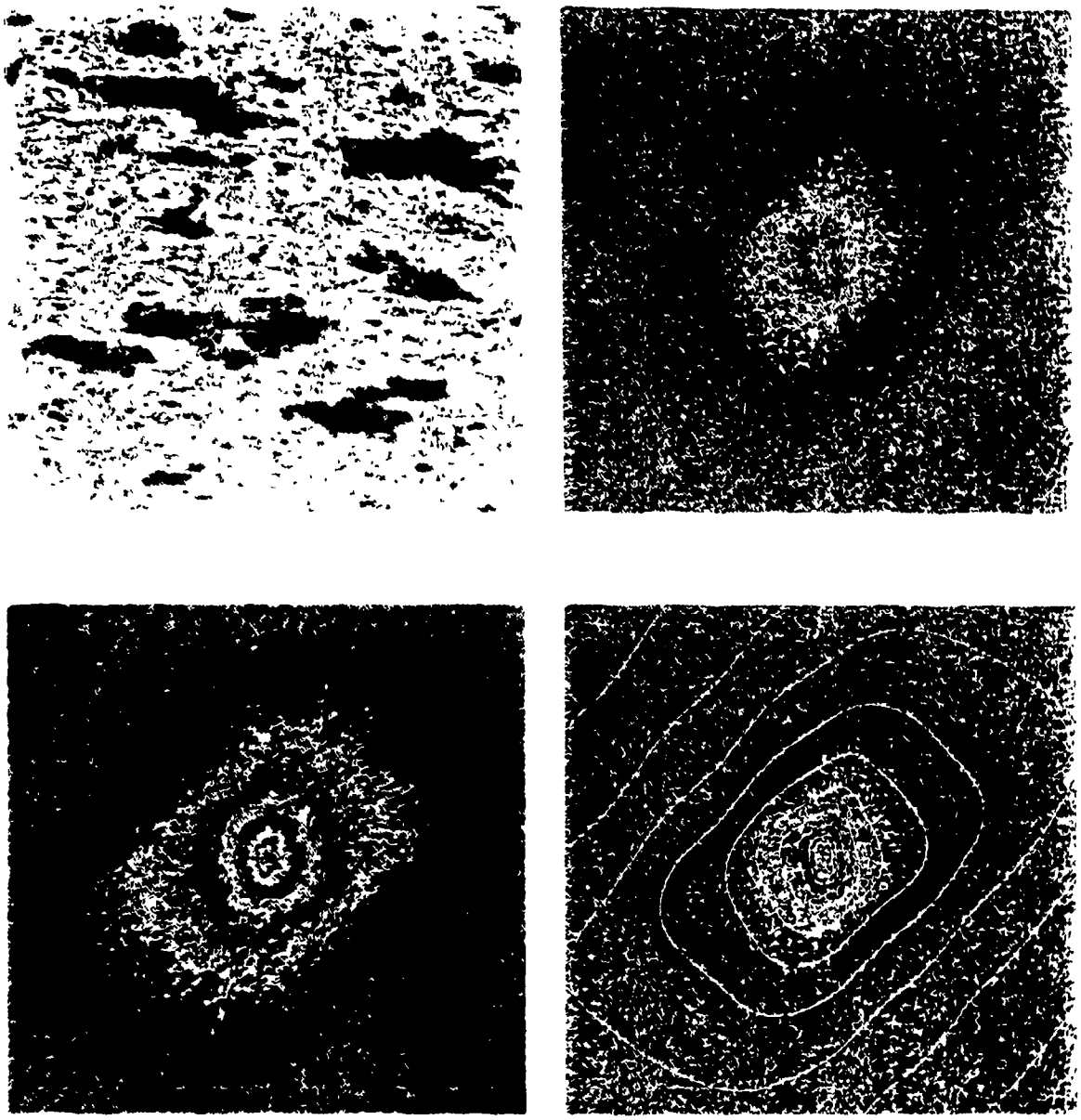

Figure 4.6 Simulation 6 : in real space (top left), spectral energy density (top right), enhanced spectral energy density (bottom left) and spectral energy density with estimated GSI contours (bottom right). See Table 4.6 for simulation and estimated GSI parameters.

TABLE 4.6 : Estimated Parameters for SIMULATION 6

parameter	theory	estimate
s	2.64	2.63 ± 0.02
c	0.23	0.19 ± 0.02
f	-0.19	-0.19 ± 0.01
e	0.36	0.32 ± 0.03

r_0	a_1	b_1	a_2	b_2
$1.01 \cdot 10^3$	$-0.01 \cdot 10^3$	$0.69 \cdot 10^3$	$-0.28 \cdot 10^3$	$-0.10 \cdot 10^3$

Now that the balls were approximated by curves of the form in equation (2.3.7) and that the errors in the ball parameters are approximately 1% (measured by the deviation from a a contour of an ensemble average, P). The ball parameters are given in $(\text{units})^4$, where the external scale is defined as 1 unit.

4.2 Discussion of Results and Investigation of the Accuracy of the Uncertainties

From the results on the simulations of section 4.1, it can be seen subjectively that, the estimated balls, drawn over P, seem to reasonably match the contours of P. However, in many cases, the discrepancies between the estimated and theoretical values are somewhat larger than the estimated standard deviations. A closer investigation is necessary because it is not known if the discrepancies are due to the realization to realization variability (in which case the estimated uncertainties, $\sigma^2_{g_k}$, are too small) or if they are an indication of a biased estimation. Thus, it is necessary to investigate the accuracy of $\sigma^2_{g_k}$.

In chapter 3, it was stated that the uncertainties on the estimates of the GSI parameters, g_k, due to the statistical nature of the data, would be estimated as:

$$\sigma^2_{g_k} = \frac{\varepsilon_{kk} E^2_{\min}}{n} \qquad (4.2.1)$$

where ε_{kk} are the diagonal elements of the error matrix, n is the number of pairs of data points (as in equation 3.3.5) and $E^2_{\min}$ is the value of the hypersurface, E^2, at its minimum.

The $\sigma^2_{g_k}$ are expected to be reasonable estimates of the actual uncertainties if the n pairs are effectively independent, if the hypersurface can be reasonably approximated by a parabola and if the statistics are approximately Gaussian. However, these ideal conditions will not be met and it is unknown exactly how the deviations from the ideal will effect the accuracy of the $\sigma^2_{g_k}$. It is possible to check the accuracy by using the fact that $\sigma^2_{g_k}$ is an estimate of the realization to realization variability in the parameter estimates (due to the statistical fluctuations of the data points). That is, if an ensemble of realizations are analyzed, then the actual uncertainties are the variances of the parameter estimates about their respective mean values. Therefore, in order to obtain a direct estimate of the actual uncertainties, the analysis was performed on ten different simulations that were created with the same GSI and multifractal parameters but with different random sub-generators (i.e. ten different realizations). $\sigma^2_{g_k}$ can then be compared to the uncertainties obtained from the (sample) variances, $s^2_{g_k}$, of the parameter

estimates (of the ten realizations) about their mean values, $\bar{g}_k$ (i.e. a direct measure of the realization to realization variability). Table 4.7 shows the estimates from the ten simulations. The standard deviations quoted are those calculated from equation (4.2.1). The mean values, $\bar{g}_k$, are listed in Table 4.8 (with the actual theoretical values for comparison). The standard deviations calculated from $s^2_{g_k}$ are listed in Table 4.9 along with typical values of σ_{g_k}. The generator parameters of the simulations were: c=0.3, f=0.2, e=0.3, with sphero-scale at 0.30 units^{-1} (where the outer scale is measured as 1 unit) and the simulation was 512×512 pixels in size (see figure 4.1). The procedure, described in section 3.4, was followed.

simulation	c	σ_c	f	σ_f	e	σ_e
1	0.319	0.010	0.168	0.009	0.395	0.025
2	0.306	0.010	0.166	0.009	0.328	0.023
3	0.297	0.010	0.203	0.009	0.300	0.023
4	0.316	0.010	0.214	0.009	0.379	0.024
5	0.324	0.010	0.183	0.009	0.366	0.022
6	0.329	0.010	0.199	0.009	0.305	0.025
7	0.295	0.011	0.167	0.009	0.292	0.026
8	0.342	0.010	0.183	0.009	0.489	0.023
9	0.322	0.011	0.183	0.009	0.288	0.026
10	0.292	0.012	0.192	0.009	0.331	0.027

TABLE 4.7 : Parameter estimates and uncertainties for ten different realizations (with GSI parameters: c=0.3, f=0.2, e=0.3) found using SIG.

g_k	c	f	e
mean values	0.314	0.186	0.347
actual values	0.3	0.2	0.3

TABLE 4.8 : Mean values, $\bar{g}_k$, of the estimates of the parameters of the ten realizations listed in Table 4.7 and the actual simulation values.

g_k	c	f	e
s_{g_k}	0.015	0.016	0.059
σ_{g_k}	0.010	0.009	0.024

TABLE 4.9 : The standard deviations, s_{g_k}, calculated from the variance of the estimates of the parameters (listed in Table 4.7) about $\overline{g}_k$ (listed in Table 4.8) and typical estimated standard deviations, σ_{g_k}, expected from equation (4.2.1) (as in Table 4.7).

Thus, it can be seen that $\sigma^2_{g_k}$ are, in fact, underestimates of the actual uncertainties. However, they are within a factor of two (at worst), which is quite reasonable. The discrepancies between $s^2_{g_k}$ and $\sigma^2_{g_k}$ are most likely caused by the following factors which were not taken into account in the calculation of $\sigma^2_{g_k}$: the statistical dependence of the n pairs, the uncertainties in the estimates of the parabolic coefficients and the non-Gaussian nature of the statistics. Since these factors (and thus the actual uncertainties) are expected to depend on the GSI and multifractal parameters, in general, it is unknown how the discrepancies can be used to increase the accuracy of $\sigma^2_{g_k}$. However, it is expected that the largest change in the factors will come with a change in the multifractal parameters and, as a first estimate, the effects of the factors can be assumed to be approximately independent of the GSI parameters. With this assumption, (better) estimates of the uncertainties of the analysis on the simulations of section 4.1 can possibly be obtained by adding the differences between $\sigma^2_{g_k}$ and $s^2_{g_k}$, of this section, to the uncertainties of section 4.1. We do not claim that adding the differences is a theoretically correct method, but merely state that it could plausibly be an adequate approximation.

Thus, the results of section 4.1 should be reviewed while noting the revised standard deviations, σ'_{g_k}, (where $\sigma'_c = \sigma_c + 0.01$, $\sigma'_f = \sigma_f + 0.01$, and $\sigma'_e = \sigma_e + 0.04$). It can be seen that six of the eighteen estimates were further than one (revised) standard deviation away from the theoretical values. Most of these estimates were just outside this range and only two were further than two standard deviations. This gives an indication that our revised standard deviations are reasonable and that the bias is small. Although the possibility of bias cannot be ruled out, from these findings, we can conclude that an upper bound on the bias is one standard deviation.

Another point of interest is the discrepancies between the mean values of the estimates, $\bar{g}_k$, and the theoretical values of the parameters. These discrepancies could be an indication of bias, since the standard deviation in $\bar{g}_k$ is:

$$s_{g_k}/\sqrt{10}$$

i.e. $\bar{g}_k$ do not lie within one standard deviation of their theoretical values. Note, however, that the bias is still somewhat small (~0.01 of c and f; ~0.03 for e). Although this bias tends to overestimate c and e, and underestimate f, there seems to be no evidence of a systematic overestimation (or underestimation) of the parameters in section 4.1. This implies that the bias may be different for each generator. Some bias could be due to the non-parabolic characteristic of the hypersurface (see section 3.3.2c). This bias could then be reduced by decreasing the range of the parabolic expansion. Because this is expected to increase the realization to realization variability, it is unclear if the change would yield better estimates.

In conclusion, it can be stated that the estimated uncertainties, $\sigma^2_{g_k}$, are in fact an underestimation of the actual uncertainties, however, in general, the results obtained above cannot be used to improve $\sigma^2_{g_k}$. Since $\sigma^2_{g_k}$ are expected to be roughly within a factor of two of the actual uncertainties, they will be maintained as the estimates, with the understanding that they are most probably underestimates. Considering a revision of the $\sigma^2_{g_k}$, the parameter estimates found in section 4.1 seem to be reasonable. Although a bias is expected, evidence shows that it will be reasonably small. The bias is expected to be different for different generator parameters, however, the study in section 4.1 likely shows that the bias is small in a variety of cases. Finally, it can be seen, by inspection of the images of the estimated balls drawn over P, that the generator and ball parameters have been reasonably well approximated. This test is the best measure of the accuracy of the fit since, from the images, it can be judged if the bias in the estimates is too great.

4.3 The Effects of the Multifractal Parameters on the GSI Parameter Estimates and their Corresponding Uncertainties

The results of the analysis (in section 4.1) on simulations, with multifractal parameters comparable to those found empirically in clouds, shows that the Scale Invariant Generator (SIG) technique could plausibly be used in the study of actual cloud radiances. However, since SIG is applicable to many geophysical fields, it would be beneficial to investigate the accuracy with which it measures the GSI parameters of fields with different statistical properties (e.g. different anisotropic scaling exponents and noise characteristics). For universal multifractals, these properties are described by the multifractal parameters: α, C_1 and H (see section 1.2 and Schertzer and Lovejoy, 1987, 1991a). Therefore, by varying the multifractal parameters, the accuracy, with which SIG analyzes fields with different properties, can be examined.

It is expected that the anisotropic scaling exponent, s, will be a major determinant of the accuracy since it determines the rate of decay of the amplitude of the spectral energy density, P, with scale. As s decreases the contours of P become less distinguishable, therefore it is expected that there exists some critical s at which the technique will no longer yield reasonable estimates. Equivalently, it is expected that the curvature of the hypersurface will decrease with decreasing s and thus, the uncertainties in the GSI parameter estimates will increase. The analysis was performed on three theoretical ensemble average spectral energy densities of different s, in order to investigate its effect on the hypersurface. The results are presented in the one-dimensional cross-sections of the hypersurfaces shown in figure 4.7. It can be seen that s has a substantial effect on the curvature.

α, C_1 and H determine the anisotropic scaling exponent, s, in the following manner:

$$s = D_{el} - \frac{C_1}{\alpha - 1}\left(2^{\alpha} - 2\right) + 2H$$

where D_{el} is the elliptical dimension (see section 2.1). Since we will consider $D_{el} = 2$ to be constant, the uncertainties will predominately depend on C_1 and H. H is expected to effect the results solely in its contribution to s, however, C_1 is a direct measure of the

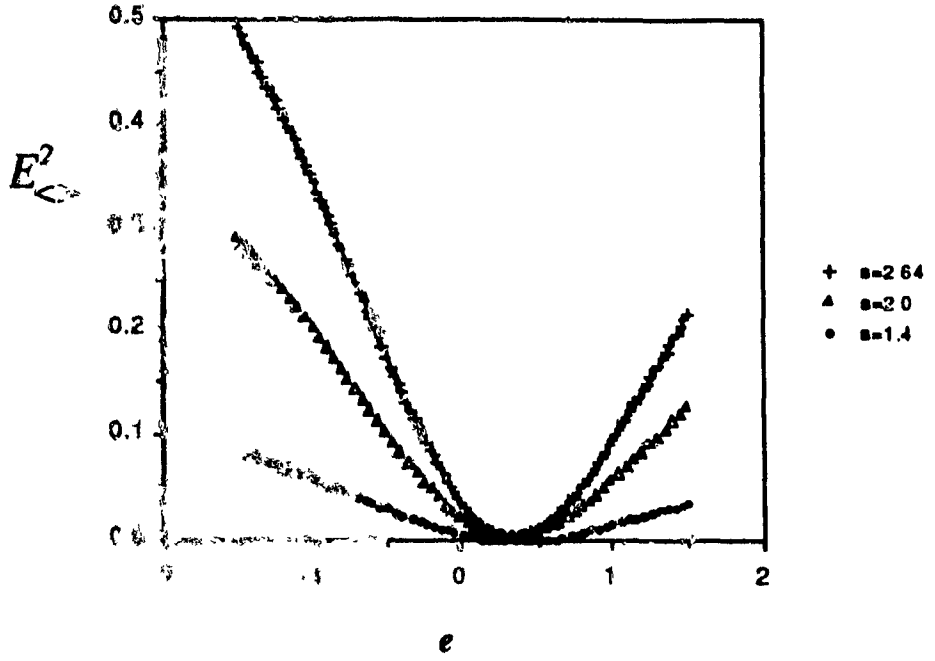

Figure 4.7 : Effect of change in s on the surface of a theoretical ensemble average spectral energy density shown in three one-dimensional cross-sections for s=2.64, s=2.0, s=1.4. It can be seen that s has a substantial effect on the curvature of the hypersurface.

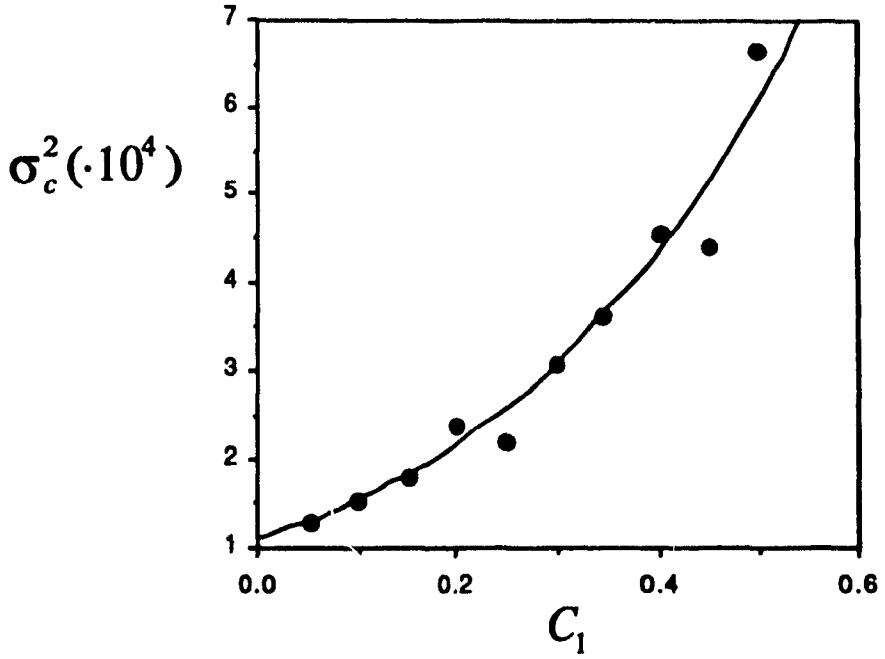

Figure 4.8 : Effect of change in C_1 on uncertainty of the estimate of the GSI parameter c. The data is contained in Table 4.10. An exponential function has been fit to the data.

amplitude of the noise (i.e. the contours will be less distinguishable due to an increase in C_1). The weak dependence of the uncertainties on α will not be studied.

Table 4.10 contains the results of the analysis performed on ten simulations (c=0.3, f=0.2, e=0.3) with different values of C_1. H and α were held constant at 0.4 and 1.5, respectively. The technique as described in section 3.4 was used. As an example, the uncertainty of c is plotted as a function of C_1 in figure 4.8. The results are similar for the uncertainties of f and e. An exponential function has been fit to the data. Note that the uncertainties have been plotted and the standard deviations of Table 4.10 will increase less slowly.

C_1	s	c	σ_c	f	σ_f	e	σ_e
0.05	2.78	0.293	0.011	0.186	0.009	0.383	0.025
0.10	2.69	0.293	0.012	0.190	0.009	0.334	0.028
0.15	2.61	0.302	0.013	0.199	0.009	0.319	0.029
0.20	2.53	0.272	0.015	0.208	0.010	0.279	0.035
0.25	2.45	0.275	0.015	0.216	0.010	0.291	0.033
0.30	2.38	0.256	0.018	0.210	0.010	0.269	0.036
0.35	2.30	0.295	0.019	0.218	0.011	0.312	0.034
0.40	2.23	0.304	0.021	0.232	0.011	0.307	0.037
0.45	2.16	0.340	0.021	0.231	0.012	0.346	0.033
0.50	2.10	0.274	0.026	0.227	0.012	0.262	0.039

TABLE 4.10 : The dependence on C_1 of the parameter estimates and uncertainties of universal multifractal simulations found using SIG. H = *constant* = *0.4*.

The uncertainties were then studied as a function of H (for constant $C_1 = 0.1$). See Table 4.11. It was found that the technique as described in section 3.4 was only able to obtain valid results for $H \geq -0.1$ ($s \geq 1.59$). For values of H smaller than -0.1, the curvature of the hypersurface became negligible compared to the fluctuations about the hypersurface and consequently, the uncertainties became very large. The uncertainties are plotted as a function of s in figure 4.9 (there is a linear relation between s and H).

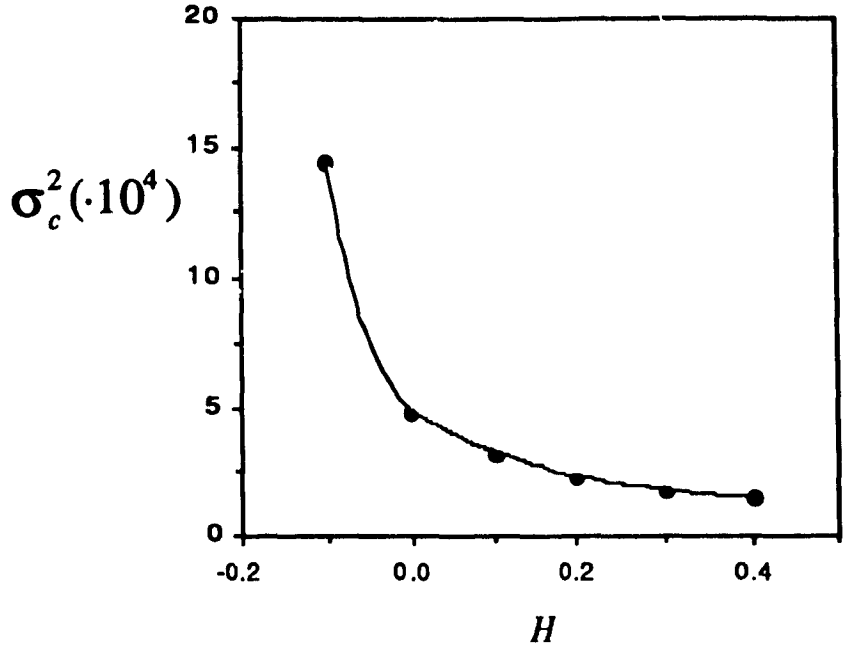

Figure 4.9 : Effect of change in H on uncertainty of the estimate of the GSI parameter c. The data is contained in Table 4.11. A smooth curve has been fit to the data.

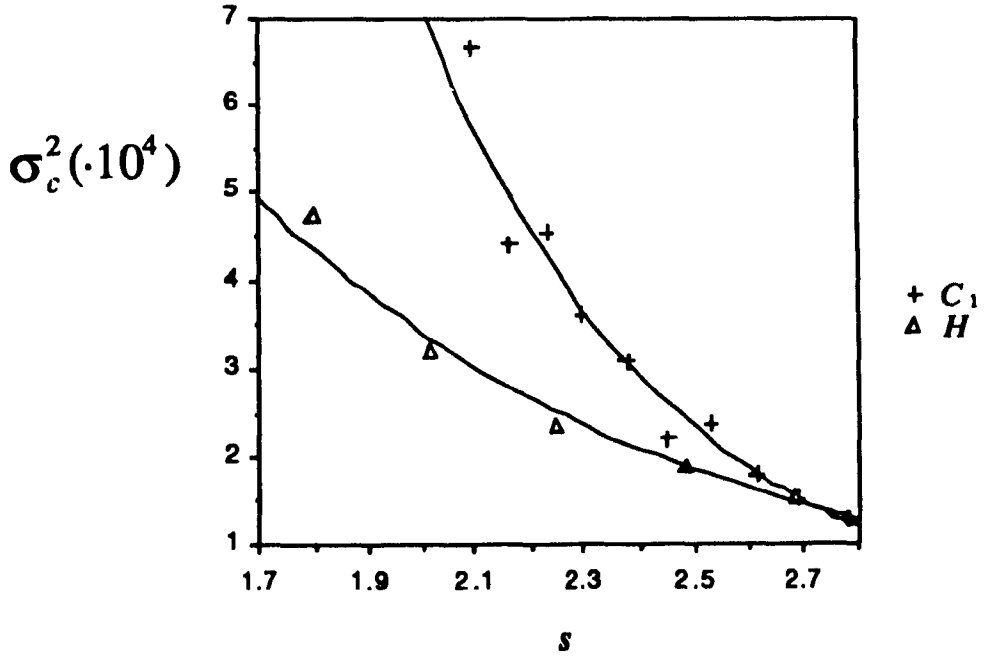

Figure 4.10 : Effect of change in C_1 and H (plotted as a function of s)on uncertainty of the estimate of the GSI parameter c. The data is contained in Tables 4.10 and 4.11. It can be seen that C_1 has a greater effect than H. An exponential function has been fit to the data.

H	s	c	σ_c	f	σ_f	e	σ_e
0.4	2.69	0.293	0.012	0.190	0.009	0.334	0.028
0.3	2.49	0.292	0.014	0.191	0.010	0.332	0.029
0.2	2.25	0.302	0.015	0.186	0.011	0.345	0.033
0.1	2.02	0.282	0.018	0.194	0.013	0.299	0.039
0.0	1.80	0.286	0.022	0.198	0.015	0.283	0.045
-0.1	1.59	0.270	0.038	0.188	0.023	0.278	0.084

TABLE 4.11 : The dependence on H of the parameter estimates and uncertainties of universal multifractal simulations found using SIG. C_1 = constant = 0.1.

In figure 4.10, both the effects of C_1 and H are plotted as functions of s, in order to see their relative effects (exponential functions are fit to the data). It can be seen that the effect of C_1 is greater than that of H. However, in the range studied, valid results were obtained for all C_1. It is expected there will also be a maximum C_1, above which valid results will not be possible. In fact, there will be a combination of effects due to C_1 and H. It may be plausible to assume that (as a first estimate) the effects are additive i.e. that the rate of rapid increase in the uncertainties due to C_1 will be approximately the same, regardless of the value of H, and likewise for H with respect to C_1. This, however, was not studied further.

The above results indicate that SIG, as described in section 3.4, will probably yield valid estimates for a range of multifractal parameters that is adequate to include the majority of the fields of Table 1.1. The parameters of pollutant and seismic fields are possibly outside the range of validity. However, it should be noted that changes can be made to increase this range. For example, by changing the range of the parabolic expansion (see section 3.3.2b), valid results were obtainable for $H \geq -0.3$ ($s \geq 1.16$). The results of the analysis, where the range of expansion was increased for c and e to the first estimates ± 0.6, and for f to ± 0.4, are shown in Table 4.12. Note the discrepancies of the estimated parameters from the theoretical (simulation) parameters are much greater for this case. This is likely due to the increased range of expansion.

H	s	c	σ_c	f	σ_f	e	σ_e
-0.2	1.38	0.274	0.02	0.132	0.02	0.294	0.05
-0.3	1.16	0.266	0.02	0.129	0.02	0.220	0.05

TABLE 4.12 : The dependence on H of the parameter estimates and uncertainties of universal multifractal simulations found using SIG. C_1 = constant = 0.1. Range of expansion is defined in text.

In conclusion, we can state that the technique in its form of section 3.4 is valid for most of the fields described in Table 1.1. If the analysis of fields outside this range of multifractal parameters is required, an adjustment in the range of the parabolic expansion can be made (with the consequence of an increase in bias). This conclusion was made for a given set of GSI parameters and would be expected to change slightly depending on them. However, the conclusions are expected to be reasonable in most cases.

Chapter 5

ANALYSIS ON GEOPHYSICAL FIELDS

5.1 Analysis on Satellite Cloud Radiances

In this section, the Scale Invariant Generator technique (as in section 3.4) is used to analyze satellite cloud radiances. The radiances were obtained from the NOAA-9 satellite, in a channel of the AVHRR sensor that is sensitive to visible wavelengths. In particular, the channel is sensitive to the wavelengths between 0.5 and 0.7 μm. The scenes were obtained with the sensor centered at a point over the Atlantic Ocean, east of Florida (longitude of 70° west and latitude of 27.5° north). These scenes were used in a systematic study of the energy spectrum of cloud radiances (Lovejoy et al., 1993). The resolution of the sensor is 1.1 km and the image is 512×512 pixels in size.

The presentation of the results is identical to that of section 4.1.

The standard deviations quoted were calculated from equation (3.3.10). However, as discussed in section 4.2, they are expected to be underestimates. The error on the balls is expected to be approximately the same as in the case of the simulations. The accuracy of the estimated parameters can be seen quite well by observing the similarity between the estimated and actual contours of P (image on bottom right of figures) and also by comparison with the enhanced P (bottom right of figures).

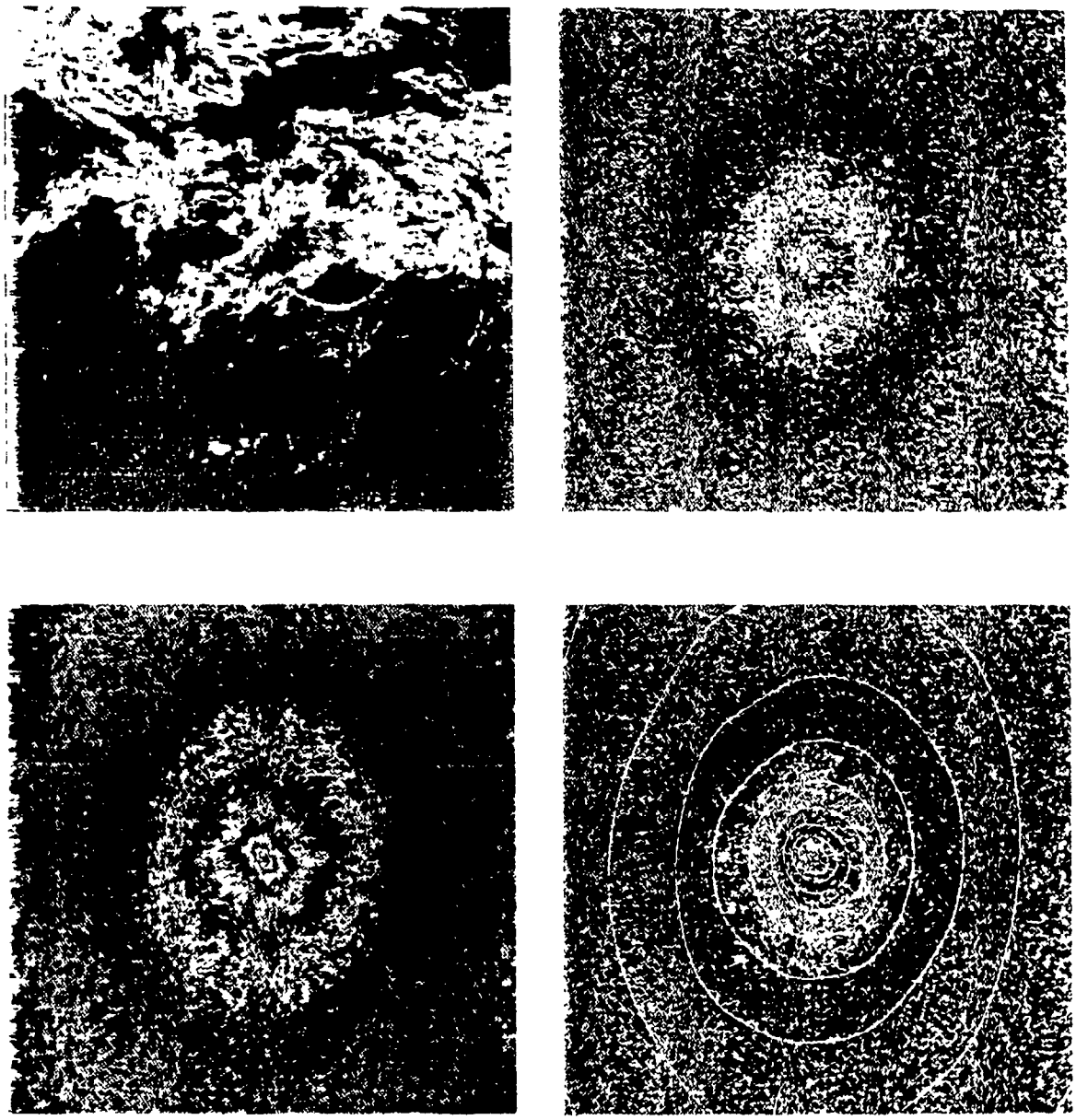

Figure 5.1 Cloud Scene 1 : in real space (top left), spectral energy density (top right), enhanced spectral energy density (bottom left) and spectral energy density with estimated GSI contours (bottom right). See Table 5.1 for estimated GSI parameters.

TABLE 5.1 : Estimated Parameters for Cloud Scene 1

parameter	estimate
s	2.69 ± 0.01
c	-0.05 ± 0.01
f	-0.13 ± 0.02
e	0.47 ± 0.06
a^2	-0.202
r_0	60.3
a_1	8.6
b_1	-1.6
sphero-scale	12.7 km

Note that the balls were approximated by curves of the form in equation (2.3.5). Using the method discussed in section 3.3.3, the field was found not to have a sphero-scale. Ball parameter units are $(\text{km})^2$.

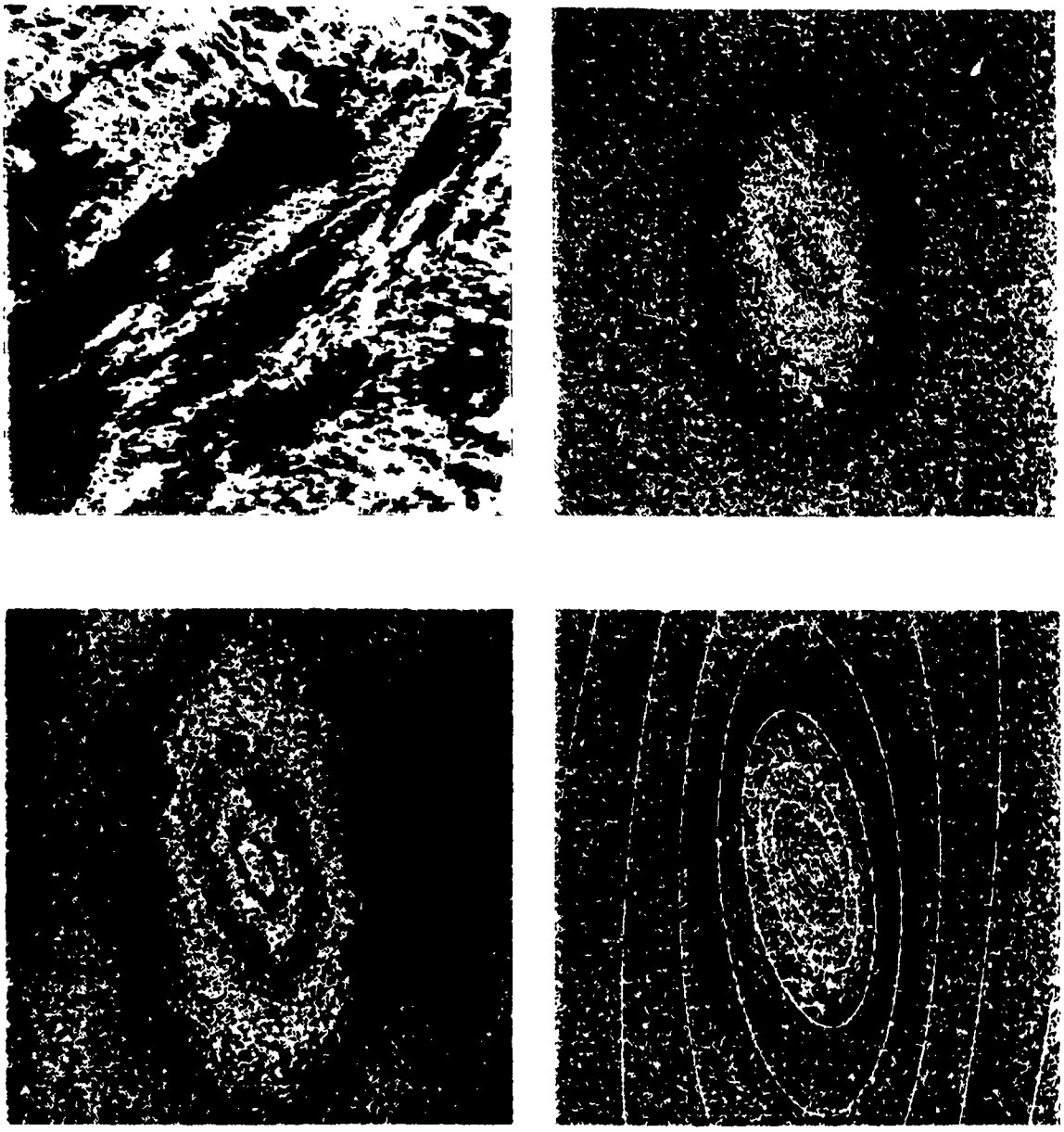

Figure 5.2 Cloud Scene 2 : in real space (top left), spectral energy density (top right), enhanced spectral energy density (bottom left) and spectral energy density with estimated GSI contours (bottom right). See Table 5.2 estimated GSI parameters.

TABLE 5.2 : Estimated Parameters for Cloud Scene 2

parameter	estimate
s	2.45 ± 0.01
c	-0.11 ± 0.01
f	-0.15 ± 0.02
e	-0.01 ± 0.03
a^2	0.035
r_0	101.2
a_1	65.5
b_1	-37.4
sphero-scale	-

Note that the balls were approximated by curves of the form in equation (2.3.5). Using the method discussed in section 3.3.3, the field was found not to have a sphero-scale. Ball parameter units are $(km)^2$.

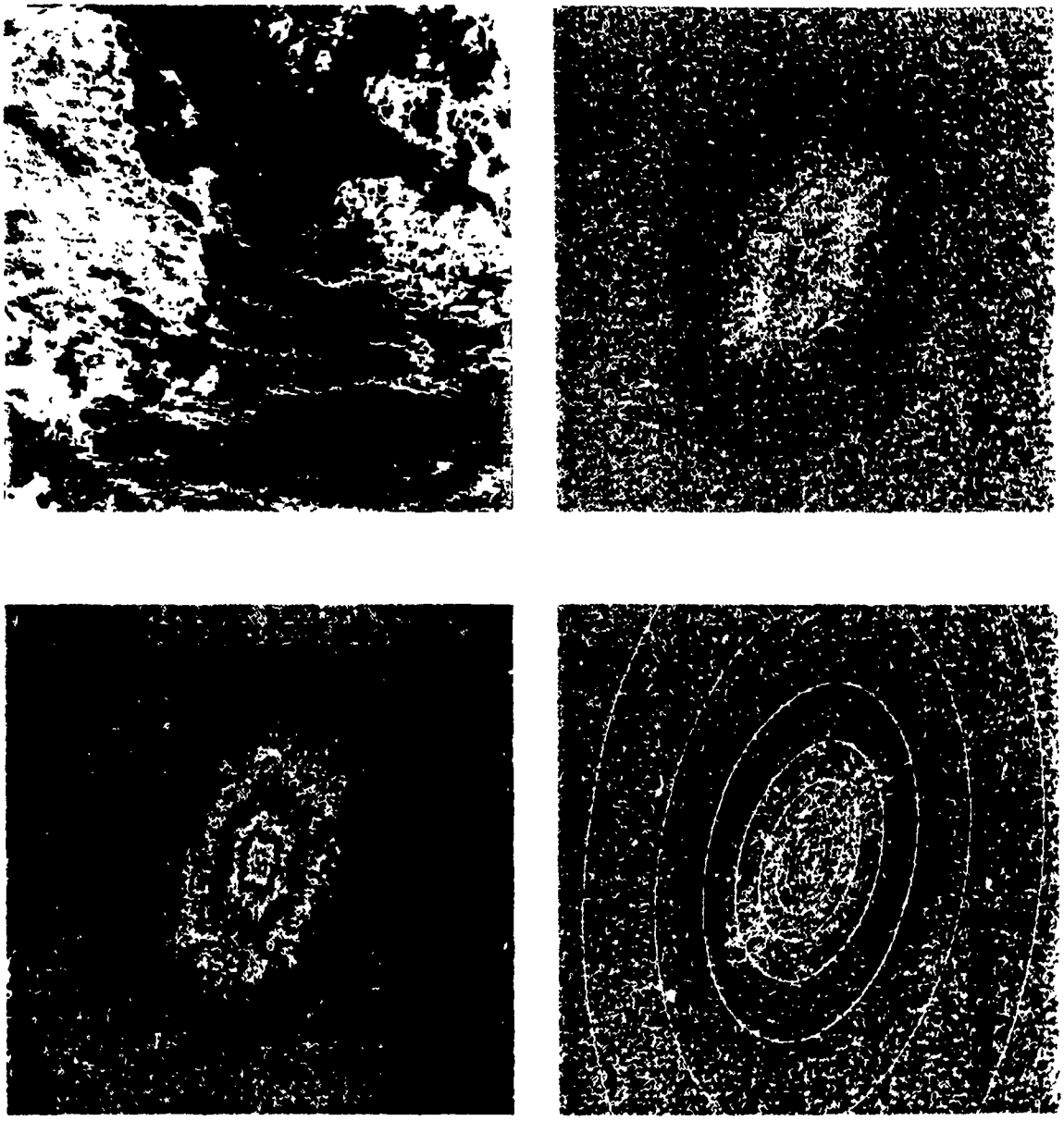

Figure 5.3 Cloud Scene 3 : in real space (top left), spectral energy density (top right), enhanced spectral energy density (bottom left) and spectral energy density with estimated GSI contours (bottom right). See Table 5.3 for estimated GSI parameters.

TABLE 5.3 : Estimated Parameters for Cloud Scene 3

parameter	estimate
s	2.34 ± 0.02
c	-0.05 ± 0.02
f	0.12 ± 0.02
e	-0.12 ± 0.06
a^2	0.003
r_0	96.1
a_1	40.3
b_1	31.1
sphero-scale	-

Note that the balls were approximated by curves of the form in equation (2.3.5). Using the method discussed in section 3.3.3, the field was found not to have a sphero-scale. Bali parameter units are $(\text{km})^2$.

5.2 Analysis on Sea Ice Reflectivities

Below, the results of SIG on sea ice data are presented. The analysis was performed on the SAR reflectivity data. The scenes were taken by the Jet Propulsion Laboratory (JPL) airborne SAR (AIRSAR) operating in the L-band (25 cm) wavelength range. The transmitted and reflected beams were linearly polarized in the horizontal and vertical, respectively. The scenes were obtained over a section of the Beaufort Sea, from an altitude of 9 km, at a latitude of 76° north and a longitude of 165° west.

The presentation of the data is the same as in the previous sections. The results are discussed in section 5.3

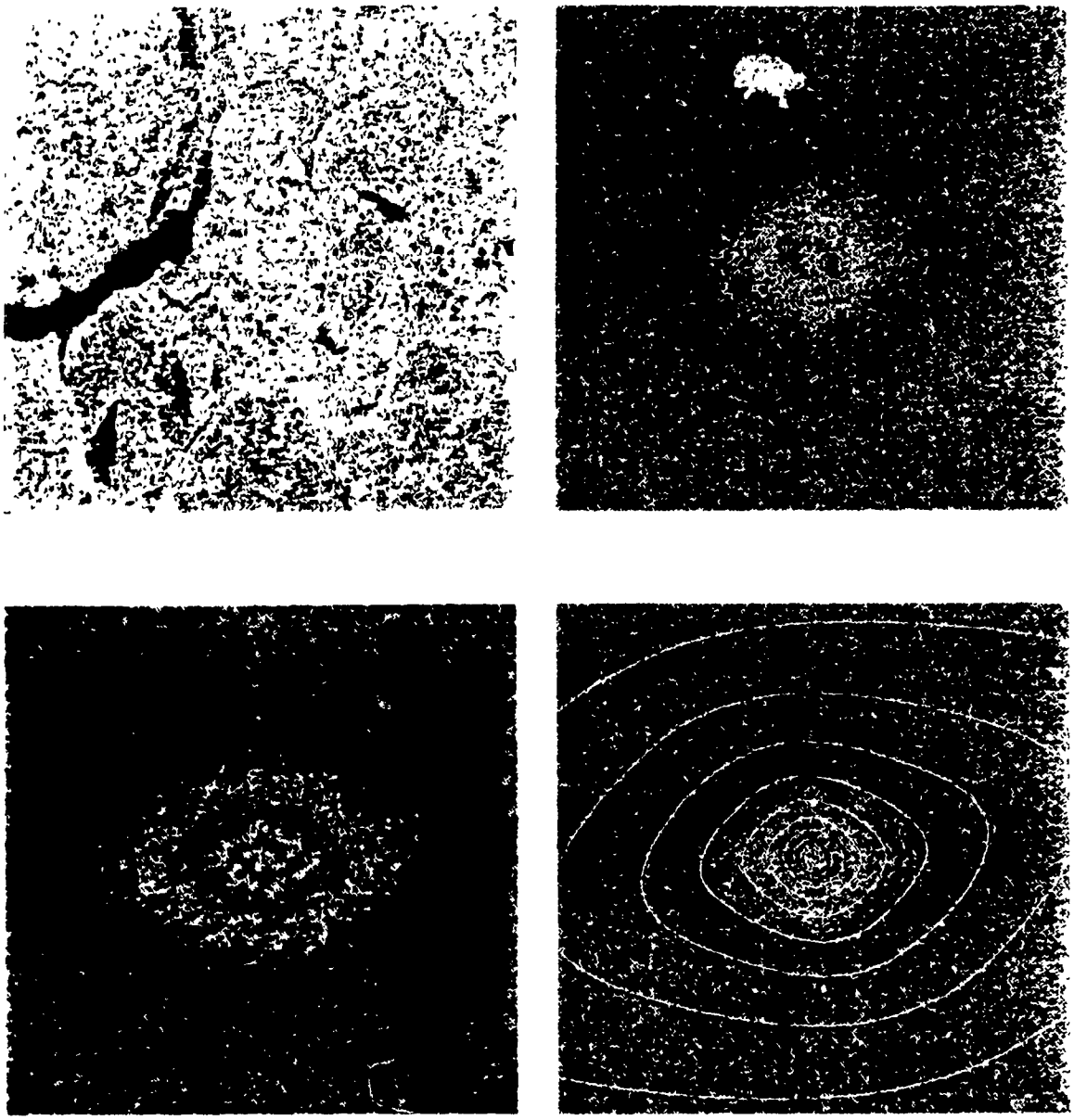

Figure 5.4 Ice Scene 1 : in real space (top left), spectral energy density (top right), enhanced spectral energy density (bottom left) and spectral energy density with estimated GSI contours (bottom right). See Table 5.4 for estimated GSI parameters.

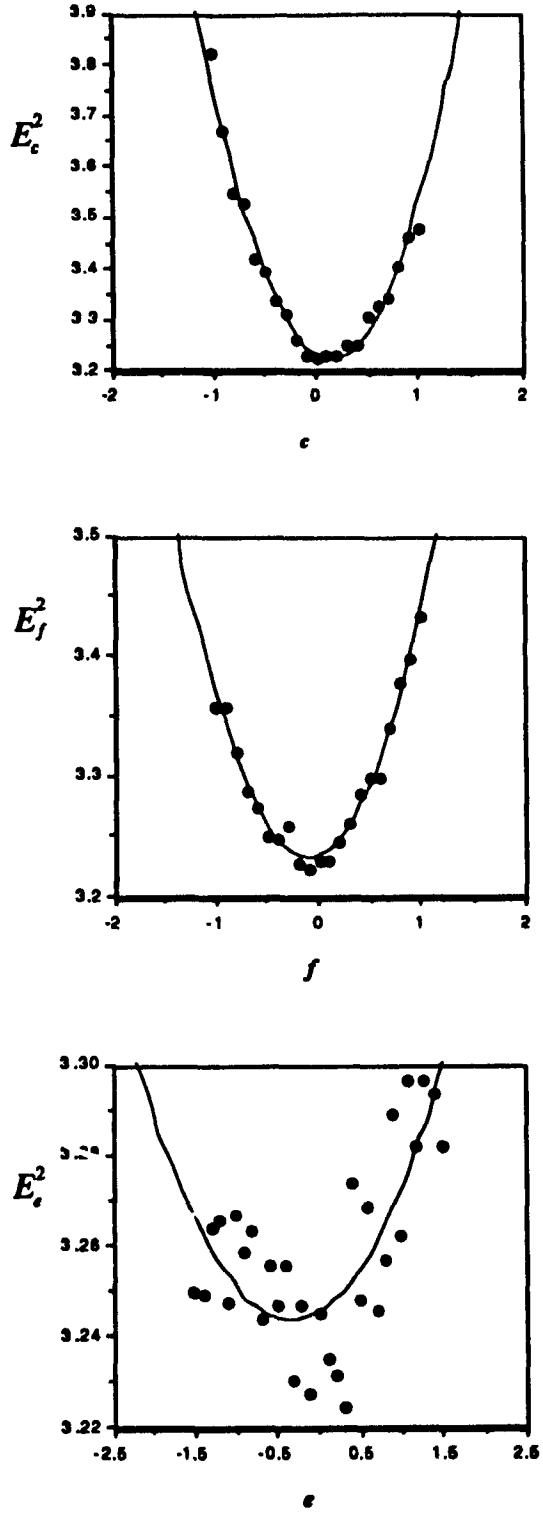

Figure 5.4b : The results of a ravine search for sea ice scene 1 (see figure 5.4). The projections of the ravine onto the c axis (top), the f axis (middle) and the e axis (bottom). The analysis was performed on simulation 1. The parabolas fit near the minimum are shown. The first estimates are: for c: $g_{o_1} = 0.15$, for f: $g_{o_2} = -0.1$ and for e: $g_{o_3} = -0.3$.

TABLE 5.4 : Estimated Parameters for Sea Ice Scene 1

parameter	estimate
s	2.05 ± 0.01
c	0.13 ± 0.01
f	-0.06 ± 0.01
e	-0.10 ± 0.05
a^2	0.011
r_0	$1.01 \cdot 10^{-4}$
a_1	$-0.58 \cdot 10^{-4}$
b_1	$-0.06 \cdot 10^{-4}$
a_2	$-0.17 \cdot 10^{-4}$
b_2	$-0.03 \cdot 10^{-4}$

Note that the balls were approximated by curves of the form in equation (2.3.7). The ball parameter units are $(\text{km})^4$.

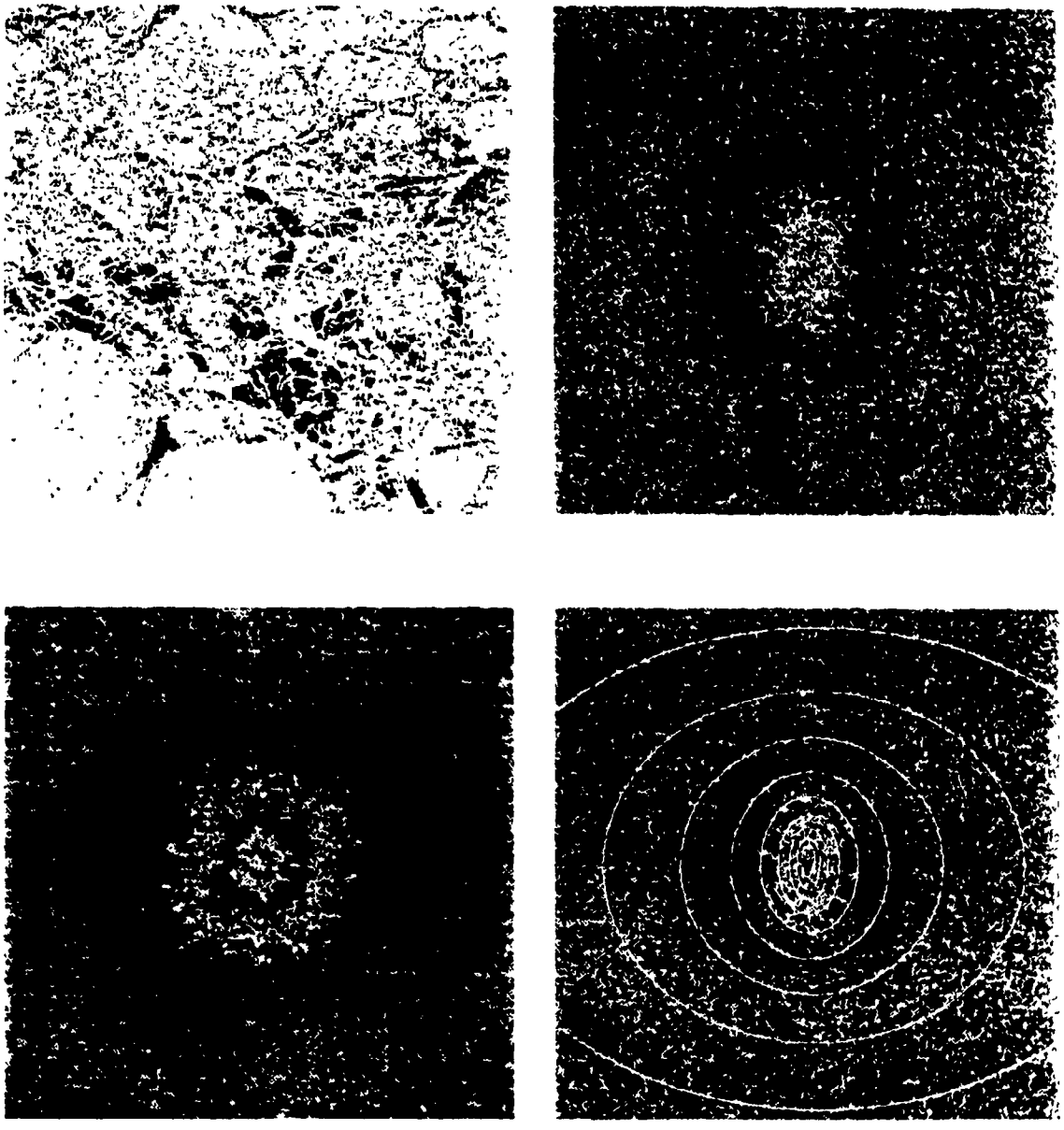

Figure 5.5 Sea Ice Scene 2 : in real space (top left), spectral energy density (top right), enhanced spectral energy density (bottom left) and spectral energy density with estimated GSI contours (bottom right). See Table 5.5 for estimated GSI parameters.

TABLE 5.5 : Estimated Parametrs for Sea Ice Scene 2

parameter	estimate
s	1.84 ± 0.02
c	0.21 ± 0.01
f	0.00 ± 0.01
e	0.00 ± 0.03
a^2	0.044
r_0	$2.95 \cdot 10^{-2}$
a_1	$1.29 \cdot 10^{-2}$
b_1	$0.13 \cdot 10^{-2}$
sphero-scale	53 meters

Note that the balls were approximated by curves of the form in equation (2.3.5). Using the method discussed in section 3.3.3, a plausible sphero-scale was calcuated. Ball parameter units are $(\text{km})^2$.

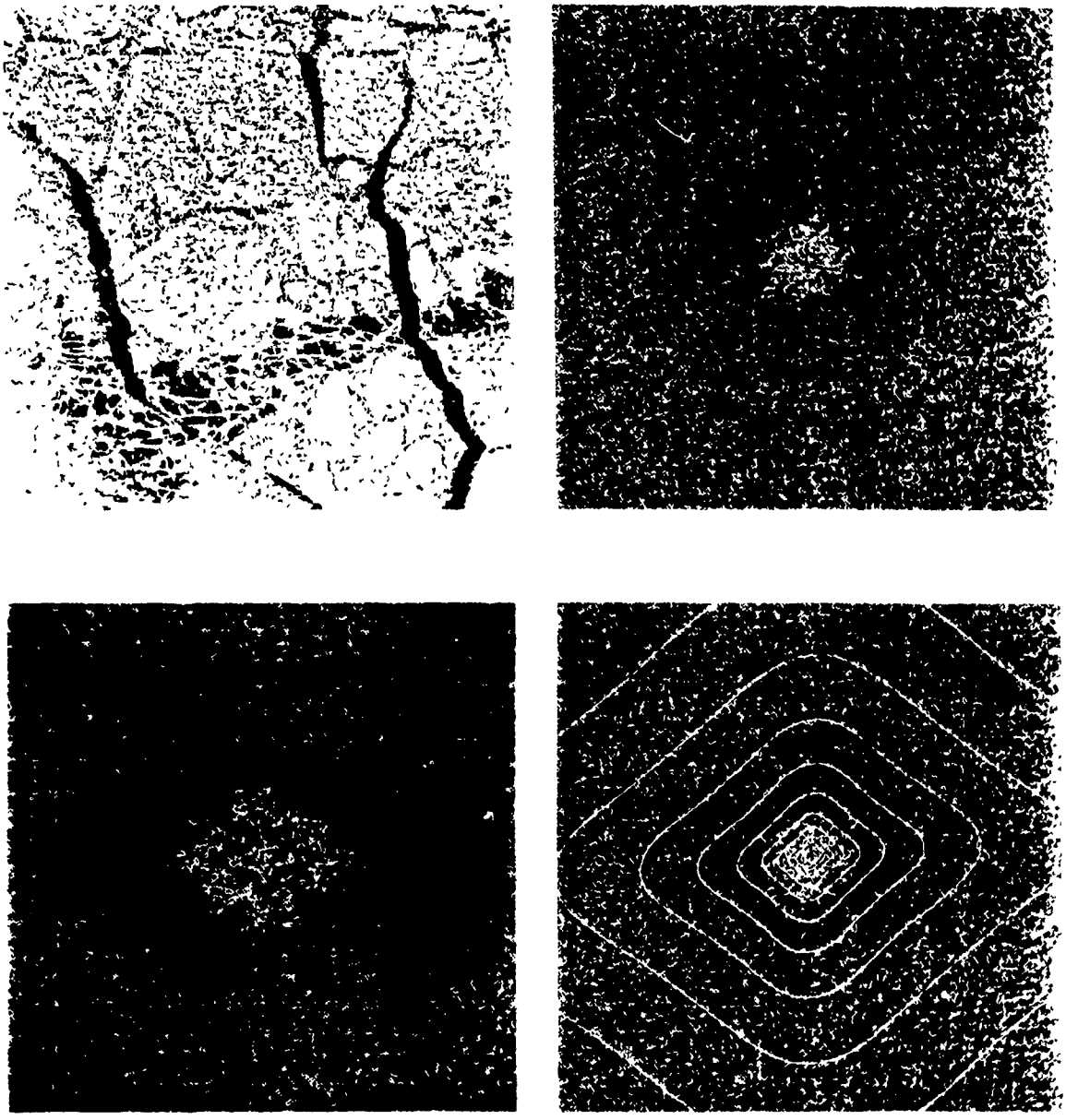

Figure 5.6 Sea Ice Scene 3 : in real space (top left), spectral energy density (top right), enhanced spectral energy density (bottom left) and spectral energy density with estimated GSI contours (bottom right). See Table 5.6 for estimated GSI parameters.

TABLE 5.6 : Estimated Parametrs for Sea Ice Scene 3

parameter	estimate
s	1.50 ± 0.01
c	0.07 ± 0.01
f	0.02 ± 0.01
e	-0.11 ± 0.03
a^2	-0.007
r_0	$2.06 \cdot 10^{-5}$
a_1	$-0.73 \cdot 10^{-5}$
b_1	$0.49 \cdot 10^{-5}$
a_2	$-0.75 \cdot 10^{-5}$
b_2	$-0.11 \cdot 10^{-5}$

Note that the balls were approximated by curves of the form in equation (2.3.7). The ball parameter units are $(km)^2$.

5.3 Discussion of Results

It can be seen that the estimated balls are reasonable approximations in all cases, although it is difficult to judge in the case of Sea Ice Scene 3 since the contours of P are not easily distinguishable.

Attention should be brought to a number of points of interest:

- The balls of all three cloud scenes were adequately described by the second order equation while two of the sea ice scenes used the fourth order. Plausible sphero-scales exist in one out of three of the cloud scenes and one out of three of the sea ice scenes. This further supports the claim of Pflug (1991) that a sphero-scale does not necessarily exist. Also, note that a sphero-scale was not evident in two of the cloud scenes, even though the balls were described by the second order equation. The sphero-scale of the cloud was at 12.7km (similar to values found by Pflug, 1991) and that of the sea ice was at 53 meters.

- Most of the estimated generator parameters are relatively small (of the order of $0.1 \Rightarrow 0.2$). This is well within the range of parameters studied in section 4.1. By inspection it can be seen that although the parameters are small, the anisotropy is not negligible. Note also that two of the six cases studied exhibit rotation dominance ($a^2 < 0$), while four showed stratification dominance ($a^2 > 0$), (see section 2.3). In all cases, however, the magnitude of a^2 is small.

- The estimated uncertainties in the estimated parameters of the sea ice scenes are not greater than those of the cloud scenes, even though the s is smaller. This can be explained because sea ice has been found (empirically) to have a lower C_1 than cloud radiances (see section 4.3 and Table 1.1).

From only six fields strong conclusions cannot be made. However, the results are very encouraging, not only because the technique produced good results, but also because the fields were reasonably modeled using linear GSI. In the future, large scale analysis will be needed to support the assumption of GSI. Also, because different generators produce different field characteristics (see figures in Chapter 4 and 5), it might be possible to use the generator parameters as a quantitative means of classification (in

particular in sea ice and clouds). Many scenes, which have been classified with the present (subjective) methods, could be analyzed to see if the generator parameters of scenes of the same class are similar. Then the scenes may be classified by the volume of parameter space in which they lie.

Chapter 6

CONCLUSIONS

In this thesis, a technique (the Scale Invariant Generator technique, SIG) was developed to estimate the parameters of a linear Generalized Scale Invariant system. It was able to estimate the generator parameters without prior knowledge of the GSI balls. This was an advantage over the previous method. It then used the estimated generator parameters to enhance the spectral energy density and thus it was able to produce good estimates of the GSI balls. The details of the technique were studied so that it could be made numerically efficient. The estimated uncertainties were found to underestimate the actual uncertainties. Universal multifractal simulations, generated with a variety of GSI and multifractal parameters, were used to test the technique. It was found that SIG reasonably estimated the GSI parameters over most of the range of multifractal parameters found in Table 1.1. Specifically, virtually all of the geophysical fields whose multifractal parameters are known have parameters which allow them to be analyzed by SIG. Thus, it can be concluded that SIG could plausibly be used to quantify the anisotropy of many geophysical fields.

The analysis was also performed on three cloud scenes and three sea ice scenes. The estimated contours seemed to be reasonable approximations to the actual contours. This not only supports the above conclusions, but also supports the assumption that cloud and sea ice fields can be approximated by linear Generalized Scale Invariance. For the latter to be conclusive, many more images must be analyzed. It was stated that the GSI parameters may be used as a measure of texture and morphology and as a means of classification. This was not tested in this thesis, however, by inspection of the images and results of chapters 4 and 5, it can be seen that the different GSI parameters correspond to different characteristics of the fields.

Thus, since we are confident that we have developed a valid and useful technique, future research should include the application of SIG to a large number of scenes of a

variety of geophysical fields. If necessary, a modification of the technique may be required to include fields which lay outside the range of multifractal parameters where reasonable results were found. Also, the possibility of using the generator parameters as a quantitative means of classification should investigated. Eventually, it may be possible to test the full non-linear GSI. This is necessary if the full potential of GSI and the Scale Invariant Generator technique is to be discovered.

Appendix A

ELLIPSE FITTING PROCEDURE

A possible method of finding the balls of a scale invariant system consists of fitting a curve to a levelset of the spectral energy density. In section 2.3, the forms of the curves were chosen to be the second and fourth order bi-variate polynomials. It was also shown that these equations could be written as:

$$r = \left[r_0 + a_1 \cos 2\theta + b_1 \sin 2\theta\right]^{-1/2} \qquad \text{(A.1)}$$

and

$$r = \left[r_0 + a_1 \cos 2\theta + b_1 \sin 2\theta + a_2 \cos 4\theta + b_2 \sin 4\theta\right]^{-1/4} \qquad \text{(A.2)}$$

as in equations (2.3.5) and (2.3.7).

There are many possible analytic methods of curve fitting available. See Pflug (1991a; Appendix A for a number). In this thesis, the method described in this appendix was used. It should be noted, that in most analytical methods, the data points are weighted according to convenience. However, in our case, since the points are expected to be scattered predominantly between the theoretical contours $\langle P \rangle \pm \Delta P$, and the amplitude of P falls off as $\ln P$, then the points closer to the origin should be more heavy weighted. This is not possible to do analytically. Therefore, it is expected that analytic methods will be give biased estimates and, generally, will underestimate the parameters (the area of the biased curve will be greater than that of the actual curve). This bias will increase with the amplitude of the noise about the theoretical contour. For this reason, it is necessary to smooth the field before finding the levelset.

Because $1/r^2$ of equation (2.3.5) is the sum of the second order terms of a Fourier expansion, the ball parameters can simply be found by taking the Fourier transform of $1/r^2$, where r is of the positions of the data points as a function of angle. That is, the space is sub-divided into pie-shaped regions delimited by discrete angles. All the points which fall within a region are averaged (according to their radius) to obtain an average radius for that region. This average is found for each region such that the average radius of the data points is known as a function of discrete angles. $1/r^2$ is then computed. A Fast Fourier Transform (Press et al., 1986) can then be used to find the Fourier expansion coefficients of $1/r^2$. The zeroth order term (divided by two) is r_0, the real part of the second order term is a_1 and the imaginary part of the second order term is b_1. This method can also be used for the fourth order equation except using $1/r^4$. r_0, a_1 and b_1 are determined as in the second order case and a_2 and b_2 are the real and imaginary parts of the fourth order term, respectively. Note that since the spectral energy density has the property, $P(\mathbf{k}) = P(-\mathbf{k})$, the odd order terms are expected to be negligible. Also note that the higher order terms are included in the expansion and can be used to determine if the appropriate choice of the order of the equation was used.

Two important details must be considered: the choice of the number of sub-regions (the magnitude of the discrete angles) and the interval of amplitudes to include in the levelset i.e. the choice of ΔP, where the levelset contains all the points of amplitudes $\langle P \rangle \pm \Delta P$. The angles should be chosen such that r is approximately constant over the sub-region, otherwise, biases will be introduced. However, if the angles are too small, then there may be sub-regions which contain no points. Also, the averaging effect is reduced. If the ΔP is too small, then the number of points in the levelset, and thus the statistics, are reduced and if ΔP is too large, biases will be introduced. In the cases studied in this thesis, ΔP was chosen to be 0.04 ($\langle P_1 \rangle$ was chosen to be some intermediate value of the field, approximately 16) and consequently, the number of points in the levelset was of the order of several thousand. The number of sub-regions was chosen to be 64. The bias with these choices appears to be small since the deviation from the contour of the ensemble average was approximately 1%.

Appendix B: Colour Palettes

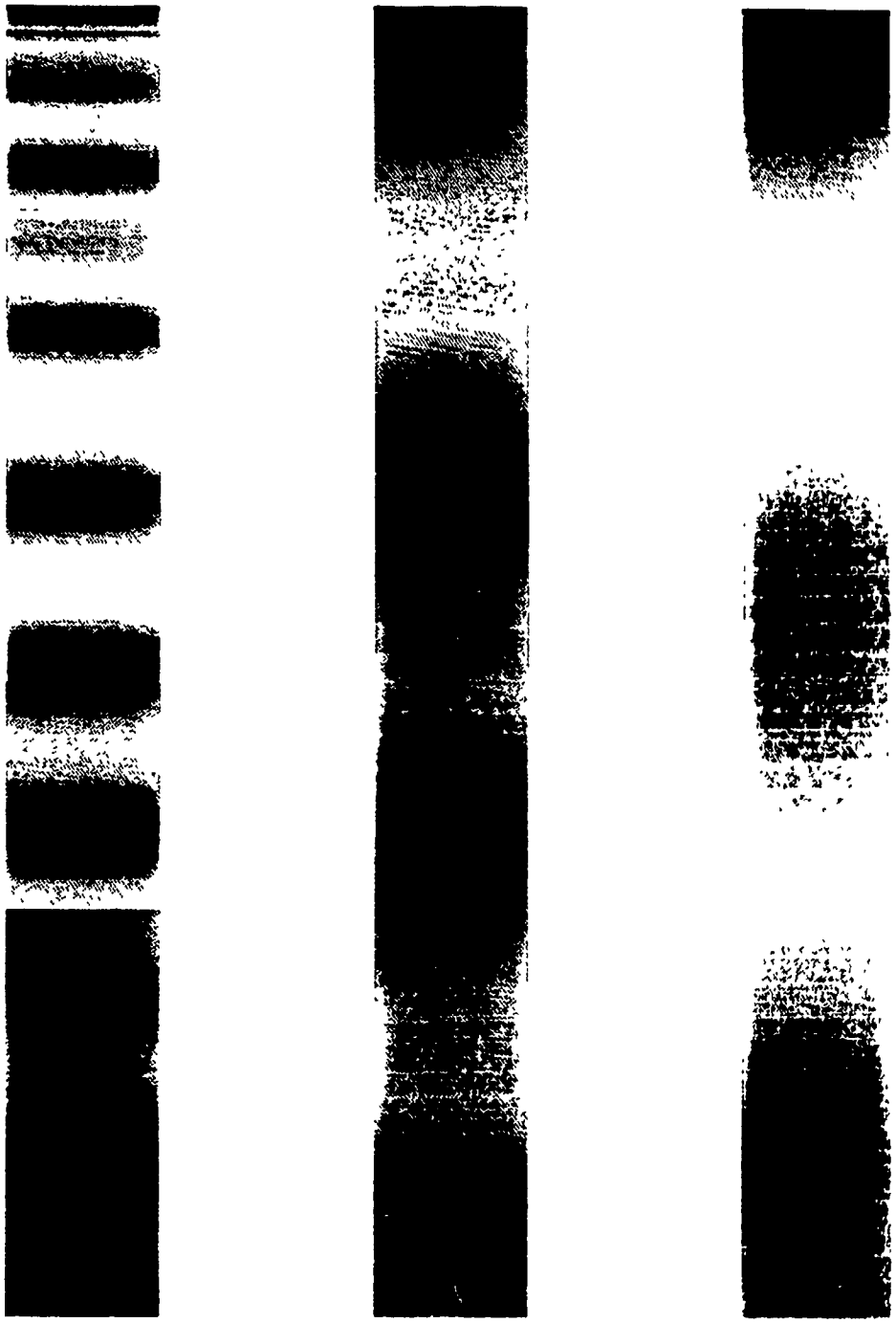

Palette 1 Palette 2 Palette 3

Numerical values corresponding to the colours decrease from top to bottom.

REFERENCES

Adelfang, S. I., 1971, On the relations between wind shears over various altitude intervals. *J. Appl. Meteor.*, 10, 156-159.

Balsley, B. B., D. A. Carter, 1982, The spectrum of atmospheric velocity fluctuations at 8 km and 86 km. *Geophys. Res. Letters*, 9, 465-468.

Bevington, P., 1969, *Data Reduction and Error Analysis for the Physical Sciences*, McGraw-Hill, New York.

Brax, P., R. Pechanski, 1991, Levy stable law description of intermittent behavior and quark-guon phase transitions. *Phys. Lett. B*, 225-230.

Brown, S. R., C. Scholz, 1985, Broad bandwidth study of the topography of natural rock surfaces. *J. Geophys. Res.*, 90, 12575-12582.

Chen, T. C., A. Wiin-Nielsen, 1978, On nonlinear cascades of atmospheric energy and enstrophy in a two-dimensional spectral index. *Tellus*, 30, 313-322.

Duncun, M., 1993, PhD Thesis, McGill University, Montréal, Québec.

Elliot, J.P., P.G. Dawber, 1979, *Symmetry in Physics, Volume 1: Principles and Simple Applications*. MacMillan, Hong Kong. p. 36

Endlich, R. M., R. C. Singleton, 1969, Spectral analysis of detailed vertical wind speed profiles. *J. Atmos. Sci.*, 26, 1030-1041.

Francis, F., T. Falco, S. Lovejoy, D. Schertzer, B. Kerman, M. Drinkwater, C. Livingstone, 1993, Scale invariance and universal multifractals in sea ice synthetic aperature radar reflectivity fields. *Goephys. Res. Letters*, submitted.

Fox, C. G., D. Hayes, 1985, Quantitative methods for analyzing the roughness of the seafloor. *Reviews of Geophysics*, 23, 1-48.

Fritts, D.C., T. Tsuda, T. VanZandt, S. Smith, T. Sato, S. Fukao and S. Kato, 1990, Studies of velocity fluctuations in the lower atmosphere using the MU radar. Part II: momentum fluxes and energy densities. *J. Atmos. Sci.*, 47, 51-66.

Hooge, C., 1993, *Earthquakes as a Space-Time Multifractal Process*. M.Sc. Thesis, McGill University, Montréal, Québec.

Korvin, G., 1993, *Fractal Models in the Earth Sciences*, Elsevier, Amsterdam.

Kolmogorov, A. N., 1962, A refinement on the local structure of turbulence. *Mechanique de la Turbulence* 447, Editions du CNRS, France.

Lavallée, D., D. Jourdan, C. Gautier, C. Hooge, 1993, Universal multifractal properties of microwave satellite data. *Proceeedings of the ASPRS/ACSM 1993 Annual Convention and Exposition*, A. J. Lewis and G. G. Kelly, New Orleans.

Lavallée, D., S. Lovejoy, D. Schertzer, P. Ladoy, 1991, Non-linear variability in landscape topography: analysis and simulations. *Fractals in Geography*, De Cola, L., N. Lam, Ed., Prentice and Hall,171-205.

Lilly, D. K., E. L. Peterson, 1983, Aircraft measurements of atmospheric kinetic energy spectra. *Tellus*, 35A, 379-382.

Lovejoy, S., D. Schertzer, 1985, Generalized scale invariance in the atmosphere and fractal models of rain. *Wat. Resour. Res.*, 21, 1233-1250.

Lovejoy, S., D. Schertzer, A. A. Tsonis, 1987, Functional box-counting and multiple elliptical dimensions in rain. *Science*, 235, 1036-1038.

Lovejoy, S., D. Schertzer, K. Pflug, 1992, Generalized scale invariance and differential rotation in cloud radiances. *Physica A*, 185, 121-128.

Lovejoy, S., D. Schertzer, P. Silas, Y. Tessier, D. Lavallé, 1993a, The unified scaling model of atmospheric dynamics and systematic analysis of scale invariance in cloud radiances. *Ann. Geophys.*, 11, 119-127.

Lovejoy, S., F. Francis, T. Falco, 1993b, Internal report to Canadian Geophysical Survey

Nastrom, G. D., K. S. Gage, 1983, A first look at wavenumber spectra from GASP data. *Tellus*, 35A, 383-388.

Oboukhov, A. M., 1962, Fluctuations of the energy dissipation in turbulence. *J. Geophys. Res.*, 67, 3011-3014

Pecknold, S. Lovejoy, D. Schertzer, C. Hooge, J. F. Malouin, 1993, The simulation of multifractals. In *Cellular Automata: prospects in astronomy and astrophysics*, J. M. Perdang, A. Lejeune, Eds., World Scientific. (in press).

Pflug, K., 1991a, Generalized scale invariance, differential rotation and cloud texture. Master's Thesis, Physics Dept. McGill University, Montréal, Québec.

Pflug, K., S. Lovejoy, D. Schertzer, 1991b, Generalized scale invariance, differential rotation and cloud texture. *Non-linear Dynamics of Structures*, R. Z. Sagdeev, U. Frisch, S. Moiseev, N. Erokhin, Eds., World Scientific, 71-80.

Pflug, K., S. Lovejoy, D. Schertzer, 1993, Differential rotation and cloud texture: analysis using generalized scale invariance. *J. Atmos. Sci.*, 50, 538-553.

Press, W. H., B. P. Flannery, S. A. Teukolsky, W. T. Vetterling, 1986, *Numerical Recipes: the Art of Scientific Computing*. Cambridge University Press, New York.

Rothrock, D. A., A. S. Thorndike, 1980, Geometric properties of the underside of sea ice. *J. Geophys. Res.*, 85, 3955-3963.

Sayles and Thomas, 1978, Surface topography as a nonstationary randon process. *Nature*, 271, 431-434.

Salvadori, G., S. P. Ratti, G. Belli, S. Lovejoy, D. Schertzer, 1993, *J. of Toxicological and Environ. Chem.*, in press.

Schertzer, D., S. Lovejoy, 1983, Elliptical turbulence in the atmosphere. *Proceedings of the 4th Symposium on Turbulent Shear Flows*.. Karlsrhule, West Germany, 11.1-11.8.

Schertzer, D., S. Lovejoy, 1984, On the dimension of atmospheric motions. *Turbulence and Chaotic Phenomena in Fluids*. T. Tatsumi, Ed., Elsevier North-Holland, New York, 505-508.

Schertzer, D., S. Lovejoy, 1985a, The dimension and intermittency of atmospheric dynamics. *Turbulent Shear Flow 4*. B. Launder, Ed., Springer, New York, 7-33.

Schertzer, D., S. Lovejoy, 1985b, Generalized scale invariance in turbulent phenomena. *P. C. H. Journal*, 6, 623-635.

Schertzer, D., S. Lovejoy, 1987a, Singularités anisotropes et divergence de moments en cascades multiplicatifs. *Annales Math. du Que.*, 11, 139-181.

Schertzer, D., S. Lovejoy, 1987b, Physical modeling and analysis of rain and clouds by anisotropic scale multiplicative processes. *J. Geophys. Res.*, 92, 9693-9714.

Schertzer, D., S. Lovejoy, 1988, Multifractal simulation and analysis of clouds by multiplicative processes. *Atmospheric Research*, 21, 337-361.

Schertzer, D., S. Lovejoy, 1989a, Generalized scale invariance and multiplicative processes in the atmosphere. *Pageoph*, 130, 57-81.

Schertzer, D., S. Lovejoy, 1989b, Nonlinear variability in geophysics: multifractal simulations and analysis. *Fractals: Physical Origin and Consequences*. L. Pietronero, Ed., Plenum, New York, 49-79.

Schertzer, D., S. Lovejoy, 1991a, Nonlinear geodynamical variability: multiple singularities, universality and observables. *Scaling, Fractals and Non-linear Variability in Geophysics*. D. Schertzer and S. Lovejoy, Eds., Kluwer, Dordrecht, 41-82.

Schertzer, D., S. Lovejoy, D. Lavallée, F. Schmitt, 1991b, Universal hard multifractal turbulence, theory and observations. *Non-linear Dynamics of Structures*, R. Z. Sagdeev, U. Frisch, S. Moiseev, N. Erokhin, Eds., World Scientific, 213-235.

Schertzer, D., S. Lovejoy (Eds.), 1991c, *Scaling, Fractals and Non-linear Variability in Geophysics*. D. Schertzer and S. Lovejoy, Eds., Kluwer, Dordrecht, 41-82.

Scholz, C., B. Mandelbrot (Eds.), 1989, *Fractals in Geophysics: reprint from PAGEOPH, volume 131 no. 1/2*, Birkhauser-Verlag, Basel.

Schmitt, F., D. Lavallée, S. Lovejoy, D. Schertzer, C. Hooge, 1992, Estimations directes des indices de multifractals universels dans le champ de vent et de température. *C. R. Acad. Sci. Paris*, 314, 749-754.

Schmitt, F., D. Schertzer, S. Lovejoy, D. Lavallée, 1993, Universal multifractal indices oand orders of divergence of moments for atmospheric wind data. *Physics of Fluids*, in press.

Tessier, Y., S. Lovejoy, D. Schertzer, 1993a, Univeral multifracctal: theory and observations for rain and clouds. *J. Appl. Meteor.*, 32, 223-250.

Tessier, Y., S. Lovejoy, D. Schertzer, D. Lavallée, B. Kerman, 1993b, Universal multifractal indices for the ocean surface at far red wavelengths. *Geophys. Res. Letters*, 20, 1167-1170.

VanZandt, T. E., S.A. Smith, T. Tsuda, D.C. Fritts, T. Sato, S. Fukao and S. Kato, 1990, Studies of Velocity Fluctuations in the Lower Atmosphere Using the MU Radar. Part I: Azimuthal Anisotropy. *J. Atmos. Sci., 47, 39-50.*

Vinnichenko, N. K., 1970, The kinetic energy spectrum in the free atmosohere-1 second to 5 years. *Tellus*, 22, 158-166.

Wilson, J., D. Schertzer and S. Lovejoy, 1991, Continuous multiplicative cascade models of rain and clouds. *Scaling, Fractals and Non-linear Variability in Geophysics*. D. Schertzer and S. Lovejoy, Eds., Kluwer, Dordrecht, 185-207.